Investigation of particular crystal defects in solar silicon materials using electron beam techniques

Von der Fakultät für Mathematik, Naturwissenschaften und Informatik
der Brandenburgischen Technischen Universität
Cottbus - Senftenberg

zur Erlangung des akademischen Grades

Doktor der Naturwissenschaften
(Dr. rer. nat)

genehmigte Dissertation

vorgelegt von

Diplom-Physiker

Christoph Krause

geboren am 20. Juli 1984 in Cottbus

Gutachter: Prof. Dr. sc. nat. Martin Kittler
Gutachter: Prof. Dr. Peter Weger
Gutachter: PD. Dr. rer. nat. habil. Hartmut S. Leipner

Tag der mündlichen Prüfung: 04.05.2015

Abstract

The aim of this work is to describe and explain the properties of defects in multicrystalline (mc) and thin-film solar silicon (Si). For this reason, investigations with scanning electron microscope methods were performed, namely cathodoluminescence (CL), electron beam induced current (EBIC), electron backscatter diffraction (EBSD) and transmission electron microscopy (TEM). Additionally, photoluminescence (PL) and reverse-biased electro luminescence (ReBEL) measurements were also conducted. Through correlation of PL, ReBEL and EBIC, it was possible to localize breakdown sites at mc-Si solar cells. Problems that occurred during the thin-film EBIC investigations could be demonstrated and explained. For the first time cross sectional EBIC investigations could be performed on thin-film silicon tandem cells. At mc-Si, it was possible to observe the oxygen related P-line next to the common D1-line luminescence at 10 K clearly distinguishable from each other at once. Furthermore, a hitherto not comprehensively discussed intense luminescence line at 0.93 eV could be described in detail. Through correlation of PL, CL, EBIC, EBSD, and TEM measurements, the origin of the now named Di luminescence at 0.93 eV is postulated to be in connection with Frank partial dislocations, with two energetic levels inside the band gap, one at 112 ± 9 meV below the conduction band and the other at 93 ± 10 meV above the valence band. Finally, it was attempted to explain the behavior of twin boundaries at temperatures below 30 K, where these show an enhanced collection efficiency in comparison to the surrounding grains. An alteration of the local “freeze out” temperature, possibly by a local band gap narrowing, is suggested as a reason. Another conceivable explanation is a breakdown of the diode potential at the grains.

Investigation of particular crystal defects

Das Ziel dieser Arbeit ist es, das Auftreten von verschiedenen Defekten sowohl in multikristallinem als auch in Dünnschicht-Solar Silizium zu beschreiben. Die vielfältigen Möglichkeiten wie Defekte im Material auf Grund ihrer Eigenschaften nachgewiesen werden können, wurden eingehend untersucht. Dazu wurden Rasterelektronenmikroskopie Verfahren wie Kathodolumineszenz (CL), Elektronenstrahl-induzierte Strom (EBIC) Messungen, rückgestreute Elektronenbeugungsuntersuchungen (EBSD) und Transmissionselektronenmikroskopie (TEM) durchgeführt. Außerdem wurden auch Ergebnisse aus Photolumineszenz (PL) und Elektrolumineszenz unter Sperrvorspannung (ReBEL) zur Defektcharakterisierung herangezogen. Durch die Korrelation von ReBEL, PL und EBIC Daten war es möglich, Durchbruchstellen in mc-Si Solarzellen zu lokalisieren und mögliche Ursachen für diese aufzuzeigen. Die Anwendung von EBIC an dünnen Siliziumschichten sowie die damit verbundenen Präparations-, Mess- und Analyseprobleme konnten gezeigt und erläutert werden. Es war außerdem erstmals möglich EBIC Messungen an Querschnitten von Dünnschicht-Silizium-Tandemzellen erfolgreich durchzuführen und dadurch Informationen über die Rekombinationsaktivität von Defekten in unterschiedlichen Schichten der Zellen zu sammeln. Bei der Durchführung von CL Messungen an mc-Si bei 10 K konnte gezeigt werden, dass die in der Literatur mit Sauerstoffpräzipitaten in Verbindung gebrachte Lumineszenz bei 0.77 eV (P-Linie), auch parallel zur D1-Linie klar unterscheidbar auftreten kann, was bis dahin in dieser Art noch nicht publiziert wurde. Neben der P-Linie konnte eine intensive Lumineszenz bei 0.93 eV festgestellt werden, die ebenfalls bei Raumtemperatur messbar ist. Diese bis dahin nicht umfassend beschriebene Lumineszenz, welche im Laufe der Arbeit die Bezeichnung Di-Linie erhielt, wurde detailliert untersucht und beschrieben. Dazu wurden die Ergebnisse von PL, CL, EBIC, EBSD und TEM miteinander korreliert. Durch die umfassenden Untersuchungen konnte ein Zusammenhang mit Frank Partialversetzungen postuliert werden. Für diese Defektlumineszenz könnten zwei Defektlevel in der Bandlücke, bei 112 ± 9 meV unterhalb des Leitungsbandes und 93 ± 10 meV oberhalb des Valenzbandes, verantwortlich sein. Im letzten Teil der Arbeit wurde versucht, das Sammlungsverhalten von Zwillingskorngrenzen bei Temperaturen unterhalb von 30 K zu erklären. In diesem Temperaturbereich zeigen Zwillingskorngrenzen eine erhöhte Sammlungseffizienz im Vergleich zu den umgebenen Körnern. Als Ursache dafür wird ein lokaler Unterschied in der "Ausfriertemperatur" der Ladungsträger vermutet. Um eine derartige Schwankung auszulösen, könnte eine lokale Verkleinerung der Bandlücke, möglicherweise spannungsinduziert, in Frage kommen. Eine ebenfalls in Betracht kommende Erklärung wäre ein Zusammenbruch des Diodenpotentials im Bereich der Körner.

Contents

1 Introduction

Since the first produced silicon-based solar cells with just 4-6% efficiency by Bell laboratories in 1953, the investigations to generate electricity by sunlight have achieved huge steps forward. Only a few years after the first production, satellites were equipped with Si solar cells in 1958 to charge their batteries in space. At earth, solar cells could provide the opportunity to supply areas far away of the electric grid with electricity. In my opinion, this is one of the most useful applications for solar cells. In recent years, this kind of application was moved out of the research focus. Nowadays, after several oil crises, some disastrous accidents in nuclear power plants, and not to forget global warming, the main aim of research in photovoltaics (PV) is the coast reduction of solar cell production and of course the increase in efficiency to create an alternative source of power generation. If it were possible to provide a cheap and efficient source of power generation, nuclear power plants and coal power stations could be shutdown, while the need for oil would also be reduced, using solar powered means of transportation instead of gas dependent ones. I guess there is a chance that it is sufficient to charge batteries with the help of solar power, like in the first days of fabrication. Nevertheless, there remains a huge research requirement to achieve the goal of shutting down the conventional kinds of power plants. According to the current facts of PV [release 28.05.2014; latest available at www.pv-fakten.de], supplied by the Frauenhofer ISE, in 2013 PV power was able to provide 5.7% of the net power consumption of Germany, while all alternative sources of energy together achieved up to 29%. It is exciting that at sunny workdays today it is possible to achieve 35% with just PV-modules and even 50% at sun- and holidays. However, the current generated with PV remains more expensive than that produced by conventional power plants. Therefore, it is still necessary to continue research in the field of PV to enhance the knowledge of the used solar materials and establish the opportunity to improve the solar cell performance. For this reason it is important to know where the limiting influences in the solar materials originates from, how they arose, how they take effect, how they can be controlled and of course how they can be avoided. The Joint Lab IHP/BTU founded in 1999 works in the field of fundamental principles oriented research with the aim of achieving improved Si properties by defect engineering. Through fundamental research, the basic

knowledge about defect originations could be enlarged, improving the understanding of defect influences. Besides improving material quality by supplying a broad field of information about defect mechanism to the PV production industries, some kind of defects provide properties which allow their aimed usage to improve different kind of electrical devices. These special defects could be used to produce Si light emitters for on-chip optical data transfers or certain kinds of transistors for example. Even after all these years, from 1953 to present there is simply an uncompleted amount of knowledge at our disposal. This lack of understanding has to be reduced.

Aim and outline of this work

The investigations for this work were performed within the scope of the "SolarWinS" research cluster, as well as of the PVcomB project (Competence Centre Thin-Film and Nanotechnology for Photovoltaics Berlin) - Teilvorhaben 6 Analytik. The focus of the presented work will be the investigation of different defects with the aim to describe their properties, explain the observations and if possible suggest an origin for the defect behavior. For this purpose, it is necessary to combine luminescent spectroscopic measurement methods, to identify characteristic spectra, with electron beam induced current (EBIC) investigations to also include the total recombination as well. To examine the structural influence of the sample on the observed behavior additional electron backscattered diffraction (EBSD) and transmission electron measurements (TEM) have to be included. The combination and correlation of all differently gathered measurement data should enable a satisfactory reply to the question what provokes the remarkable behavior in each investigated case.

After the introduction and this outline, the second chapter is dedicated to explaining the basic knowledge that is essential to follow the investigations and conclusions hereafter. In addition, the experimental methods used, their measurement setup, the necessary sample preparation steps, how the signals arose, and how they could be analyzed will be presented.

The third chapter provides a wide overview of material defect features observed during investigations for this work. This chapter is subdivided into bulk multicrystalline silicon (mc-Si) material and investigations performed at thin-film silicon. Whereby the mc-Si part is differentiated into radiative features, mainly observed with cathodoluminescence (CL), and non-radiative features, appeared during EBIC investigations. The following

thin-film part includes successful performed measurements and the difficulties due to the special sample setup.

Subsequently, the work is restricted to the occurrence of two selected utterly different defects. Therefore, there are two more chapters to describe each of the two defects.

The fourth chapter is solely focused to the investigation of the appearance of the Di luminescence at 0.93 eV. The goal of the investigations described, performed, and combined in this chapter is the suggestion of a possible origin for the intense luminescence.

The fifth chapter is about the electrical behavior of twin boundaries at low temperatures below 30 K, observed with EBIC measurements. Here it is intended to explain why such a behavior could occur.

The results are summarized in the sixth chapter, which is also the last one.

2 Basic knowledge

In this chapter, the necessary fundamentals are presented to provide a short insight into semiconductor physics. At first the properties of carriers in intrinsic as well as in doped semiconductors are briefly shown. Subsequently, possible kinds of defects in silicon are explained, before radiative and non-radiative recombination processes are introduced. The experimental methods used are presented in the final section of this chapter, including how the measurement method works in general, which sample preparation steps are necessary, how the signal arose and how the collected data could be analyzed for the mainly used methods. The information provided should support the discussions and the presented investigations in the following experimental chapters.

2.1 Semiconductor properties

Semiconductor properties are strongly dependent on the carrier concentration and the carrier mobility. Therefore, it is necessary to provide a brief overview concerning how they can be influenced.

2.1.1 Carrier concentration

To describe the carrier concentration it is necessary to distinguish between the intrinsic semiconductors and doped ones. Doping is performed to provide more carriers, and thus a better conductivity in the material.

Intrinsic semiconductor

For the intrinsic case without any dopants, the carrier concentration can be calculated with the Fermi-statistic $f(E,T)$ and the density of states of holes in the valence band $D_v(E)$.

The concentration of electrons in the conduction band can be calculated respectively.

$$p_v = \frac{1}{V}\int_{-\infty}^{E_v} D_v(E)[1 - f(E,T)]dE$$

With the effective mass of holes m_h^*, the Boltzmann constant k, the temperature T, the valence band energy E_v, the energy of the Fermi level E_F and the Planck constant h, the hole concentration can be simplified after Sze [90]:

$$p_v = \underbrace{2\left(\frac{2\pi m_h^* kT}{h^2}\right)^{\frac{3}{2}}}_{p_{eff}^v} e^{\frac{E_v - E_F}{kT}} \tag{2.1}$$

Where the effective density of states in valence band are given by p_{eff}^v.

Doped semiconductor

In the case of doped semiconductors, the induced carriers have to be take into account. Using p-type doped silicon, there is the concentration of acceptors N_A with the density of neutral N_A^0 and ionized acceptors N_A^-:

$$N_A = N_A^0 + N_A^-$$

The number of holes at acceptor level E_A is given by:

$$p_A = N_A^0 = \frac{N_A}{e^{\frac{E_F - E_A}{kT}} + 1}$$

and the density of ionized acceptors:

$$N_A^- = N_A - \frac{N_A}{e^{\frac{E_F - E_A}{kt}} + 1}$$

For small temperatures, it can be assumed that the most holes p_v in the valence band originate from the acceptor level (E_A) rather than the conduction band. With equation 2.1 and $p_v \simeq N_A^-$ the hole concentration can be calculated through:

$$\frac{p_v}{p_{eff}^v} e^{-\frac{E_v}{kT}} = e^{\frac{-E_F}{kT}}$$

$$p_v \simeq \frac{N_A}{1 + \frac{p_v}{p_{eff}^v} e^{\frac{E_A - E_v}{kT}}}$$

After solving this equation and with the distance E_d between the acceptor level and band edge, for low temperatures the density of holes can be given by:

$$4 \frac{N_A}{p_{eff}^v} e^{\frac{E_d}{kT}} \gg 1 \tag{2.2}$$

$$\Rightarrow p_v \simeq \sqrt{N_A p_{eff}^v} e^{-\frac{E_d}{2kT}} \tag{2.3}$$

An example for the temperature dependence of the carrier concentration is shown in Fig.2.1.

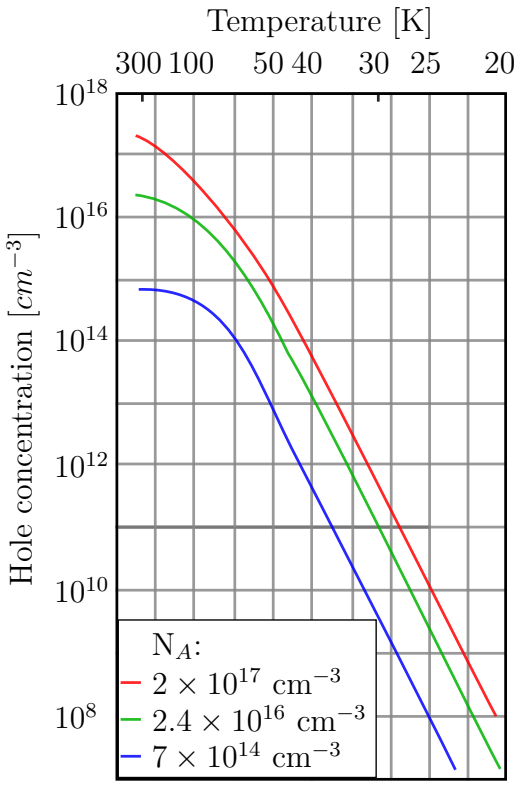

Figure 2.1: Temperature dependence of the carrier concentration for p-type single-crystal silicon containing boron as dopant, after Morin and Maita [67].

The qualitative temperature dependence of the carrier concentration together with the corresponding Fermi energy temperature dependence is shown in Fig.2.2.

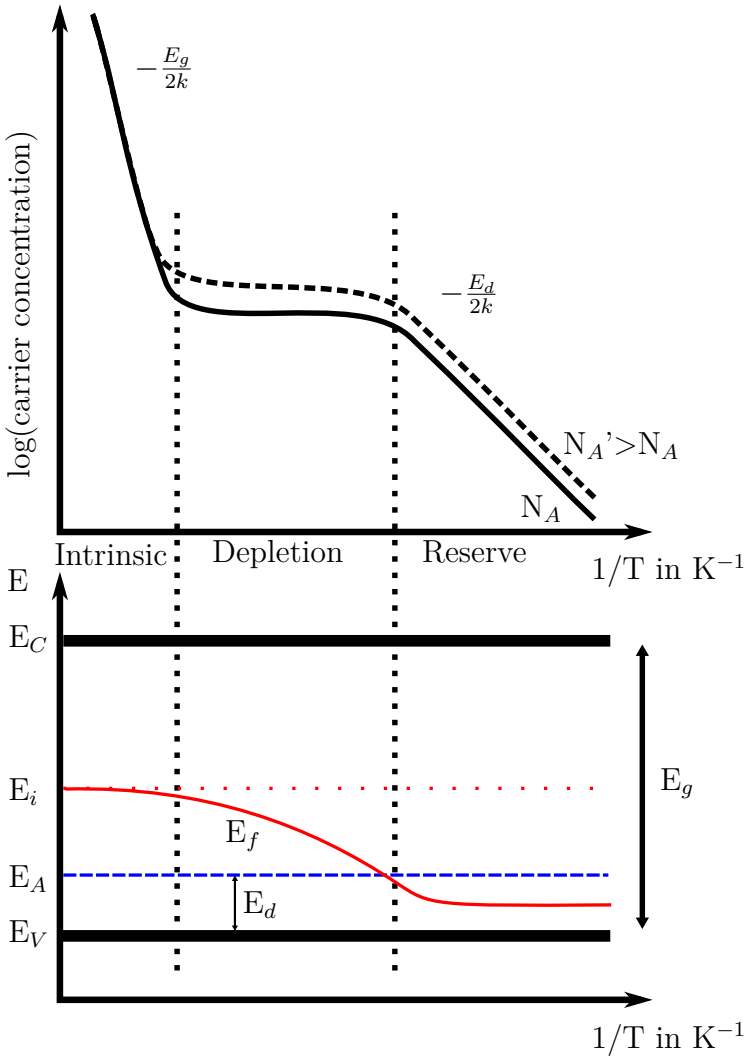

Figure 2.2: Qualitative temperature dependence of the carrier concentration and corresponding temperature dependence of the Fermi energy.

The Fermi energy influences the later in section 2.4.2 discussed EBIC contrast. Deep defect levels, which are located deeply in the band gap, near the Fermi energy, become already recombination active at room temperature, while shallow defect levels near the band edge, far away from the Fermi energy, show a recombination contrast after cooling, at a certain lower temperature.

2.1.2 Carrier mobility

The resistivity of the semiconductor is indirect proportional to the mobility of the carriers and is affected by scattering mechanism in the material, which is mainly induced by the lattice μ_a (acoustic phonon scattering) and ionized impurities μ_i. The combined mobility is after Sze [91]:

$$\mu = \left(\frac{1}{\mu_a} + \frac{1}{\mu_i} \right)^{-1}$$

With the resistivity ρ, the current density J, the electric field ξ and the conductivity σ [91]:

$$\begin{aligned} J &= \sigma\xi \\ \rho &= \frac{1}{\sigma} \qquad\qquad = \frac{1}{q(\mu_n n + \mu_p p)} \end{aligned}$$

where μ_n and μ_p are the mobilities of electrons and holes. The conductivity for p-type semiconductors with $p \gg n$:

$$\sigma = q\mu_p p$$

The temperature dependent carrier mobility, for some published p-type silicon data sets, with the acceptor concentration N_A, is shown in Fig.2.3.

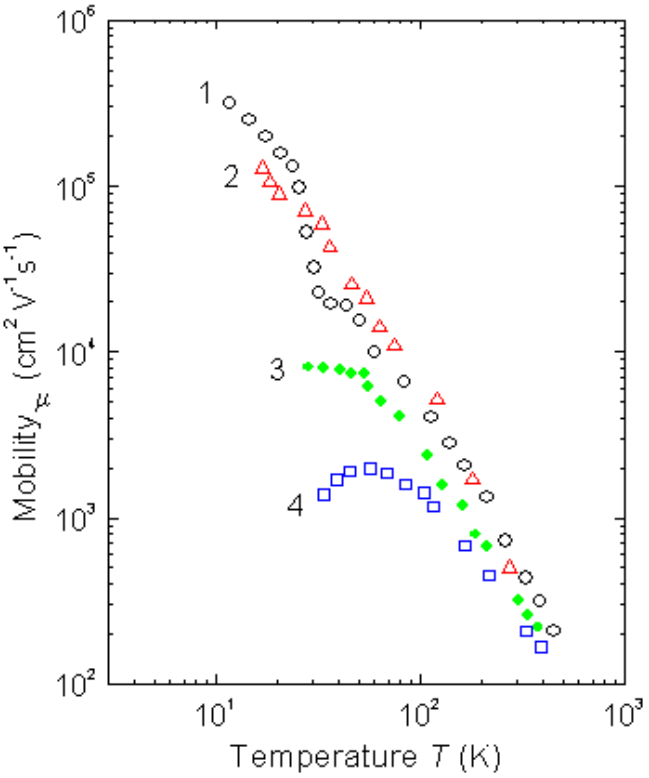

Figure 2.3: Temperature dependence of the carrier mobility: (1)Ottaviany et al. [71] tof-technique : $N_A = 10^{12}\ cm^{-3}$,(2)Logan and Peters [56]photo-Hall-effect:$N_A \sim 10^{14}\ cm^{-3}$, Morin and Maita [67] Hall effect:(3)$N_A \sim 2.4 \times 10^{16}\ cm^{-3}$ and (4)$N_A \sim 2 \times 10^{17}\ cm^{-3}$.

2.1.3 Space-charge-region (SCR)

The electric field that influences the carrier motion is dependent of the build-in depletion layer. At a metal-semiconductor contact a depletion layer is formed, which is schematically shown in Fig.2.4.

The Fermi-level of the metal and the semiconductor are shifted with $\Phi_M - \Phi_H$, where $e\Phi_M$ is the work function of the metal and for the semiconductor $e\Phi_H = e\chi + eV_n$ with the distance between Fermi- and vacuum level eV_n and the electron affinity $e\chi$, the distance between conduction band and vacuum level.

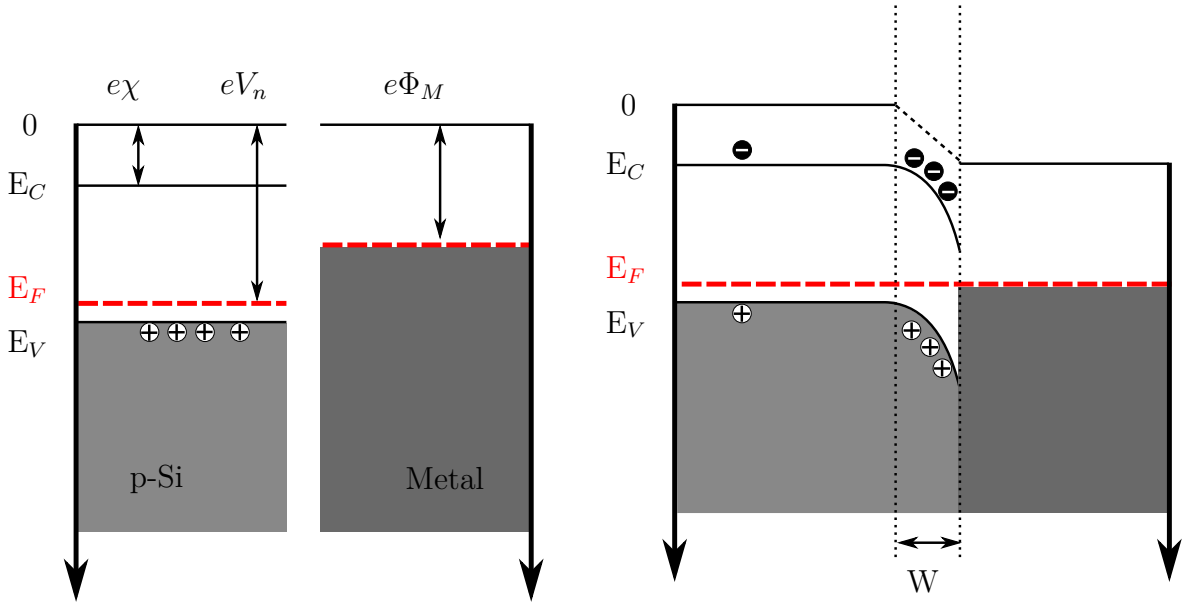

Figure 2.4: Schematic band bending caused by forming of a p-type semiconductor-metal contact with depletion layer width W.

The formed depletion layer width W can be calculated with the dopant concentration N_D and the assumption that $\rho \simeq qN_D$ for $x < W$ and $\rho \simeq 0$ and $\frac{\mathrm{d}V}{\mathrm{d}x} \simeq 0$ for $x > W$ to those of an one-sided abrupt pn-junction after [22]:

$$W = \sqrt{\frac{2\epsilon_s}{qN_D}(\Phi_M - \Phi_H)}$$

The capacitance C can be calculated with the space charge Q_{sc}

$$\begin{aligned} Q_{sc} &= qN_D W & &= \sqrt{2q\epsilon_s N_D(\Phi_M - \Phi_H)} \\ C &= \frac{\delta Q_{sc}}{\delta V} & &= \frac{\epsilon_s}{W} \end{aligned}$$

2.2 Recombination processes

Through excitation with light or electron beam, excess carriers will be built inside the semiconductor. To reach the equilibrium state again, recombination processes take place. Under existence of an electrical barrier near the generation volume the electron-hole pairs will be separated by the electrical field when they reach the barrier and electrons will drift to the positive and holes to the negative pole. Without the influence of an additional electrical field, the build carriers diffuse freely. They will be recom-

bined radiatively or non-radiatively. With the excess carrier concentration Δn and their lifetime τ the recombination rate R is generally defined by $R = \frac{\Delta n}{\tau}$ where by

$$\frac{\Delta n}{\tau} = \frac{\Delta n}{\tau_{BB}} + \frac{\Delta n}{\tau_{DRL}} + \frac{\Delta n}{\tau_{SRH}} + \frac{\Delta n}{\tau_{Auger}} + \frac{\Delta n}{\tau_s} \tag{2.4}$$

the lifetimes for total, band-to-band (BB), defect-related luminescence (DRL), Shockley-Read-Hall (SRH), Auger and surface recombination are given by τ, τ_{BB}, τ_{DRL}, τ_{SRH}, τ_{Auger} and τ_s. Instead of the lifetime, it is also common to use the diffusion length L of the excess carriers, reflecting the average length of carrier diffusion within their lifetime. With the diffusion constant D the diffusion length is:

$$L = \sqrt{D\tau} \tag{2.5}$$

2.2.1 Radiative recombination

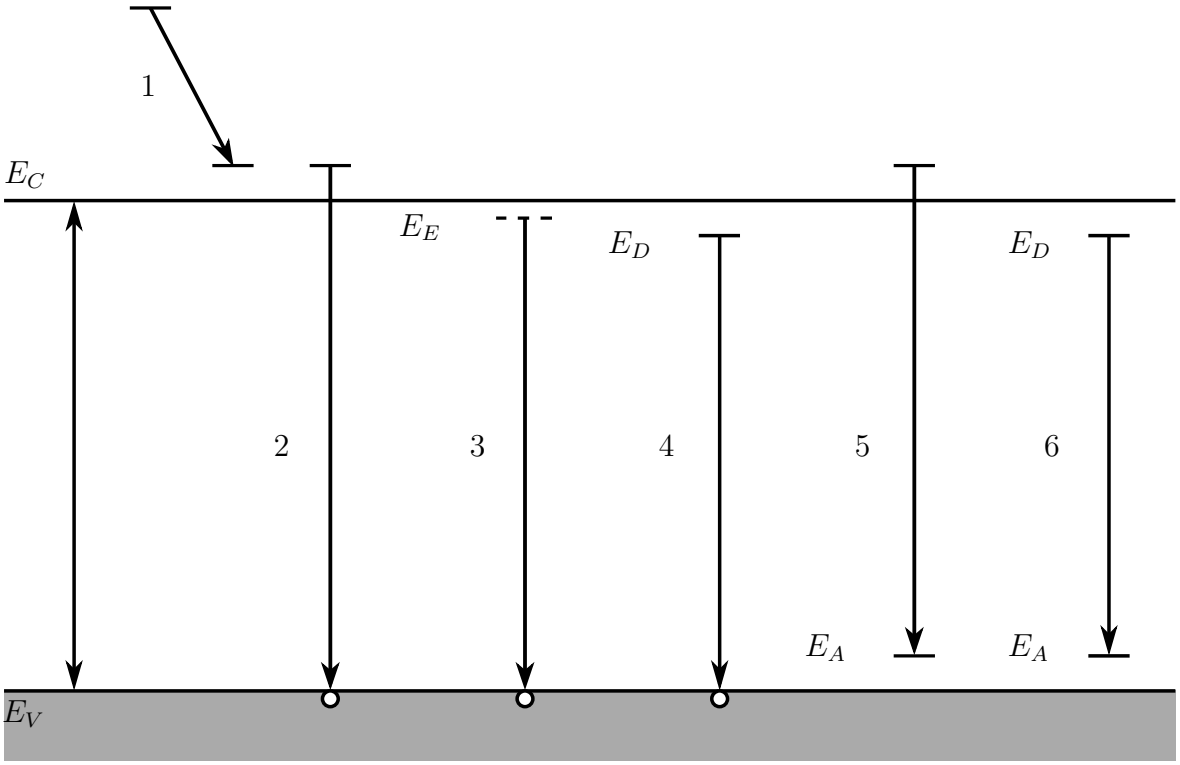

Figure 2.5: Schematic transitions between conduction band (E_L), valence band (E_V) and exciton (E_E), donator (E_D) and acceptor (E_A) levels at semiconductors after Yacobi and Holt [99].

Figure 2.5 presents some simplified radiative transitions. Process *(1)* is an intraband transition, an exciton will be excited (E_E) over the edge of the conduction band with following relaxation. The result of this thermalization procedure can be either an emission of a phonon and a photon or simply an emission of phonons. In *(2)*, an interband transition is shown featuring a radiative recombination between electrons in the conduction band (E_C) with holes in the valence band (E_V). The resulting radiation is called band-to-band luminescence (BB). The third one *(3)* is an excitonic transition, which is only visible at low temperature. Free excitons as well as bounded ones caused by soilings can lead to this kind of transition. The transitions *(4)* to *(6)* are between localized states in the band gap induced by soilings or doping (donor E_D and acceptor E_A). Resulting luminescence is called defect-related luminescence (DRL).

Band-to-band luminescence

After the excitation process (electron will be excited from valence to conduction band and leaving a hole there) electrons and holes aspire to reach the equilibrium state again and thus they will recombine. The recombination path differs depending on which kind of semiconductor was excited, namely whether it was a direct or indirect one. Both cases are schematically drawn in Figure 2.6.

In direct semiconductors, electrons from the conduction minimum will be recombine with holes from the valence band maximum, which is at the same position in reciprocal space. In indirect semiconductors, the position of conduction band minimum and valence band maximum differs and for the direct band transition an additional phonon is necessary. This is why these indirect BB transition are less probable than direct BB transitions.

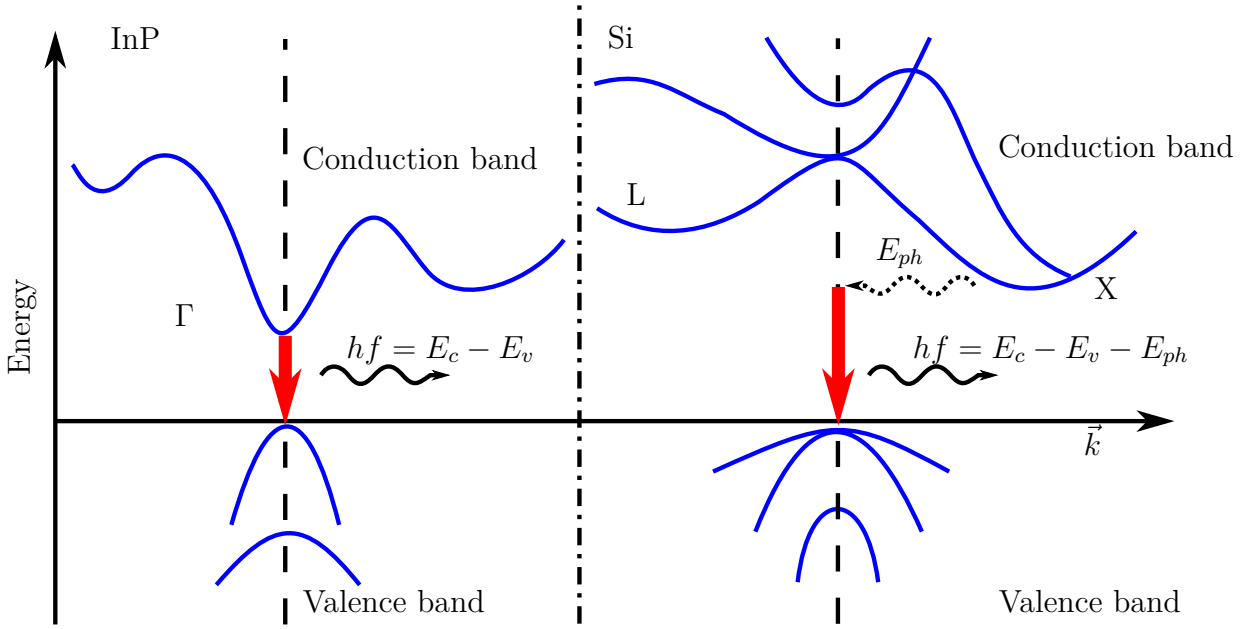

Figure 2.6: Energy transfer from conduction band (E_c) into the valence band (E_V) with emission of photon (hf)in direct (InP left) and indirect semiconductor (Si right) with additional participation of a phonon (E_{ph})(right); after Liang und Bowers [54].

The recombination rate R includes the constant radiative recombination coefficient B of the BB transition [77], is proportional to the product of electrons n and holes p and is equal to the generation rate G of excess carriers.

$$R = Bnp = G$$

where n and p after excitation can be denoted as:

$$n = n_0 + \Delta n$$
$$p = p_0 + \Delta p$$

with excess carriers Δn and Δp, which are usual due to light absorption or electron beam injection $\Delta n = \Delta p$. Hence, the recombination rate can be represented as the sum of the excess recombination rate ΔR and recombination rate at equilibrium condition R_0:

$$R = R_0 + \Delta R$$

For p-type semiconductors $p_0 \gg n_0$, the recombination rate of excess carriers follows as:

$$\begin{aligned}\Delta R &= Bnp - Bn_0p_0 = B(n_0 + \Delta n)(p_0 + \Delta p) - Bn_0p_0 \\ &= B(n_0 + p_0)\Delta n + B\Delta n^2\end{aligned}$$

The term $B\Delta n^2$ can be neglected under the assumption of low injection $\Delta n \ll p_0$ where the amount introduced carriers is negligible compared to the concentration of majority carriers. The excess recombination rate is given by:

$$\Delta R \approx B(n_0 + p_0)\Delta n$$

In contrast to low injection, $B\Delta n^2$ becomes dominant if high injection conditions are valid $\Delta n \gg p_0$, which leads to

$$\Delta R = B\Delta n^2$$

Defect-related luminescence in silicon

Besides the previously described BB luminescence, another kind of luminescence is that involving defect levels within the band gap. The energy of luminescence in this case conforms the energetic distance between the defect level and the band edge. Here, the transition from conduction band to the defect level as well as from defect level to the valence band are possible. Probably the most discussed and investigated radiative transitions are the so called D-lines D1-D4 [16], which are first observed in the 70th and related to dislocations. At low temperature, it is possible to observe all four luminescence transition with i.e. photoluminescence (PL). A good example of how it could look in a PL spectrum is shown in Fig.2.7 from Arguirov [2]. At room temperature, from these four D-lines, only D1 could be observed [88], whereas the shallow levels of the other luminescences will be suppressed. Drozdov et al. [16] reported the spectral positions at helium temperatures: D1 0.812 eV, D2 0.875 eV, D3 0.934 eV and D4 1.0 eV. Despite many long term investigations, the entire mechanism of the D-lines and there exact origin are still not completely understood.

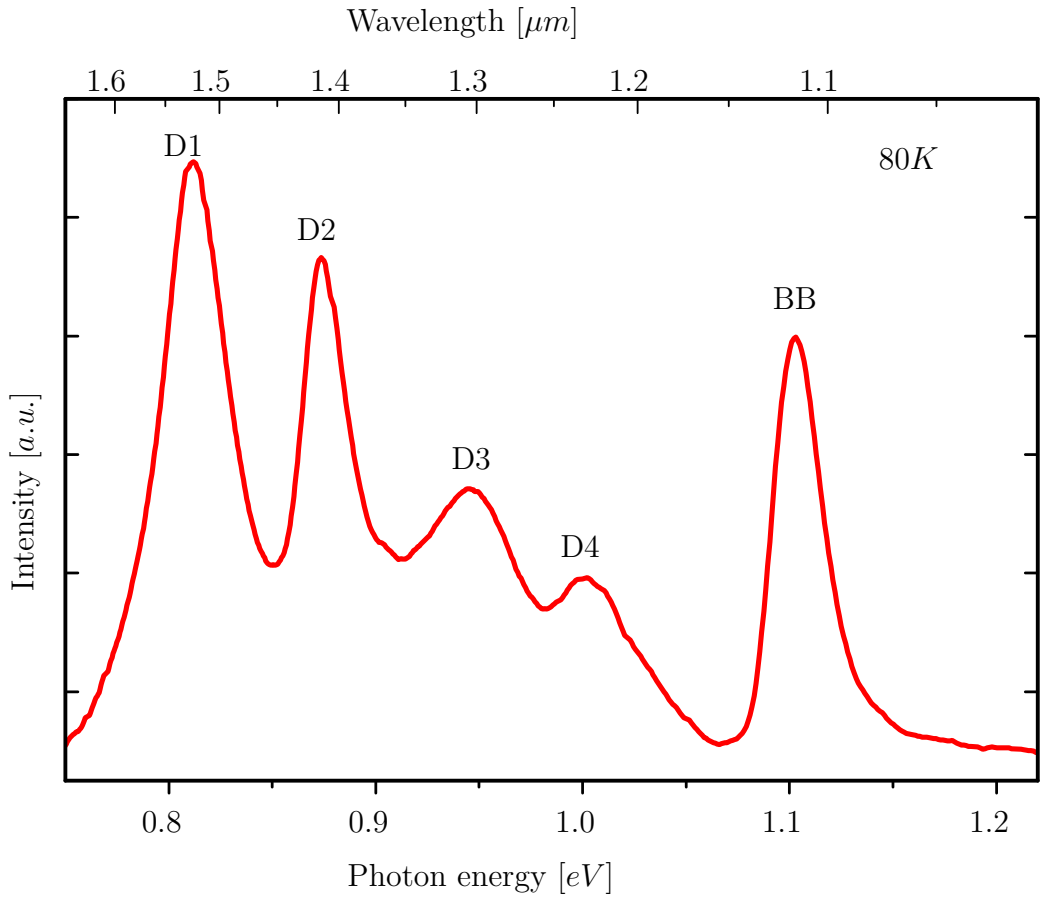

Figure 2.7: PL spectrum from plastic deformed silicon at 80 K. D1-D4 as well as BB are observed [2].

For the D1 luminescence, there are several different suggestions of possible origins reported. It could be associated with defects along the dislocation line (kinks and jogs) [53; 85]. Moreover, strong D1 luminescence was observed at the crossing points of screw dislocations by Mchedlidze et al. [64]. Other suggestions are stress-related deep and shallow dislocation levels in the band gap of Silicon [76; 49], clusters of intrinsic atoms close or at the dislocation lines [29; 6], oxide precipitates at or near to dislocations [4; 5], and recent investigations by Mchedlidze et al. [62; 61] on dislocation networks in bonded Si wafers, presenting a model for grain boundaries (GBs), suggesting that the intensity and shape of dislocation-related luminescence spectra strongly depend on the structure of the network. Taking the lattice distortion into account, which could induce a strain field around the dislocation, Lelikov's [53] suggestion should also take place here. According to Lelikov [53], these strain fields could build one-dimensional energy bands that are dependent of the dislocation Burgers vector $\vec{b}$. The spectral position of the radiative emission E_{lum} could be estimated with E_g the band gap energy, the lattice

constant a, the edge component b_e of the Burgers vector and a constant A, which is related to the deformation potential and the mean effective carrier mass:

$$E_{lum} \approx E_g - A \left(\frac{b_e}{a} \right)^2$$

Dislocation type	**b/a**	**estimated E_{lum}[eV]**	**observed E_{lum}[eV]**
Screw non-split	1/2[110]	/	/
30° partial glide	1/6[211]	1.140	/
stair-rod partial	1/6[110]	1.125	1.030[53]
90° partial glide	1/6[112]	1.040	1.025[53]
Frank Partial	1/3[111]	0.900	0.870(D2)[76]
60° non-split	1/2[101]	0.870	0.84(D12)[76]
Lomer-Cottrell	1/2[110]	0.770	0.807(D1)[76]

Table 2.1: One-dimensional band gap, build through strain field around dislocations. Calculated luminescence in comparison to experimentally observed [53].

In his work, Lelikov [53] compared estimated band gap modifications for different kinds of dislocations with spectral features (Table 2.1). The estimated E_{lum} of about 0.9 eV, which he has dedicated to Frank Partials, almost corresponds to the later discussed luminescence in chapter 4. In addition, Sekiguchi [84; 85] shows a spatial correlation between dislocation-related luminescence and dislocations introduced by plastic deformation. He observed a domination of D1 and D2 in regions of intersecting slip lines whereas D3 and D4 originate along glide dislocations or edge dislocations [62]. Furthermore, there are reports that contribute luminescence in the range around D1 to oxygen precipitates (OP) [62; 95]. The discussion, which lines are D1 or OP, persisted over the last ten years and extends far beyond this work. However, some observed spectra indicating oxygen involvement are presented in section 3.1.

2.2.2 Non-radiative recombination

Besides the radiative transitions, also non-radiative recombinations exist. Aside from *(1)* in Figure 2.5, there is the so-called Auger process, whereby energy of a former electron transition will be absorbed by another electron, which will be excited to a higher energetic level inside the conduction band. Subsequently, an emission of this electron or heating of the material through phonon emission is possible [72]. Furthermore, the Shockley-Read-Hall (SRH) recombination particularly as well as the surface recombination should be mentioned, whereby former absorbed energy in form of thermal energy is transferred to the material through lattice vibration.

Shockley-Read-Hall recombination

In indirect semiconductors, non-radiative recombinations are the most expected recombination mechanism. Defects cause built-in levels in the band gap that could act as traps for minority carriers. The recombination rate is given by [87; 23].

$$R_{SRH} = \frac{np - n_i^2}{\tau_p(n + n_l) + \tau_n(p + p_l)} \tag{2.6}$$

The electron and hole concentration is denoted with n and p whereby n_i^2 is the intrinsic carrier concentration under equilibrium condition. τ_n is the lifetime for electrons when the recombination centers are entirely empty while the lifetime for holes, if the centers are occupied by electrons, is given by τ_p:

$$\tau_p = \frac{1}{\sigma_p v_{th,p} N_t} \qquad \text{and} \qquad \tau_n = \frac{1}{\sigma_n v_{th,n} N_t}$$

τ_p and τ_n are related to N_t the density of the recombination centers, their capture cross section for holes σ_p and electrons σ_n as wells as the thermal velocities of the carriers $v_{th,p}$ or $v_{th,n}$. The energy level of the defect states are given by n_l and p_l, which are the equilibrium electron and hole concentrations when the Fermi level coincides with the energy level E_t of the trap in the band gap.

$$n_l = n_{eff}^c e^{\frac{E_t - E_C}{kT}} \qquad \text{and} \qquad p_l = p_{eff}^v e^{\frac{E_V - E_t}{kT}}$$

where E_C and E_V are the conduction and valence band energy, k is the Boltzmann constant and T is the temperature. n_{eff}^c and p_{eff}^v denotes the effective densities of states in conduction and valence bands.

For a n-type sample $n_0 \gg p_0$ R_{SRH}, equation (2.6) can be simplified to:

$$R_{SRH} = \frac{np - n_i^2}{\tau_p(n + n_l)} \tag{2.7}$$

At low injection ($\Delta n = \Delta p \ll n_0, n = n_0 + \Delta n, p = p_0 + \Delta p,$ and $n_0 p_0 = n_i^2$), SRH recombination is usually the dominating recombination in silicon. In doped material, the change of majority carrier concentration through injection can be neglected; therefore, it is possible to simplify equation (2.7) with the minority carrier lifetime τ_{SRH} and their concentration Δn:

$$R_{SRH} \approx \frac{\Delta n}{\tau_{SRH}}$$

Surface recombination

The surface recombination is a special kind of SRH recombination, which also involves intraband transfers. "The subscript "s" refers to the appropriate quantity at the surface" [82]. According to equation (2.6) after [82], with the recombination velocities of holes ϑ_p and electrons ϑ_n, the recombination rate ca be simplified to:

$$R_s = \frac{\vartheta_n \vartheta_p (p_s n_s - n_i^2)}{\vartheta_n (n_s + n_{ls}) + \vartheta_p (p_s + p_{ls})}$$

under the assumption that the trap density N_{ts} at the surface is constant. p_s and n_s design the hole and electron densities at the surface.

Auger recombination

This three-particle process becomes important in highly doped silicon or under high injection conditions. Energy that is released through carrier recombination is transfered to an additional carrier, an electron in case of so-called eeh process or to another hole, ehh process [17].

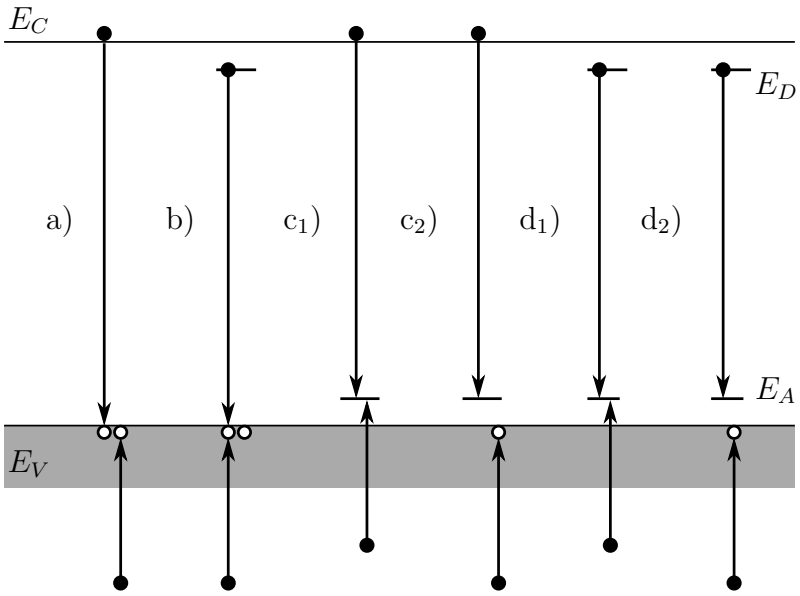

Figure 2.8: Schematic drawing of possible Auger recombination processes in p-semiconductors after Pankove [72].

In Fig.2.8, according to Pankove [72] some of the possible transitions are shown for p-type material. Through energy release in BB transition, a) the second hole will be excited deep from the valence band. The process *b)* is a donor to valence band transition, a second hole will be excited. The transitions from conduction band to acceptors are shown in c_1*)* and c_2*)*. Furthermore, transitions from donor to acceptors *d)* are conceivable.

The recombination rate R_{Auger} is dependent on the concentration of three particles that take part at the recombination:

$$R_{Auger} = C_n n^2 p + C_p n p^2 \tag{2.8}$$

where C_n and C_p are the Auger coefficients for eeh and ehh process. The lifetimes can be estimated from equation (2.8) for low τ_{lo} and high τ_{hi} injection in dependents of the doping type. For p-type silicon:

$$R_{lo} = C_p N_A^2 \Delta n \qquad \Rightarrow \qquad \tau_{lo} = \frac{1}{C_p N_A^2}$$

$$R_{hi} = C_a \Delta n^3 \qquad \Rightarrow \qquad \tau_{hi} = \frac{1}{C_a \Delta n^2}$$

with the density of acceptors N_A and the ambipolar Auger coefficient $C_a = C_n + C_p$ [32].

2.3 Crystal defects

Defects in semiconductor materials as shown in Fig.2.9 are distinguished by means of their dimension. Therefore, we have zero-dimensional defects also called point defects like intrinsic defects or extrinsic defects. One-dimensional defects describe dislocations. Stacking faults, grain and phase boundaries are counted among the two-dimensional defects, while three-dimensional defects include precipitates and voids. All of these defects could influence the mechanical, electrical and optical properties of silicon.

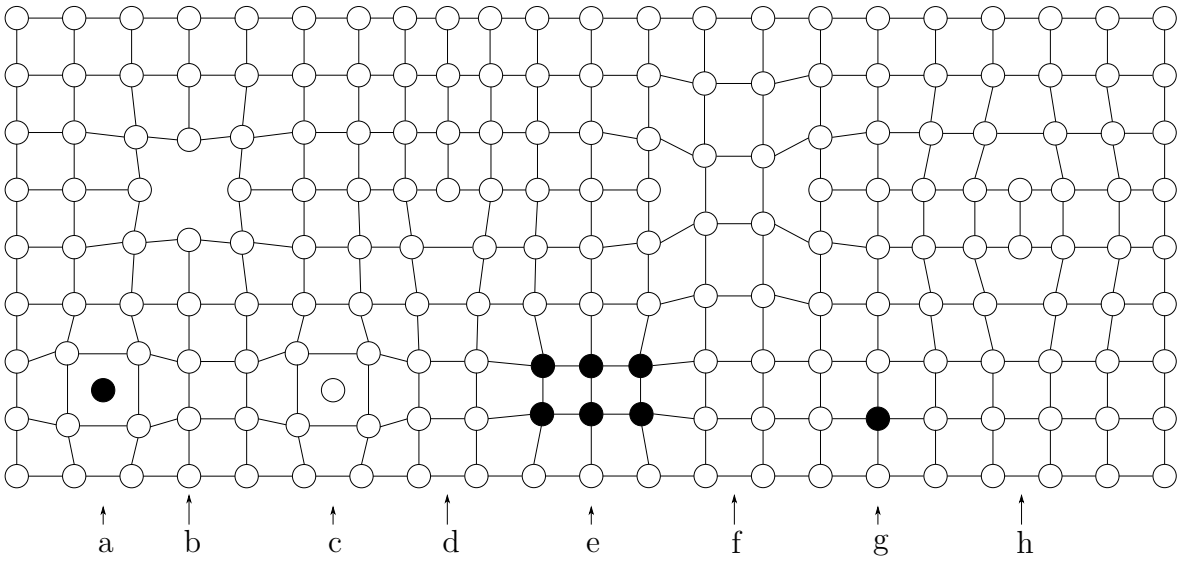

Figure 2.9: Schematic crystal lattice defects drawing after Föll et al. [20]: *a)* interstitial impurity atom, *b)* vacancy, *c)* self-interstitial atom, *d)* edge dislocation, *e)* precipitate of impurity atoms, *f)* vacancy type dislocation loop, *g)* substitutional impurity atom, *h)* interstitial type dislocation loop.

2.3.1 Point defects

Vacancies and self-interstitials, which are counted among the intrinsic point defects, are shown in Figure 2.9 *b)* and *c)*. Extrinsic point defects like Figure 2.9 *a)* or *g)* could include doping atoms, transition metals, interstitial oxygen atoms or carbon substitutional atoms, for example. These defects could form energy levels in the band gap, which influence the transitions in the material.

2.3.2 Dislocations

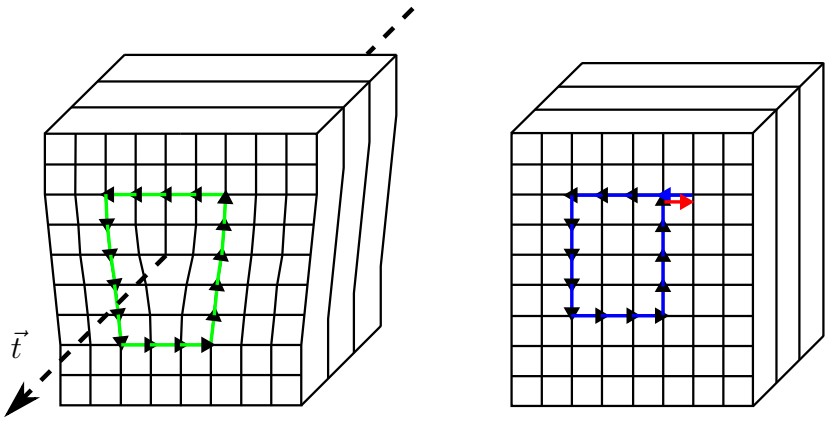

Figure 2.10: Schematic crystal lattice with edge dislocation after Föll [19]; green: closed Burgers circuit around dislocation, blue: same chain of base vectors in perfect reference lattice without dislocation will not close, red: resulting Burgers vector $\vec{b}$ close circuit, black dashed: dislocation line $\vec{t}$.

Dislocations are formed during the crystal growth process, for example due to lattice mismatch between the interface of two material layers, mechanical stress, which could be produced through high temperature steps, or resulting different local thermal expansions. Dislocations are characterized by their Burgers vector $\vec{b}$.

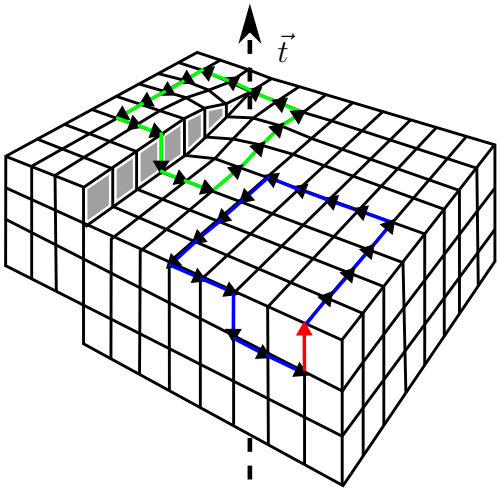

Figure 2.11: Schematic crystal lattice with screw dislocation after Föll [19]; green: closed Burgers circuit around dislocation, blue: same chain of base vectors in perfect reference lattice without dislocation will not close, red: resulting Burgers vector $\vec{b}$ close circuit, black dashed: dislocation line $\vec{t}$.

The formation of the Burgers vector is presented in Figure 2.10 for an edge dislocation and in Figure 2.11 for a screw dislocation. It is evident that the circuit of base vectors around the dislocation does not close in the perfect reference lattice. The missing vector is called Burgers vector $\vec{b}$ and, in the case of an edge dislocation, is located perpendicular to the dislocation line $\vec{t}$, and in the case of a screw dislocation, parallel to the dislocation line $\vec{t}$.

Dislocation line charge

In p-type silicon, defect levels related to dislocations can be occupied with holes forming a positive line charge, respectively for n-type material the line will be negatively charged due to the occupation through electrons. Around the dislocation, a space charged region with ionized negatively charged acceptor atoms is formed 2.12 *b)*. In case of n-type Si, the surrounding so called Read cylinder will comprise ionized positively charged donor atoms. To compensate the dislocation charge, the valence and conduction band will be bended, a potential barrier is formed in the band schema 2.12 *a)*.

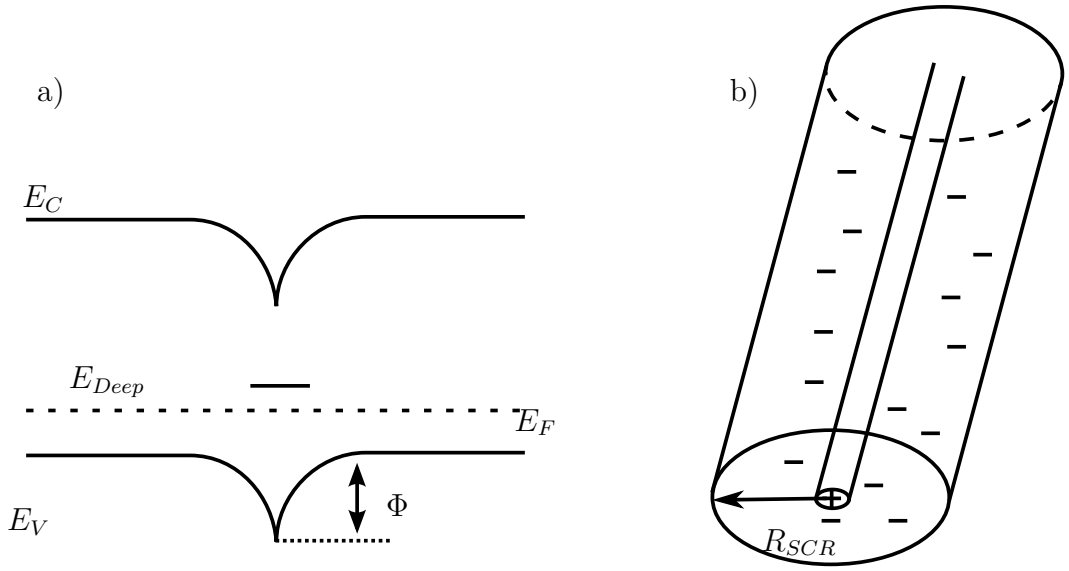

Figure 2.12: Model of charged dislocation in p-type material. a) Space charge region and band bending at dislocation. b) Space charge cylinder with charged acceptors after Kittler and Reiche [39].

2.3.3 Grain boundaries and stacking faults

Grain boundaries (GBs) are formed during the growth process of multicrystalline silicon. Neighboring crystallites touching each other and the interface between them is called grain boundary, which is described by the orientation of these two grains to each other. For certain types of GBs, it is possible to categorize them according to the coincidence site lattice (CSL) theory, whereby the number of exactly coincide lattice points from one lattice with the rotated second one is taken into account. The coinciding points form some kind of superstructure. A definition how the GB will be divided is given in [19] " The relation between the number of lattice points in the unit cell of a CSL and the number of lattice points in a unit cell of the generating lattice is called Σ; it is the unit cell volume of the CSL in units of the unit cell volume of the elementary cell of the crystals." The always odd Σ value for a GB describes the orientation between the two adjacent grains unambiguous. A small Σ value, whereby $\Sigma 1$ means an almost perfect crystal without any boundary, denotes GBs with just a slight misorientation between the two grains. According to Föll [19] GBs that are close to the $\Sigma 1$ orientation are called small angle grain boundaries. The GB with the highest symmetry between the grains is called twin boundary (TB) and is described with $\Sigma 3$.

Twin boundaries are a special kind of GBs observed in crystals. They are highly symmetrical with no change of bond length or angles at the mirror plane (Fig.2.13). Therefore, the grain boundary energy per unit area is smaller here than at other GBs. Furthermore, both crystals should bend together without any straining of the lattice due to the high symmetry. The twin boundaries on {111} planes are called coherent twin boundaries; they are the simplest ones and have the smallest energy. All other possible twins on different planes are called incoherent. The twin boundaries are also called $\Sigma 3$ boundaries according to the coincidence site lattice (CSL).

If it is not possible to classify the GB according to the CSL theory, the degree of misorientation between the grains is used for description. They will be denoted as high angle GBs if the twist or tilt angles between two grains are larger than 15 degree, otherwise they are called small or low angle GBs [15]. GBs, which are due to their misorientation far to a coincidence relationship, are also referred as random GBs.

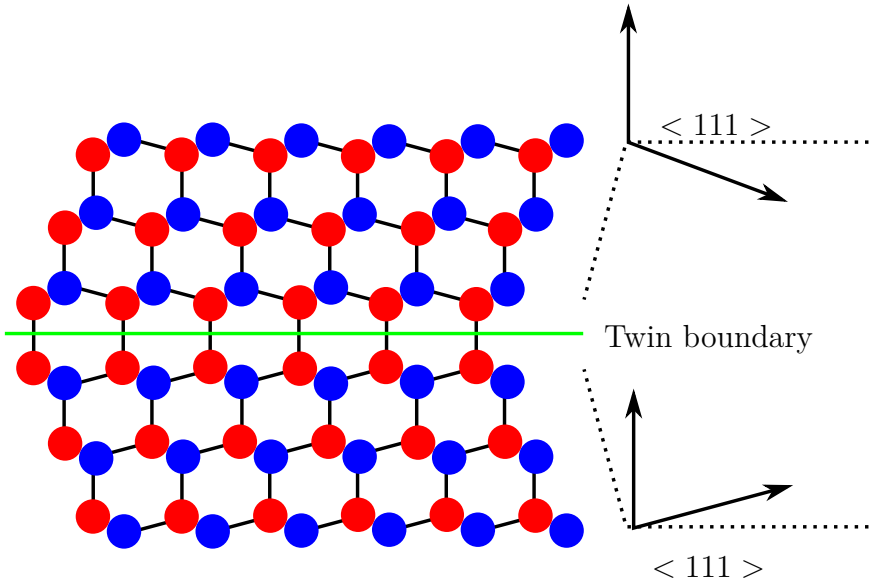

Figure 2.13: Schematic drawing of the crystal lattice of a twin boundary after Föll [19].

Stacking faults are defects in the planes of the crystal lattice. As we consider the sequence of three neighboring (111) planes from the silicon diamond structure ...ABCABCABC...we talk about a stacking fault if we remove an existing plane or insert an additional plane (Figure 2.14).

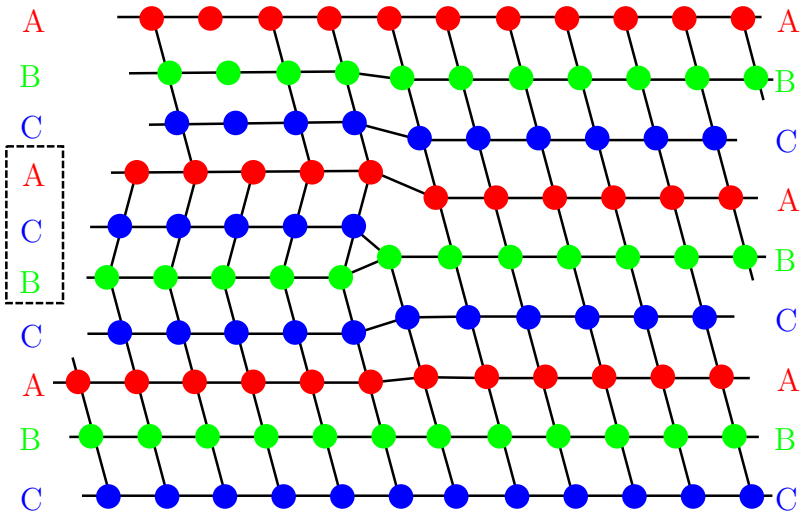

Figure 2.14: Schematic crystal lattice with extrinsic stacking fault after Föll [19].

The extrinsic stacking fault in Figure 2.14 shows an edge dislocation, which is released by interstitials. The Burgers vector of this dislocations is $\vec{b} = \pm\frac{a}{3} < 111 >$ and thus it is not a translation vector of the fcc silicon lattice. Dislocations with this special kind of Burgers vector are called Frank partial dislocation.

Partial dislocations were built because perfect dislocations may split up into two partials to lower their total energy. This splitting is shown for a dislocation with a Burgers vector $\vec{b} = \frac{a}{2}[110]$ in Fig.2.15.

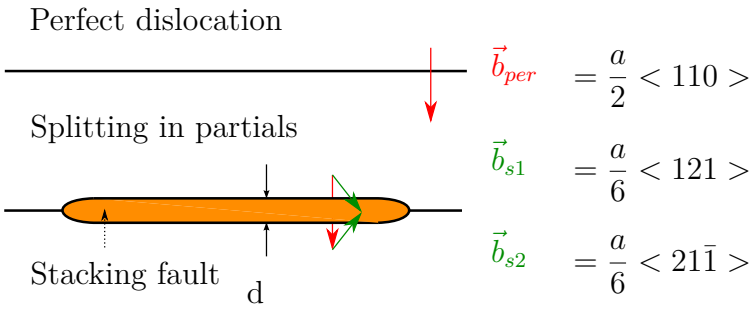

Figure 2.15: Schematic drawing of a perfect dislocation splitting in two Shockley partials in a distance d with a stacking fault between the partial dislocations after Föll [19].

A cross sectional view (Fig.2.16) of this kind of splitting could be found in [26].

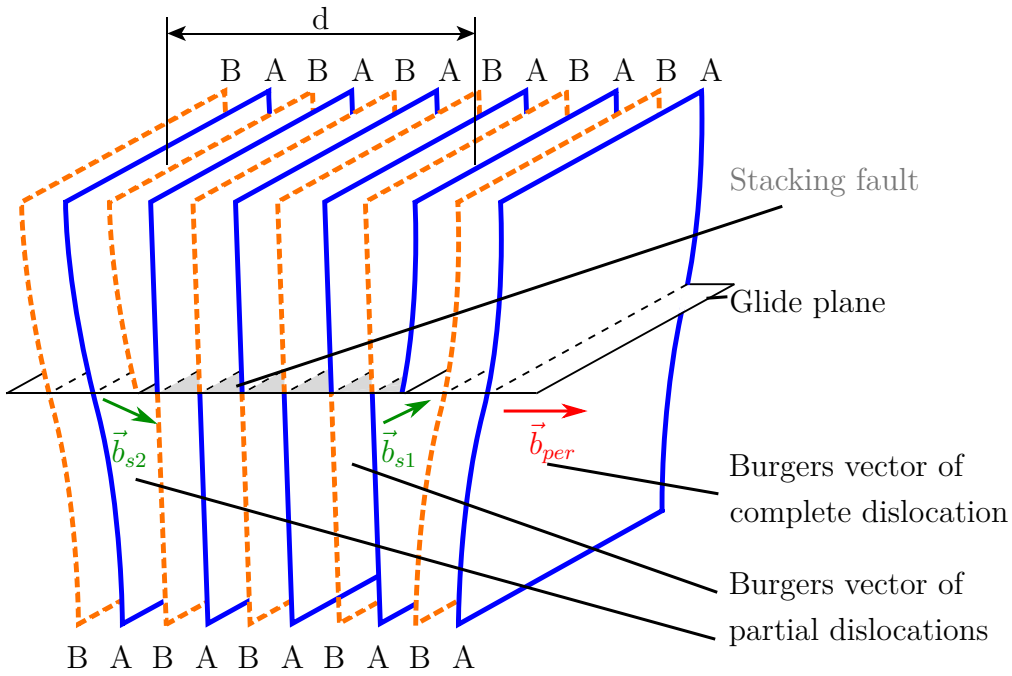

Figure 2.16: Schematic cross sectional drawing of two Shockley partials in a distance d with a stacking fault between the partial dislocations after Hull and Bacon [26].

This kind of partial dislocation, shown in Fig.2.15 is called Shockley partial, characterized by a displacement vector of the type $\vec{b} = \pm\frac{a}{6} < 112 >$, which is also not a

translation vector of the lattice. In general, dislocations characterized by Burgers vectors that are not translation vectors of the lattice are called partial dislocation and they are necessarily bordered a two dimensional defect like the stacking fault shown in Fig.2.14 or 2.16 [19]. Besides the Burgers vector, the difference between Frank and Shockley partials is the possibility to glide. Shockley partials are able to glide on the same glide plane (spread out by Burgers vector $\vec{b}$ and line vector $\vec{t}$) like the perfect dislocation where the stacking fault moves along and they are able to change their length without any issues. In contrast, the Frank partials loops are bounded and can only move on their glide cylinder, whereby additional length changing would include the absorption or emission of point defects.

2.3.4 Precipitates

Precipitates could be formed by an agglomeration of point defects at a specific temperature when the concentration of the point defects exceeds the solubility limit. According to Borghesi [8], oxygen precipitates emerge predominant from about 1000−1200 °C during the block cast process. One main source of oxygen contamination is the dissolution of the quartz crucible into the silicon melt [80]. Carbon dissolves into the liquid silicon from contamination of the feedstock, as well as from carbon monoxide from the furnace environment. Typical impurity concentrations in the solar silicon used in this work are $3 \times 10^{16} - 3 \times 10^{17}$ cm^{-3} of O_i (oxygen interstitials) and $5 \times 10^{16} - 1 \times 10^{18}$ cm^{-3} of C_s (carbon substitutionals). Additionally, " metallic impurities are always present in cast silicon material. They originate from contaminants in the feedstock and in the quartz crucible and its coating" [80]. For examples, the measured interstitial Fe_i concentration, at silicon material investigated in the next chapters, was about $1 - 10 \times 10^{14}$ cm^{-3}.

2.4 Experimental methods

In the following section, the experimental methods used will be explained. The different methods need various special sample preparations to perform the investigations correctly. These previously performed preparation steps for mc-Si samples are also described in the following. Thin-film samples exhibit some complications to prepare them for the measurements. The discussion about the complications is placed separately in the second part of chapter three, where the thin-film measurements will be described. For the initially presented scanning electron microscopy measurement methods, like CL, EBIC, EBSD and TEM, the interaction of the excitation electron beam with the sample material is essential to know. Therefore, prior to explaining the methods, the basic mechanisms about material interaction are briefly shown.

Electron beam - material interaction

If electrons are induced into material, for example through illumination with an electron beam, electrons will be scattered. Scattering processes can be divided into elastic and inelastic. Through elastic scattering from electrons at atoms it comes to reflection of high energetic electrons. These backscattered electrons (E_{bs}) can be detected through a scanning electron microscope (SEM). In dependence of the atomic number of the material, a contrast image will be observed. The inelastic scattering allows different kinds of investigation methods. Due to the electron material interaction, it comes to secondary electron emission (E_{SE}), building of electron-hole pairs (E_{eh}), cathodoluminescence, x-ray radiation E_x, Auger-electrons and thermal effects like electro acoustical effect. The energy of the impact electrons (E_0) is distributed into:

$$E_0 = E_{bs} + E_{SE} + E_{eh} + E_x + ...$$

The energy of the electron-hole pairs may be accepted:

$$E_{eh} \approx E_0 - E_{bs} \approx (1 - \gamma)E_0 = 0.9E_0 \tag{2.9}$$

This common assumption is valid under the presumption that the influence of the secondary electron emission and x-ray radiation in silicon could be neglected and the backscatter coefficient γ of the electron beam is approximately 10 % [98]. The electron-hole pair generation in silicon occurs through impact ionization. An electron in the valence band is excited into the conduction band, thus leaving a hole in the valence

band. Because the conduction and the valence band are not solid single bands but rather divided into several sub bands, the required average generation energy ε for a electron-hole pair is higher than the band gap energy E_g. For silicon, ε is estimated at $\sim 3.6\ eV$ [98]. Therefore, it is possible to calculate the number N of electron-hole pairs per primary injected electron with energy E_0 in keV.

$$N = \frac{E_{eh}}{\varepsilon} = \frac{900}{3.6} E_0 = 250 E_0 \tag{2.10}$$

The penetration depth for the primary electrons in semiconductors can be calculated. One generally accepted formula was established by Kanaya and Okayama in 1972 [30].

$$R_e = \left(\frac{0,0276 A}{\rho Z^{0,889}} \right) E_0^{1,67} [\mu m]$$

R_e presents the penetration depth, E_0 electron acceleration voltage in keV, A atom weight in $\frac{g}{mol}$, ρ density in $\frac{g}{cm^3}$ and Z atom number. The exemplary penetration depth after Kanaya and Okayama of Si, Ge, GaN and GaAs are shown in Figure 2.17 in dependence of the beam energy. Besides the calculation after the maximum range of

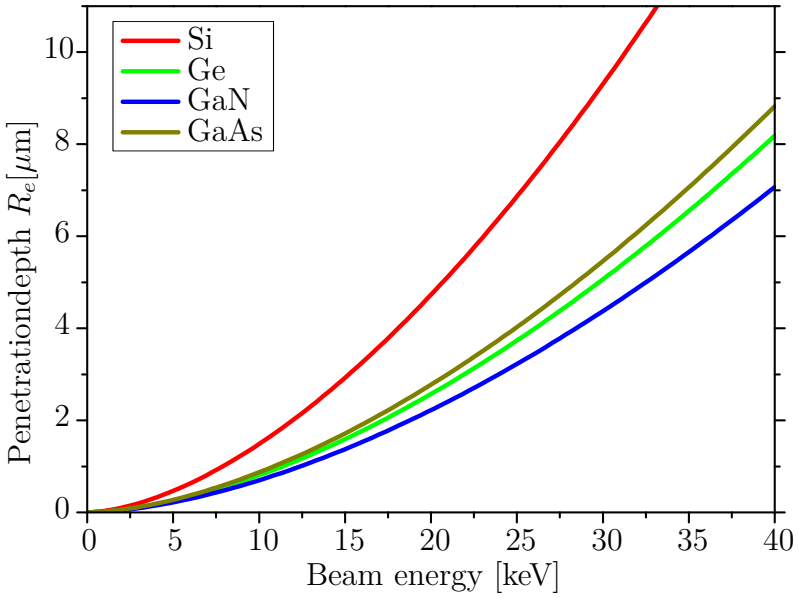

Figure 2.17: Electron penetration depth R_e in different semiconductor materials at increasing electron acceleration voltage E_0 calculated after Kanaya-Okayama.

Kanaya and Okayama, there is also the possibility to calculate the penetration depth with the universal curve of Everhart and Hoff or with the Gruen range [48]. It is

generally accepted to use any of these formulas, although it is necessary to be aware of which one is used during the data analysis.

The penetration depth defines the generation volume of electron-hole pairs. The number of generated pairs could be described by an normalized analytical empirical depth-dose function $\lambda(Z)$ given by Everhardt and Hoff [18] valid for $0 \leq \frac{z}{R_e} \leq 1.1$:

$$\lambda(Z) = \lambda\left(\frac{z}{R_e}\right) = 5.69\left(\frac{z}{R_e}\right)^3 - 12.4\left(\frac{z}{R_e}\right)^2 + 6.21\left(\frac{z}{R_e}\right) + 0.6$$

where z is the depth under the surface. With equations (2.9) and (2.10), the electron beam current I_B and the minority carrier charge q the depth-dose function can be quoted as

$$N(z) = \frac{I_B E_B (1-\gamma)}{q\varepsilon R_e}\lambda\left(\frac{z}{R_e}\right) = \frac{N}{R_e}\lambda(Z)$$

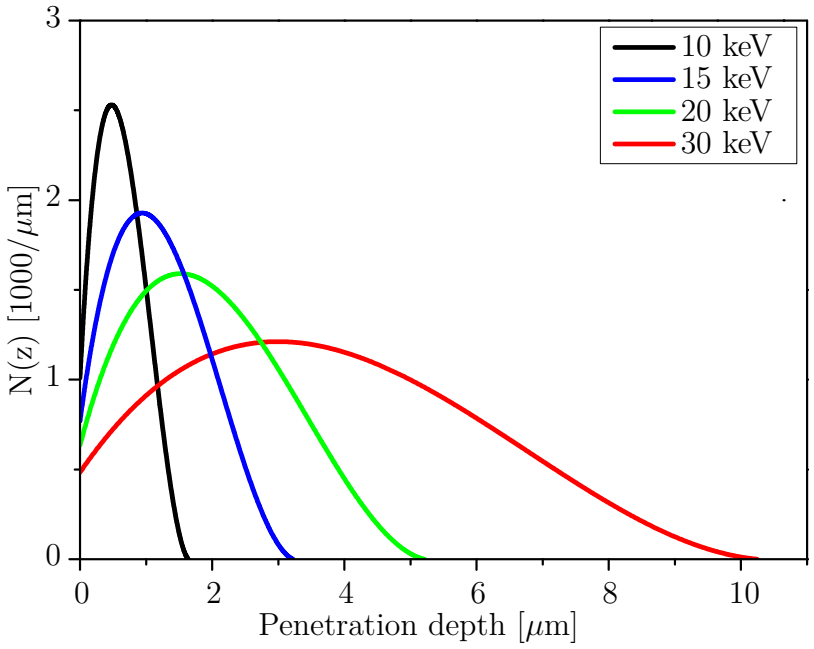

Figure 2.18: Number of electron-hole pairs formed per micrometer for different electron beam energies by a single energetic electron in silicon. Depth-dose curves are of the form determined by Everhardt and Hoff [18] with the penetration depth after Kanaya-Okayama [30].

2.4.1 Cathodoluminescence - CL

Cathodoluminescence is the emission of light as a result of electron bombardment. It offers a contactless, nondestructive measurement method with high spatial resolution for the characterization of semiconductors. One important advantage compared with optical methods is the possibility to achieve depth resolved information by changing the energy of the electron beam. The name cathodoluminescence itself comes from the cathode as electron source.

First time usage for characterization emerged around 1880 by William Crookes, who used the method at lead glass. Nowadays, interest arose late in the 1950s due to the development of analytical (x-ray)-electron-microscopy [69]. Initial applications were in the field of mineralogy and petrology because the CL images reveal the different components of quartz, dolomite and feldspar, as well as remaining skeleton structures of fossils. In 1960, CL applications increased due to commercially available scanning electron microscopes (SEM) and first steps in space investigations and microelectronics [69]. Today, CL can be found in almost all scientific fields.

Sample preparation: The 1×1 cm sized samples were cleaned with a Piranha solution (30% H_2O_2 and 70% H_2SO_4) and dipped into HF-solution to prevent the formation of an oxygen layer at the surface. Thus, surface recombination can be reduced.

Signal

As already mentioned in section 2.4.1, the luminescence results from radiative transitions in material excited by an electron beam. Due to the absence of a general rule like Moseley's law in x-ray microanalysis, which could serve to identify bands or lines in the CL spectrum, it is difficult to distinguish between transitions that involve impurities or variety other defects [99]. Non-radiative transitions cannot be described by CL measurements. Radiative transitions are influenced by temperature. Therefore, cooling of the sample (i.e. with liquid nitrogen or liquid helium) could result in sharper lines in the observed spectra, which possibly enables the identification of transitions between defined energy levels [99]. Due to the excitation by an electron beam, the most radiative transitions will be excited at once [99]. The electron probe size, the size of the generation volume of electron-hole pairs and the minority carrier lifetimes are responsible for the resolution of the cathodoluminescence [99]. According to [83], the spatial resolution of CL is in the micrometer-range and at areas with strong recombination

activity a spatial resolution of just ≈ 1 μm is feasible. Obtained spectra are dependent on temperature, beam energy, beam current, sample bias and electrical fields. The investigation of the influence at the silicon BB luminescence is commonly well described in literature, but for the defect luminescence there remains room for improvement.

Setup

The CL measurements were conducted in a Zeiss EVO 40 SEM equipped with a Helium cooling stage working with liquid nitrogen at 80 K, as well as with liquid helium down to 10 K. Additionally, the SEM was mounted with a Gatan MonoCL3 system and a Hamamatsu InGaAs photomultiplier detector with a range from 250 nm up to 1700 nm. The schematic setup is shown in Fig.2.19. The electron beam originates

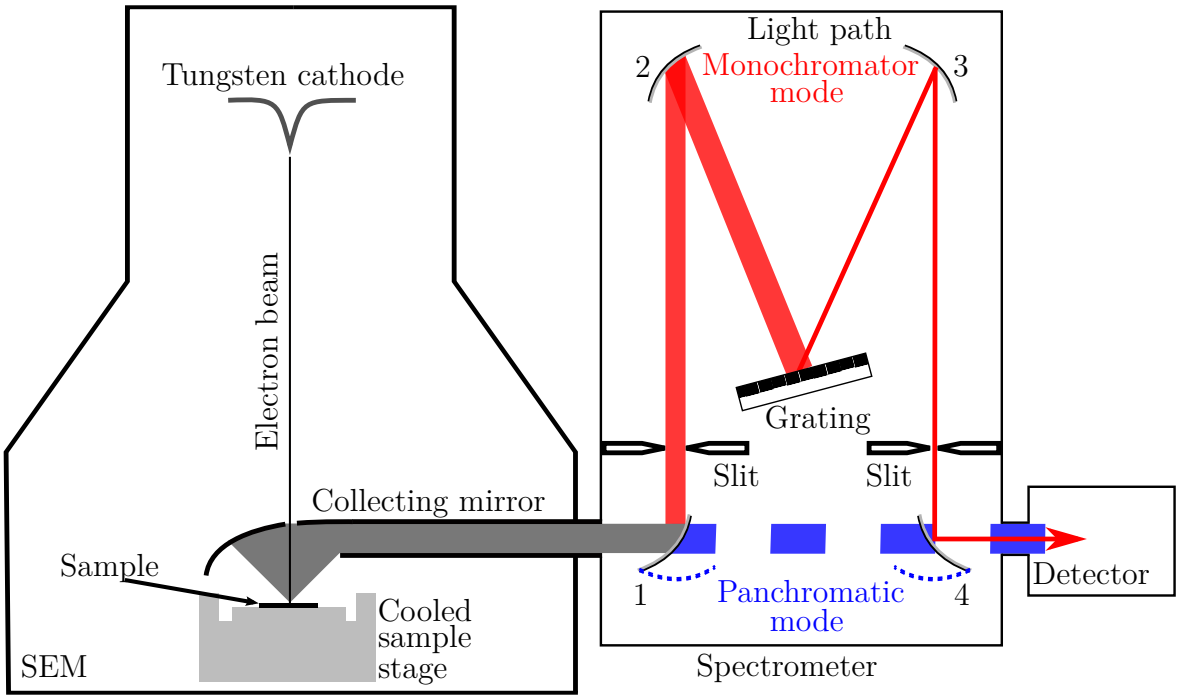

Figure 2.19: Schematic setup of the used CL measuring system, including simplified light path for monochromatic (red), using mirrors 1-4, and panchromatic (blue), with rotated mirrors, spectrometer settings.

from a tungsten cathode and is focused on the sample through a hole in the parabolic collecting mirror. This mirror, placed above the sample, collects the generated luminescence and led it to the spectrometer (MonoCL3 system). In the case of panchromatic (all wavelength) measurements, the mirrors 1 and 4 have to be rotated to lead all collected light to the photomultiplier tube (detector). If a mapping of just one selected

wavelength is planned, the monochromator mode has to be used. The slits are used to control how much light will be induced in the monochromator: wide slits give a higher intensity, whereas narrow slits give a better resolution. After passing the spectrometer, the signal is recorded by the photomultiplier. The detector allows acquiring a spectrum of the chosen sample position (Fig.2.20 *c*) or performing a spatial mapping of a selected area. The mapping procedure is possible in monochromatic mode (Fig.2.20 *a* and *b*), to record just one selected wavelength, or in panchromatic mode recording all emitted wavelengths. Another detection system, compared to the sequential one

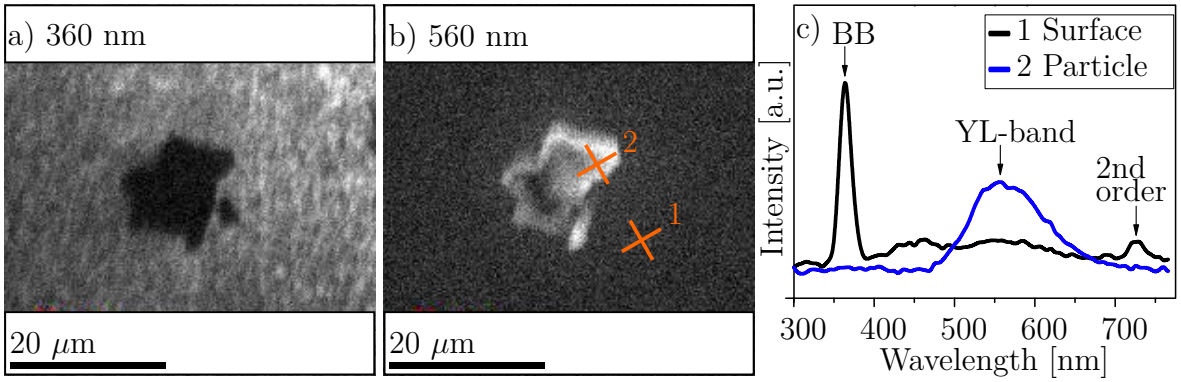

Figure 2.20: Monochromatic CL image at *a* 360 nm, *b* 560 nm of GaN grown at Al_2O_3 substrate and *c* the corresponding spectra from the surface *1* and from the particle *2* after Krause [43].

used in Cottbus, is mounted in the Electron- and Ion Microscopic Facility of Interdisciplinary Resource Center for Nanotechnology of Saint Petersburg State University (IRC-NT-Lab). It was also possible to use it for this work during a short work stay at their laboratory. They use a parallel CL detector with a charge-coupled device (CCD) camera, which allows low noise spectral measurements within few seconds during the sample scanning process. Therefore, it is possible to acquire all spectra from every single point of the scanned area very quickly. The spectral ranged from this detector is 900 up to 2200 nm. Furthermore, this parallel detector with 1064 channels allows spectral measurements with a spectral bandwidth of about 260 nm during the sample scanning process. However, it is not possible to record panchromatic or even monochromatic images of the scanned surface area due to the discharge time of the CCD detector. The only way round is a mapping procedure, whereby a program measures the spectral distribution at each point of the selected area, calculates the average intensity value for a small part and creates a map of the intensity distribution. Even this detour takes much time related to the studied area and the intensity of the luminescence.

2.4.2 Electron beam induced current measurements - EBIC

EBIC is used to investigate recombination active defects, lifetime inhomogeneities and also doping variations. Thereby, it is not important if electron-hole pairs recombine radiative or non-radiative at these defects. Through the variable beam energy, it is also possible to collect information about defect depth distribution, diffusion length, as well as the surface recombination. Furthermore, the high spatial resolution enables the investigation of selected single defects as well as mapping the recombination activity over a selected sample area. Due to nondestructive measurements, this method of analysis is widely used in photovoltaic and microelectronic.

Sample preparation: To perform EBIC measurements, a diode like sample structure containing a pn or Schottky junction is necessary. Therefore Schottky diodes were prepared. EBIC samples, 1×1 cm, were slightly isotropic etched with HNA - solution (HF, HNO_3 and CH_3COOH) to prevent influences from surface damage caused by the wafer sawing step, cleaned in Piranha solution to build an oxide layer to improve the Schottky barrier, and rinsed with deionized water. Finally the front Schottky contact was prepared by deposing a 10 nm aluminum layer over the oxide interlayer. The ohmic contact was formed by rubbing InGa alloy on the sample back surface. This kind of back contact exhibit also a good conductivity at low temperature like 80 K or even at 15 K.

The IV-investigations were conducted at samples with Al deposited dots without an oxygen layer to prepare ohmic contacts at the p-type Si samples. To compare different regions of the sample, some of the dots are located at regions with a high concentration of twin boundaries and others were placed at areas with plain grains without boundaries. In addition, the samples were tempered for 20 min at 400 °C to increase the conductivity of the ohmic contacts by slightly diffusing Al into the sample at the contact spots.

Signal

Electric current is generated similar to a solar cell. While sun light is necessary at solar cells, for EBIC an electron beam is used. Measurements are performed at short-circuit conditions (Fig.2.21).

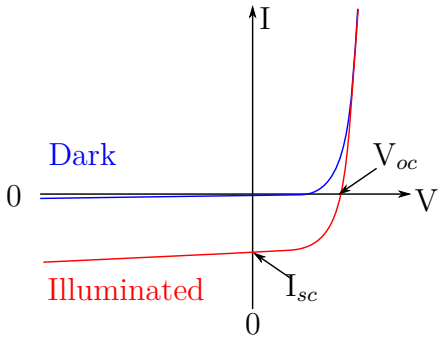

Figure 2.21: Characteristic of a solar cell (blue) without, (red) with illumination and marked measurement conditions for EBIC I_{sc} and EBIV V_{oc}.

High energetic electrons excite the generation of electron-hole pairs. The electric field due to the depletion region (SCR) of a short-circuit Schottky junction separates these pairs and induces a current. The signal emergence is simplified shown in Fig.2.22.

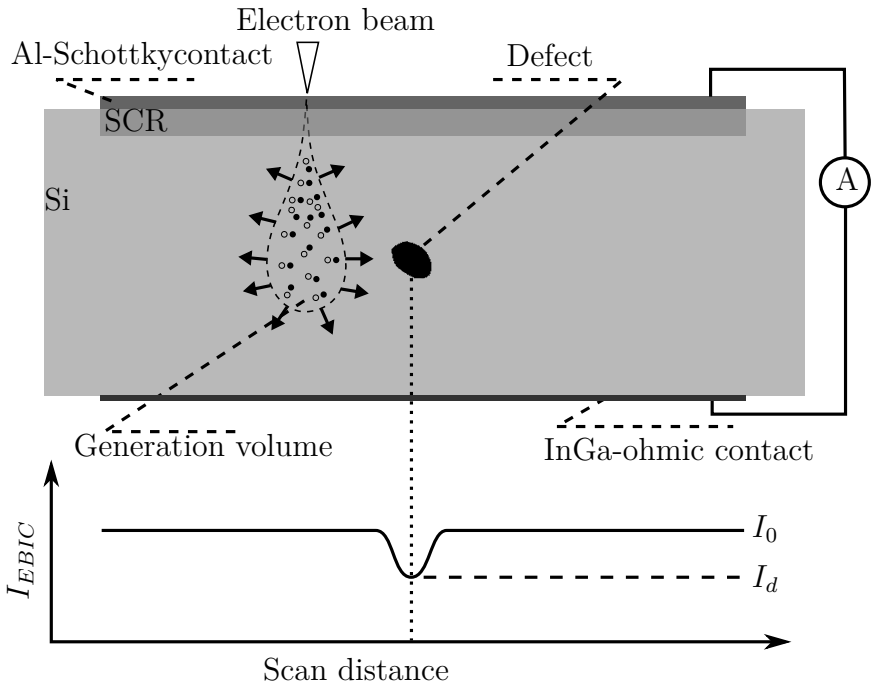

Figure 2.22: EBIC measurement setup and signal build.

At the achieved grayscale-map (Fig.2.23), areas with no defects will show up bright, high collected current (I_{EBIC}), while defect rich areas appear dark, decreased I_{EBIC}. The EBIC measurements are strongly temperature dependent. Fig.2.23 shows the EBIC micrograph of a sample overview at 300 K compared to 90 K. Through cooling it is possible to reveal recombination active dislocations even in the grains which possibly appear bright at 300 K.

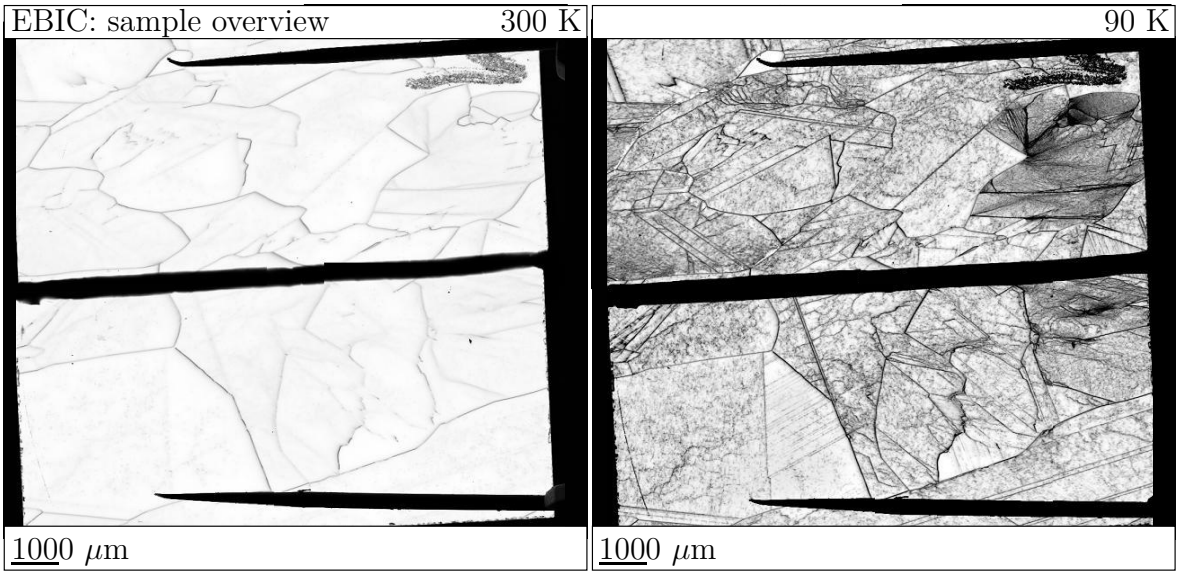

Figure 2.23: EBIC micrograph: sample overview merged from 6 single images at 300 K compared to 90 K with 100 pA and 30 keV.

The calculable collection efficiency η can be used for the characterization of material properties. With the measured EBIC current I_{EBIC} and the maximal possible collected current $250E_0I_B$, according to equation 2.10 the collection efficiency is:

$$\eta = \frac{I_{EBIC}}{250E_0I_B} \tag{2.11}$$

The energy dependent collection efficiency is also a function of the thickness of the metal Schottky contact, the depletion layer width, the surface recombination velocity and the minority diffusion length [98]. The recombination activity is characterized by the EBIC contrast c with the EBIC current at the defect site I_d and the current I_0 far away from the defect in a defect-free region:

$$c = \frac{I_0 - I_d}{I_0}$$

The contrast is dependent of the defect geometry, beam conditions as well as the substrate properties [35]. Kittler et al. [38] reported a tentative classification of defects related to their contrast behavior. The two different groups of temperature and beam current related contrast are presented in Fig.2.24. The first group could attributed to defect charging (deep states) and the second one to shallow defect centers. Deep defect levels, which are located deep in the band gap, near the Fermi energy (section 2.1.1), become already recombination active at room temperature, while shallow defect levels near the band edge, far away from the Fermi energy, show a recombination contrast after cooling, at a certain lower temperature.

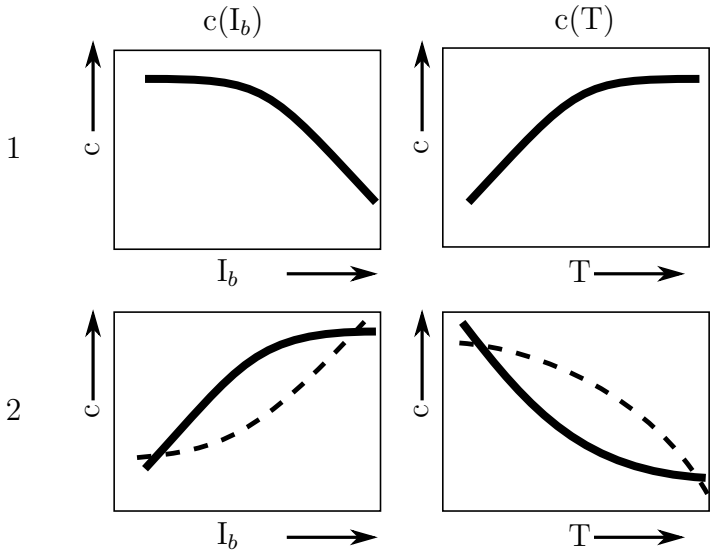

Figure 2.24: Illustration of the two different groups of contrast behavior according to [38].

A diffusion equation to explain the formation of EBIC contrast was solved by Donolato [14], who proposed that the contrast can be defined as a product of recombination strength Γ and a correction factor f:

$$c = \Gamma f$$
$$\Gamma = \frac{1}{D}\left[\frac{1}{\tau_d} - \frac{1}{\tau_0}\right] = \frac{1}{L_d^2} - \frac{1}{L_0^2}$$

with the diffusion coefficient of the minority carrier D, the minority carrier lifetime at the defect site τ_d as well as at the defect free site τ_0 and the corresponding diffusion length L_d respectively L_0. In the common case, $L_d \ll L_0$ and it is possible to simplified Γ to $\Gamma \approx \frac{1}{L_d^2}$. These recombination strength is independent of beam conditions, defect geometry and sample properties. The correction factor f involves all dependences and

can calculated using Donolato's model. Like at CL, the spatial resolution is mainly limited by the electron beam settings (energy and current), the beam-sample interaction, and the material properties (i.e. diffusion length of the minority carriers). A spatial resolution below 100 nm is achievable.

Setup

EBIC measurements were also performed with the same Zeiss EVO 40 SEM as the CL investigations. Scanning with the electron beam over the sample generates EBIC current. This EBIC signal was led to a current pre-amplifier and subsequently digitalized to a PC with Gatan Software for evaluation. The beam current was measured using a Faraday cup at the sample holder. Temperature data are gathered using a diode placed inside the sample holder close to the sample backside. Afterwards evaluation was performed using Gwyddion Software for gathering profiles from recorded EBIC images, before exporting these raw data sets for further analysis in Origin.

Besides the default EBIC setup shown in Fig.2.22, there is also the possibility to measure cross sectional. Thus, to examine thin-films, the advantage of considering every single layer is given. To perform this kind of measurement, a specially designed sample holder is necessary. In Fig.2.25, both kinds of sample holders used are shown. Both holders are mainly made of copper. For electric isolation, in contrast to good thermal conductivity, a thin layer of vacuum grease was placed between the two parts of the commonly used EBIC holder. This enables the placement of front and back contact at opposite sample sides without a shortcut to the sample stage. Note that this isolation is missing at the cross sectional holder setup; therefore, front and back contact have to be placed at the surface of the sample. There is no shortcut to the sample stage because the investigated thin-film samples contain a thick glass substrate at the backside.

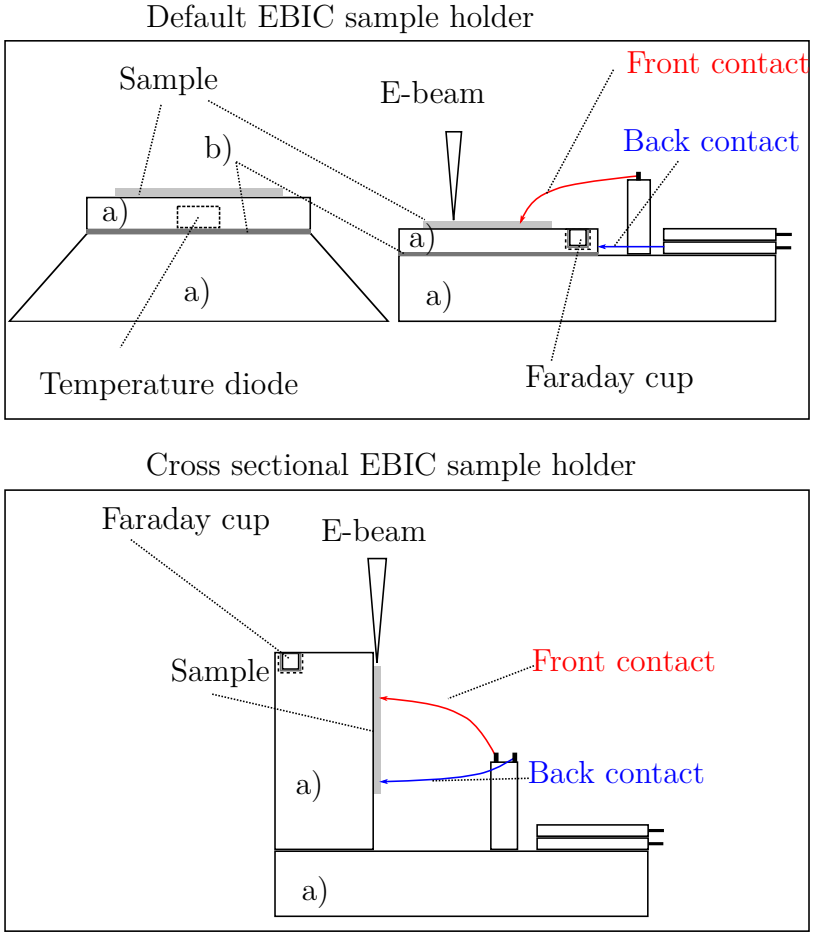

Figure 2.25: (top) Setup of the default EBIC sample holder for the common investigations made of copper a) with an electronic isolating layer b) between the bottom and top part of the holder. (bottom) Setup of the holder designed for cross sectional EBIC measurements with front and back contact placed at the surface of the sample.

Electron beam induced voltage - EBIV

As well as EBIC measurements at short-circuit current (I_{sc} in Fig.2.21), it is also possible to perform EBIV measurements at open-circuit voltage conditions (V_{oc}). For this kind of investigation, another kind of amplifier with a high input impedance was used. The EBIV measurements should provide insights into local variation of the sample resistivity.

2.4.3 Electron backscattered diffraction measurements - EBSD

The crystallographic orientation of a sample can be measured with the Electron backscatter diffraction (EBSD) method. This microstructural crystallographic technique can be performed with a SEM equipped with an EBSD detector.

The electron beam of the SEM strikes the tilted sample, which is mounted at a rotatable and tiltable xyz-stage. The impinging electrons will be scattered inelastic in all directions. Therefore, electrons will be scattered at all atomic planes and might be interfere constructively if the Bragg's law is fulfilled. A pattern from diffracted electrons will be formed on a fluorescent screen, reflecting the crystal structure and orientation of the investigated region. This kind of diffraction image is called Kikuchi-Pattern and is shown in Fig.2.26.

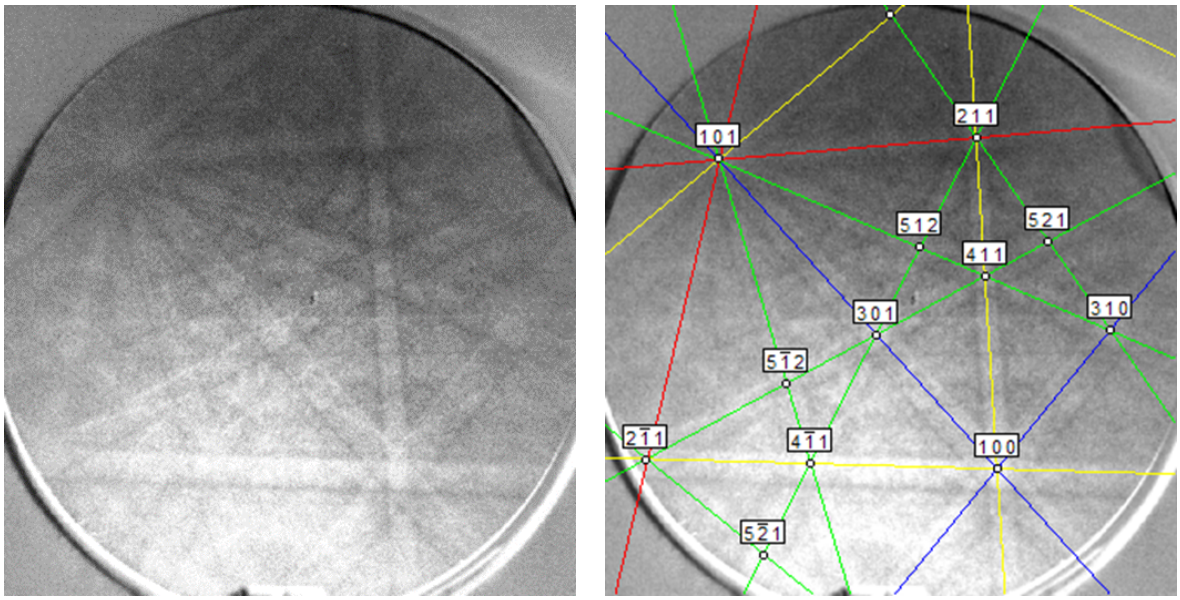

Figure 2.26: At the left Kikuchi-Pattern of mc-Si, at the right with identified reflection planes.

The computational evaluation of these patterns offers the possibility to identify the local crystal structure and orientation, as shown in Fig.2.27. In image *a)*, the inverse polfigure (IPF) is shown, which provides the necessary information to identify the grain orientations in image *b)* according to their color. Image *c)* is a gray-scaled image quality (IQ) map reflecting the sample surface. At this IQ-map, the different grain boundaries (GBs) are color marked, different colors imply a different GB orientation. The marked GBs are identified to be red: $\Sigma 3$, green: $\Sigma 9$, and blue: $\Sigma 27a$. The light blue GB with a rotation angel of about $6 - 8°$ could not be counted to a CSL Sigma value.

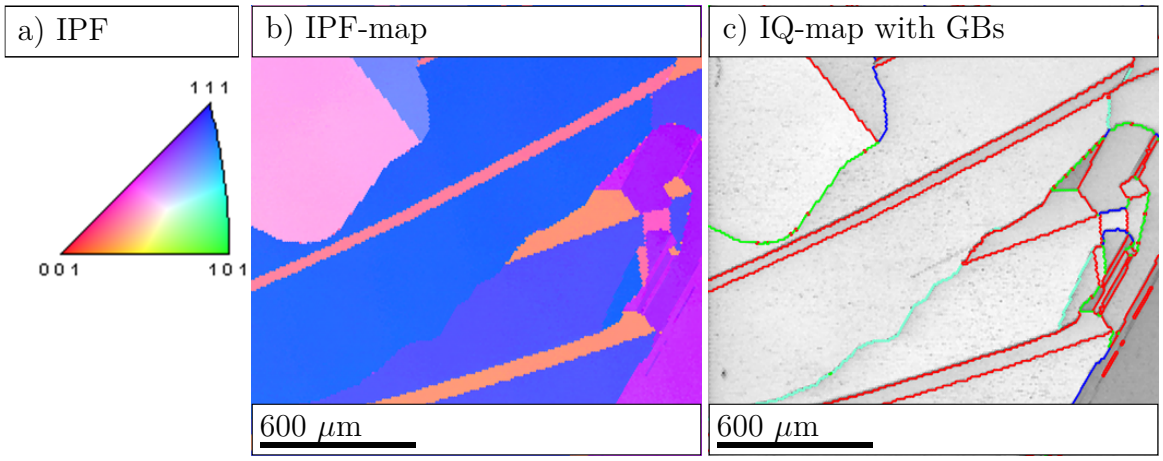

Figure 2.27: *a)* Inverse polfigure (IPF), *b)* IPF-map of an investigated sample from chapter 5, *c)* Image Quality (IQ) map of the same sample area with marked grains.

For the measurements, a Zeiss MA 25 SEM equipped with a TSL-camera was used. The measurements and data analysis were conducted with EDAX OIM software by H.-M. Krause.

Sample preparation: To improve the EBSD measurement results the sample pieces were mechanically polished, cleaned in Piranha solution and rinsed with deionized water prior to conducting the measurements, which should provide the possibility to record good diffraction pattern.

2.4.4 Transmission electron microscopy - TEM

An electron beam is transmitted through a thin sample while interacting with it (scattering). According to Krumeich [46] several possible TEM methods could be used to collect different information from the investigated sample. Bright- and dark-field TEM (BF/DF-TEM) enables the detection of crystalline areas and the localization of defects and grain boundaries. Phase analysis are possible and the particle size can be estimated. Using high resolution transmission electron microscopy (HRTEM) provides the direct visualization of structures and defects. Energy filtered transmission electron microscopy (EFTEM) and electron energy loss spectroscopy (EELS) is used to obtain elementally sensitive images. With electron diffraction (ED) lattice parameters, the crystal symmetry as well as the crystal orientation can be determined. If an additional system to raster the beam across the sample with appropriate detectors is used, the modified TEM is called scanning transmission electron microscope (STEM). One used STEM method in this work is the annular dark-field imaging (ADF), whereby scattered electrons are collected with an ADF detector. How the application for signal detection may could be look is shown in Fig.2.28.

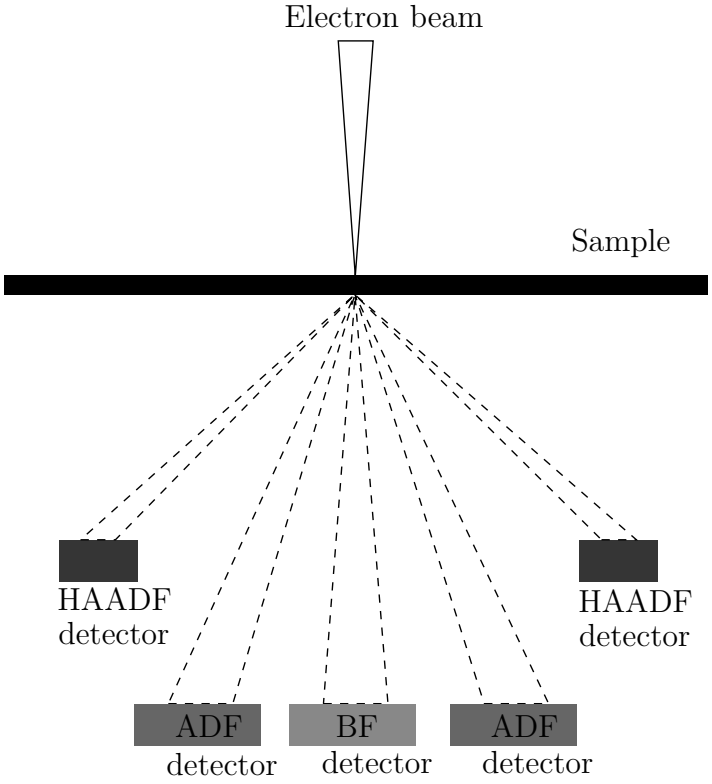

Figure 2.28: Schematic drawing of possible STEM detector arrangement after Krumeich [46].

Similar to the previously mentioned BF-TEM method, the detector for the BF-STEM method is placed in a way to detect the intensity of the direct beam from a point of the specimen. The ADF detector, used for this work is a circular plate with a hole in the center, where the BF detector is located. The ADF detector should collect scattered electrons, working similarly to the DF-TEM method. The formed contrast mainly results from diffracted electrons in crystalline areas but is superimposed by incoherent Rutherford scattering. For the high-angel annular dark field (HAADF) measurements, there is also a detector disk with a hole in the center, although the disk and also the hole diameter are much larger than that of the ADF detector. Therefore, electrons scattered to higher angles will be detected. Almost only incoherent Rutherford scattering contributes to the build images and thereby the Z contrast, according to the atomic weight, could be achieved [46]. An example image for a HAADF TEM is displayed in Fig.2.29 showing two twin boundaries in the mc-Si samples investigated in chapter 4.

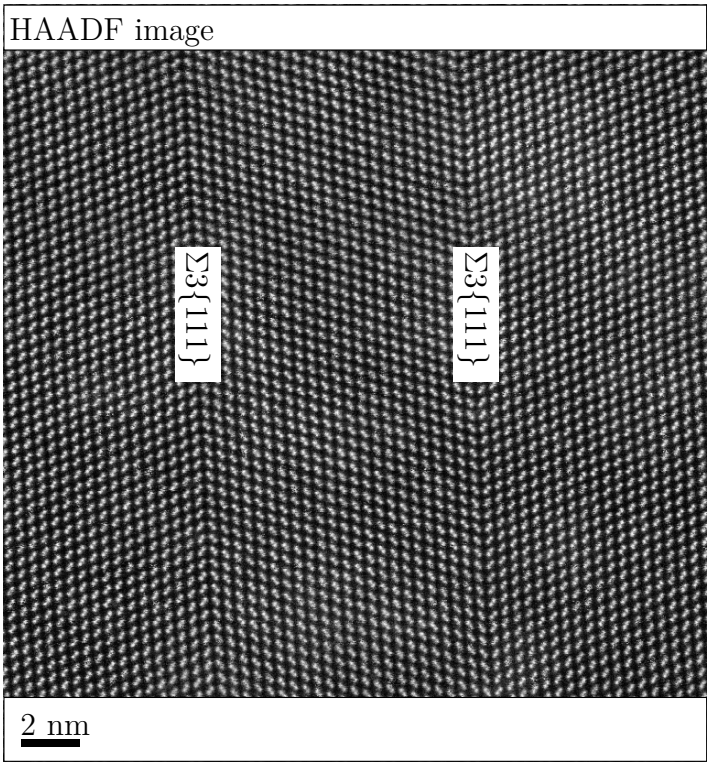

Figure 2.29: HAADF TEM image of two twin boundaries in mc-Si.

The necessary investigations for this work at a STEM were performed and analyzed by Dr. A. Hähnel at the MPI of Microstructure Physics Halle.

Sample preparation: For the TEM measurements, electrons have to transmit through the sample. Therefore thin samples ($\sim$ 100 nm) were prepared using focused ion beam techniques (FIB). This preparation step was performed by H. Blumtritt at MPI Halle.

2.4.5 Photoluminescence - PL

Photoluminescence (PL) is the luminescence excited by light (i.e. laser beam).

Signal

The signal generation is mainly the same as CL. Instead of electrons, photons excite electrons to higher energetic levels with following relaxation through radiative and non-radiative recombination. Similar to CL, only the radiative recombinations are detectable. The achieved information through PL differs from CL measurements. Due to Beer's law of absorption, the penetration depth of the laser beam is specific to the wavelength and the investigated material. It is only possible to generate luminescence with a lower energy than the excitation energy. According to Klossek [41], the laser spot size and the carrier diffusion length of the sample material limit the spatial resolution in general. By reducing the laser step sizes, the excess carrier concentration in the center of the Gaussian laser beam profile will be increased, which would reduce the resolution under the spot size limit. However, a rough estimation reveals a spatial resolution of about ≈ 100 μm.

Setup

The PL setup (Fig.2.30) includes a semiconductor laser working at 532 nm wavelength. The power can be varied in 0.01 W steps from 100 mW up to 2 W. A prism led the light through a heat protection glass (F1) which prevents longer wavelength from entering the detection system. The chopper after the glass modulated the laser light for the lock-in signal detection. The parabolic mirror focused the laser beam to a 100 μm spot size on the sample and also collected the emitted light and led it to the spectrometer. Before the entrance slit to the spectrometer, equipped with a liquid nitrogen cooled Ge detector, a 830 nm long pass filter (F2) is placed, which blocks the light from the excitation laser. Arguriov [2] provides a detailed description of the PL measurement setup and method. The PL measurements were performed by D. Mankovics.

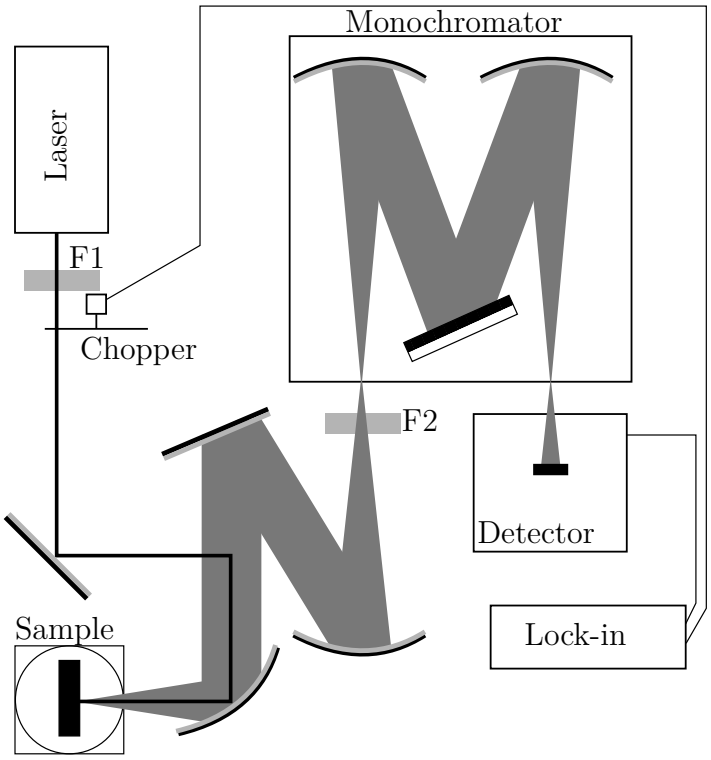

Figure 2.30: Schematic PL measurement setup; F1 prism and heat protection glass, F2 long pass filter.

2.4.6 Reverse-biased electroluminescence - ReBEL

Electroluminescence imaging under forward (EL) and reverse bias (ReBEL) can be used to correlate defect distribution and breakdown sites in solar cells [40]. An advantage of using this technique is the possibility to investigate entire solar cells without cutting them into pieces like for CL or PL measurements.

Signal

For EL, the sample will be excited by electrical current through applied forward bias, which leads to the emission of luminescence. Like at PL and CL, BB and DRL could also be observed. If applying reverse bias, at a certain bias value (breakdown voltage) the junction barrier will break down and the current could flow in the other direction, exciting luminescence at these spots. According to Mankovics, Krause et al. [58], three types of breakdown appearing in different reverse bias ranges have been described so far. “Between −4 and −9 V there is early breakdown (type 1), which is induced by aluminum contamination at the wafer surface. Between −9 and −13 V defect-

induced breakdown (type 2) dominates. This breakdown site is attributed to metal-containing precipitates lying within recombination active grain boundaries. Beyond −13 V avalanche breakdown (type 3) can be found. It is supposed that this breakdown type occurs at etch pits produced during the cell process [9]" [58].

Setup

Mankovics, Krause et al. [58] describe the setup in the following way: "An InGaAs camera (Goodrich SUI), with 640 × 512 pixel resolution on 25 mm pitch was used to detect the electroluminescence signal. The camera has uniform response to light in the spectral range from 900 to 1700 nm. The operation temperature of the detection diode matrix is maintained by a Peltier element. Electroluminescence images were taken at room temperature. To detect the band-to-band luminescence and the defect-related luminescence under forward bias several filters were used to block unwanted radiation. For detection of the reverse bias luminescence no filter was applied [78]. For microscopic electroluminescence images we equipped an optical microscope with the InGaAs camera. The achievable resolution was about 1.5 mm. Spectra of the reverse bias electroluminescence (ReBEL) were measured by a spectrometer equipped with a 300 L/mm grating and an InGaAs CCD detector operating at −70 °C."

3 Defects in solar silicon - selected case studies

The most produced solar cells are made of multi or monocrystalline silicon wafers. The well-established methods, previously described in section 2.4, are used to investigate these commonly used materials to reduce the existing wide gaps in knowledge about the defect mechanism. There is a need to know how these defects affect the collection efficiency of the solar cells in detail. In recent years, the research concerning newer thin-film PV has been increasing. The thin-film technology could possibly enable the reduction of the electricity price by reducing fabrication costs and the need of material [42; 21; 1]. For this reason, investigations at thin-film samples gained interest with the aim to explain and improve the understanding of occurred defects. In the following, there will be an overview of frequently observed defects in mc-Si. Because it is also mostly possible to apply the described methods at thin-films, the acquired insights into transferability, containing sample preparations as well as special measurement restrictions, are presented after the mc-Si results.

3.1 Multicrystalline silicon - mc-Si

The common solar cells are produced out of block cast solar silicon. Block cast means silicon is melt in large crucibles and slowly cooled, forming a large silicon block, containing many close-knit crystallites. A principal furnace design is shown in Fig.3.1. Due to this production process, silicon crystallizes while forming many grains. The ingot growing process, which includes the furnace design, the crucible type and coating, the used silicon source, the gas flow, the possibly used magnetic fields as well as the thermal heating and cooling velocity influence the quality of the resulting silicon material. Therefore, plenty of investigations have to be conducted to determine an ideal process plan to produce as good as possible solar silicon material. For this reason, detailed research in the field of defect analysis is necessary. Some of the defects that occur during investigations at mc-Si are presented in the following.

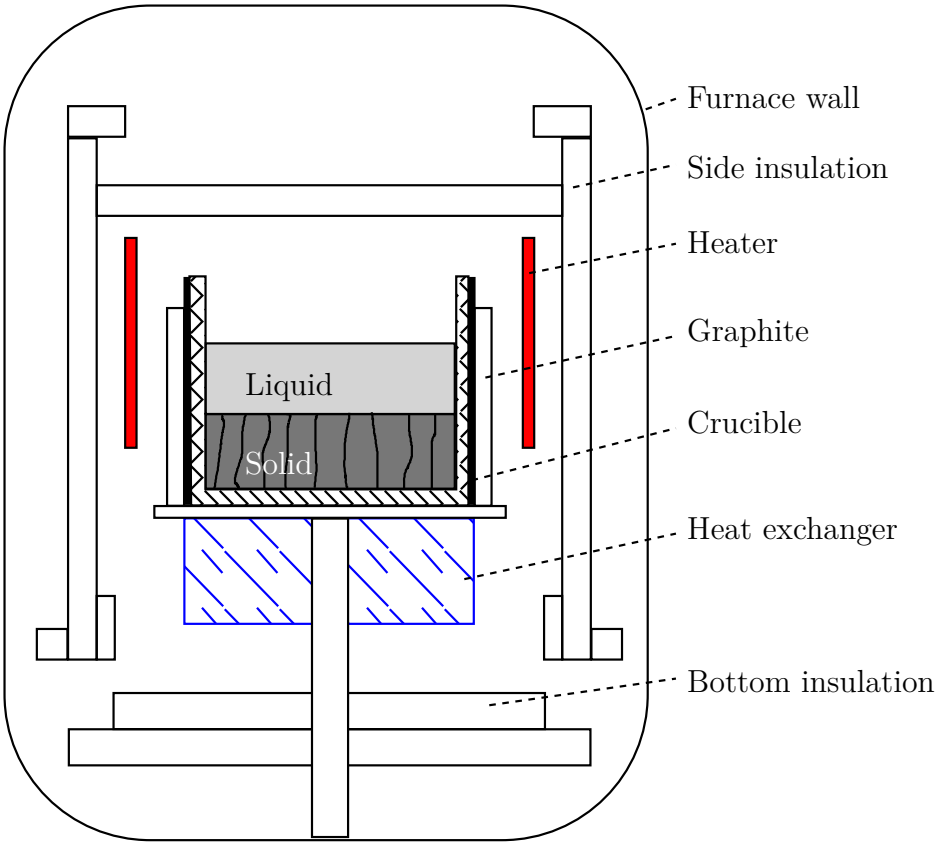

Figure 3.1: Furnace structure from a directional solidification system for mc-Si after [24].

Radiative defect features

Cathodoluminescence measurements are commonly used to investigate defect radiation with a high spatial resolution. An overview of some of the observable defect luminescences at 80 K temperature is shown in Fig.3.2. The first three images are taken with panchromatic measurement adjustment to visualize all transmitted radiative luminescence at once and localize possible interesting measurement points for further detailed investigation. Subsequently, spectral information were acquired from the marked positions, with the different spectral characteristics presented in Fig.3.3. The observed luminescence could be analyzed and associated with already known defect types.

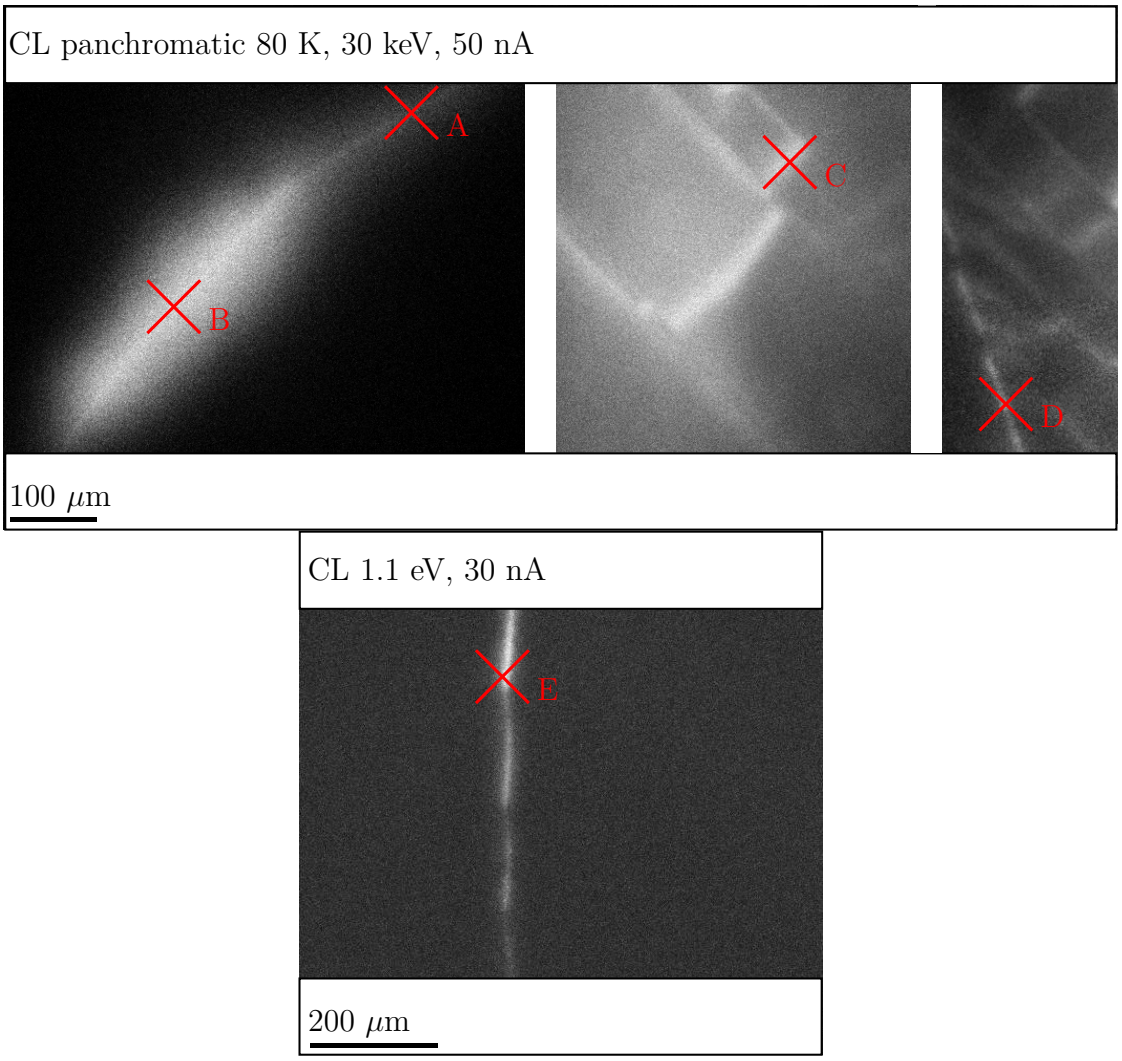

Figure 3.2: CL observations with marked measurement points at 80 K, 30 keV panchromatic at 50 nA and at 1.1 eV with 30 nA.

At point *A* the D1-D4 luminescence which is described before in section 2.2.1 can be found all at once and additional the BB radiation is noticeable. A very wide luminescence peak with a sharp D1 feature is revealed at point *B*. "The broad feature around 0.87 eV, however, can have different nature and according to Pizzini et al. [74] it could be caused either by not dissociated dislocations formed below the plasticity point of silicon, or it could be a result of an inhomogeneous broadening of the [D2, CK] transition due to locally unbalanced residual stresses and electrical fields" [45]. Furthermore, Tajima et al. [94] observed a similar broad defect luminescence at the spectral position of D2 but without dominating underlying D1 luminescence at Czochralski (Cz)-grown Si. The broad feature was referred as D_a and should be correlated with the D1-D4 lines. The observed broad luminescence in this work has its maximum intensity between 80

and 110 K and decrease below as well as above this temperatures. An almost similar behavior is also reported for the D_a luminescence. This band should be dominant between 100 and 180 K and quench above 150 K. According to these similarities, it could be possible that the broad luminescence observed at Cz-Si investigations and the occurred luminescence at mc-Si during this work might have a similar origin.

Spectrum *C* shows a typically D3/D4 doublet which might be related to glide dislocations or edge dislocations [62]. The peaks are slightly shifted which could be related to stress in the sample. Besides the shifted BB peak, the spectrum at point *D* reveals no sharp luminescence lines and is thus difficult to analyze. The elevation between $\sim$ 0.9 eV and $\sim$ 1.05 eV could be a mixture of D3/D4 possibly with a stress related influence. However, much more interesting is the high intense BB luminescence, which also occurs at measurements at point *E* in another sample.

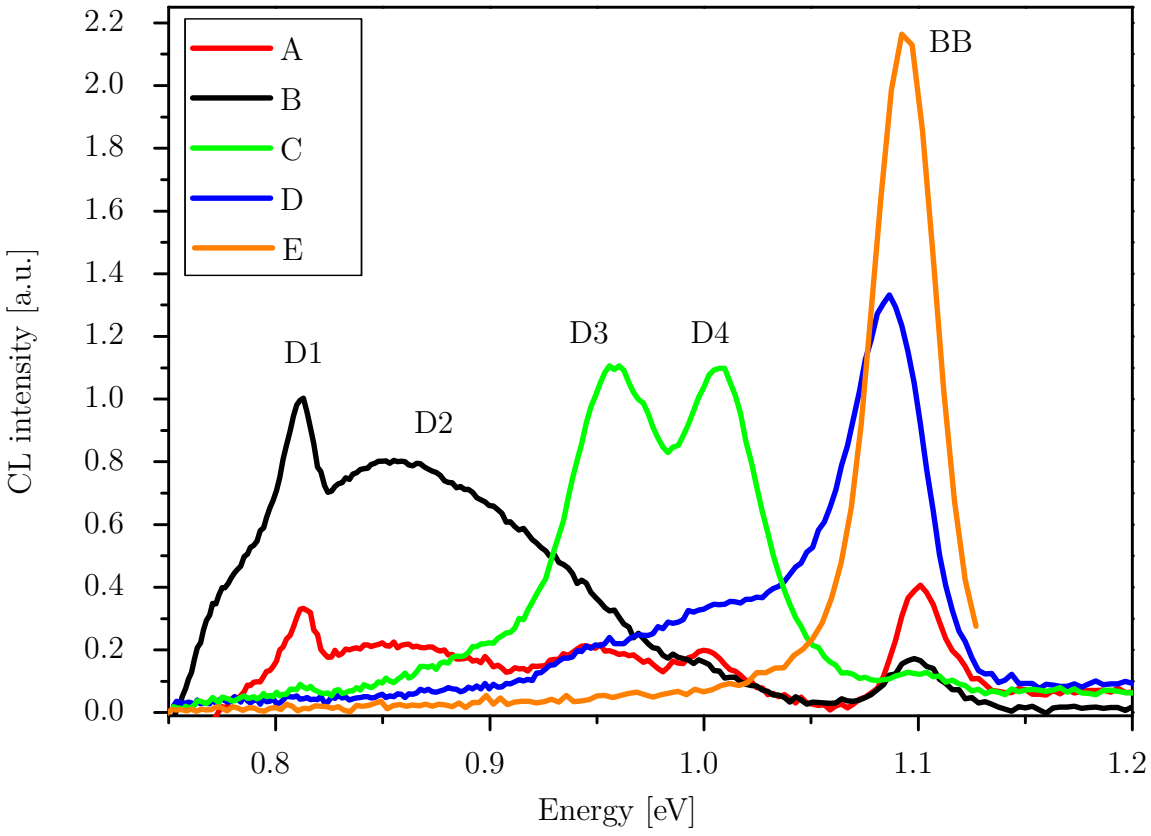

Figure 3.3: Recorded 80 K CL spectra at measurement points marked in Fig.3.2 with 30 keV and 50 nA.

In the bottom image of Fig.3.2, for the CL image acquiring process at another sample, the corresponding wavelength for the BB transition at 1.1 eV was chosen. The revealed BB luminescence along a GB is up to now inexplicable. The BB luminescence should be much more intense in less defect rich areas inside of grains than at GBs. It is generally accepted that at GB defect-related luminescence could be observe instead of BB or at least the detected BB luminescence is weaker than at spots next to the GB. Anyways during a stay at the Electron- and Ion Microscopic Facility of Interdisciplinary Resource Center for Nanotechnology of Saint Petersburg State University (IRC-NT-Lab), where a parallel CL detector system is used (section 2.4.1), several luminescence measurements were performed to estimate the applicability of such a charge-coupled device Camera (CCD Camera) in Cottbus. One of the cross-checked measurements was the occurrence of the intense BB luminescence along a GB at one of the samples. In contrast to the measurements in Cottbus, it was not possible to observe this BB luminescence feature with the CL setup in St. Petersburg. All other measurements could repeated there very well. It remains an open question why these BB feature was observed in Cottbus and not in St.Petersburg. One conceivable possibility is that the beam current in St.Petersburg was not sufficiently high. The beam current was limited to ≈ 35 nA due to the application of a field emission cathode in the used SEM there. In addition to the BB and D luminescences, it is also possible to observe luminescence features that might be related to oxygen or carbon precipitates as mentioned in section 2.2.1. In Fig.3.4 are selected CL images presented showing the occurrence of luminescence, which could be attributed to OP. This luminescence was observed under different measurement conditions and at different samples.

At the marked points in Fig.3.4, spectral information were collected and presented in Fig.3.5. The first two images *a)* and *b)* are taken at almost the same sample position at 10 K. Because image *b)* is shifted a little upwards, the marked position *A* at image *a*) is not visible at image *b)*. Nevertheless, image *b)* is taken collecting just 0.77 eV luminescence and reveals a bright luminescence spot at the marked position *B*. Image *c)* is also an energy selected record but at another sample at 80 K. Like at image *a)* and *b)* a bright luminescence at 0.77 eV can be observed at the *c)* record. Once again, at another sample with panchromatic settings, Fig.3.4 *d)* shows luminescence features at 80 K, which are spectral analyzed in Fig.3.5.

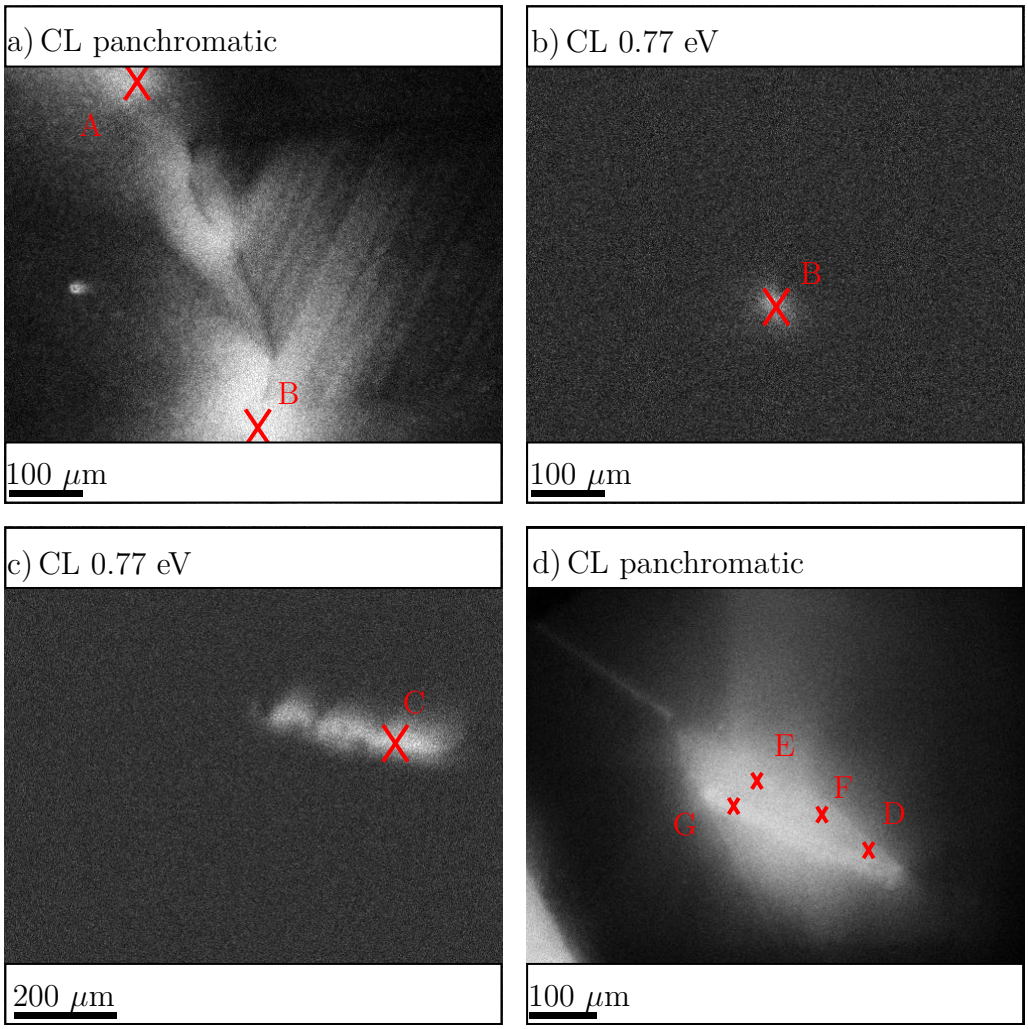

Figure 3.4: CL images from 3 different samples *a)* and *b)* are from the same sample: *a)* panchromatic and *b)* 0.77 eV energy selected at 10 K, 30 keV and 40 nA, *c)* 0.77 eV energy selected at 80 K with 30 nA, *d)* panchromatic with 28 nA at 80 K and 30 keV.

Beginning with the spectrum collected at point *A* at 10 K with 40 nA just 50% from the intensity is drawn there to show all spectra from the different measurement points at once. With no doubt, there is an additional peak with a lower energy than the neighboring D1 luminescence to recognize. A shoulder of the D1 at 0.83 eV also appears. It is possibly connected to the reported feature by Tajima et al. [27; 95], which is related to defect bands referred as D_{a1}, D_{a2} or D_b.

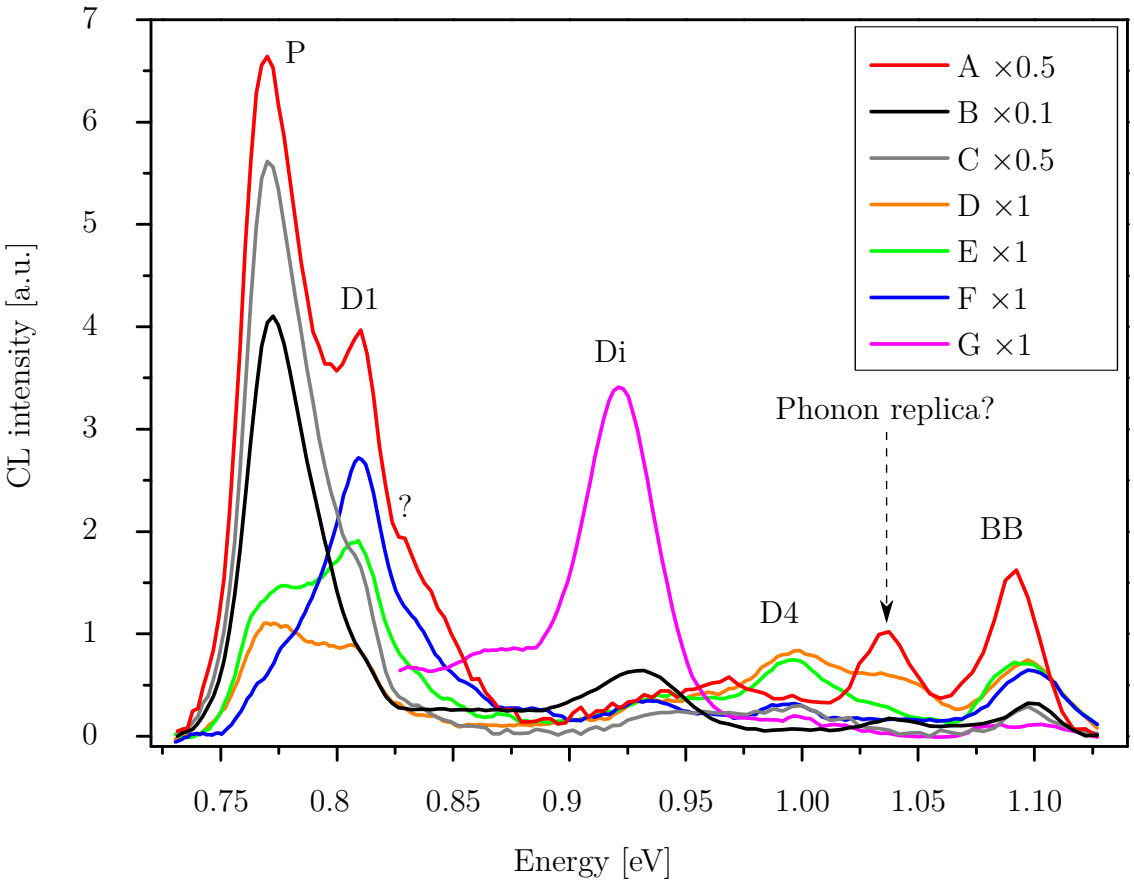

Figure 3.5: Recorded CL spectra at measurement points marked in Fig.3.4; spectra *A* and *B* are taken at 10 K, 30 keV and 40 nA, while the others are measured at 80 K, 30 keV and 30 nA.

Before the spectral position of the BB luminescence is another luminescence peak at 1.035 eV located which might be related to a phonon replica of the BB transition. The intensity of spectrum *B* was reduced by 90% and only shows a high intense luminescence at 0.77 eV, a low shoulder at the position of D1, a low intense D3 and almost no visible BB luminescence. Spectrum *C* from another sample at just 80 K have to be reduced by 50% like spectrum *A*. The spectrum also reveals a peak at 0.77 eV, as well as a low shoulder at the energetic position of D1, like spectrum *B*, and low BB luminescence. Low intense D1 luminescence with an additional almost comparable intensive peak at 0.77 eV were revealed through spectral measurements at point *D* and *E*. The observed luminescence at 0.77 eV is comparable with the reported emission at $0.78 - 0.77$ eV, 15 K by Minaev and Mudryi [65] which was extensive discussed over several years [96; 47; 92; 93; 94; 68; 31; 28; 95]. All investigations conducted suggest a close association of the luminescence at 0.78 eV (P-line) with OP [70; 65; 47; 92; 94; 31; 95] and the luminescence at 0.79 eV (C-line) to an interstitial carbon-oxygen complex [70; 47;

68; 28]. Furthermore, Kürner et al. [47] suggest an interstitial carbon atom could be also part of the P-line defect additional to an oxygen complex. The images in Fig.3.4 and the related spectra Fig.3.5 show the luminescence at 0.77 eV at 80 K as well as at 10 K. Also in the related spectra an additional D1 luminescence besides the 0.77 eV emission appears. In contrast to these findings, Tajima et al. [94] reported the observation of a luminescence at 0.77 eV (labeled D_b in his work) which occurs only at room temperature without D1 luminescence. Furthermore, at low temperature only D1 luminescence appears and according to the authors [94] the D_b band is negligible compared with the D1/D2 lines, shifts to 0.83 eV and is thus not observable. The investigations performed in this work contradict the previously reported observations. In this work it was shown that the P-line could appear next to the D1 luminescence line at 10 K.
At point *F* a broad luminescence is observed, which possibly comprise more than one single radiative transition. If there were more energetic closely neighbored transitions located at this sample spot, the luminescence peaks would superimpose each other and appear as one broad feature. The intense luminescence named Di in Fig.3.5 at spectrum *G* will be the single topic of chapter 4.

Non-radiative defect features

EBIC investigations are performed to investigate the total recombination at conducting samples. In mc-Si, the main part of the total recombination is provided non-radiative. Therefore, usually EBIC is used to investigate the non-radiative recombination in mc-Si. A significant advantage of EBIC is that already processed parts of a solar cell can be investigate without special sample preparation, whereby the electron beam excitation is comparable with the excitation by sun light.
Some of the observable defects could cause serious damage to the entire solar modules. Mankovics, Krause et al. [58] investigate and discuss such defects by PL, EL, Reverse Bias Electro Luminescence (ReBEL) as well as by EBIC. These breakdown sites especially with avalanche breakdown through reverse bias beyond −30 V (type 3) can be observed at etch pits caused during the cell process [3; 9]. Similar observations could be conducted during EBIC and SE investigations for Mankovics, Krause et al. [58]. These are shown in the following as first example what different kind of defects could be observed during EBIC investigations.

In Figure 3.6 *a)*, a ReBEL image of a part of a mc-Si solar cell made of upgrade metallurgical grade (umg) silicon is presented. The three images *b)*, *c)*, and *d)* are

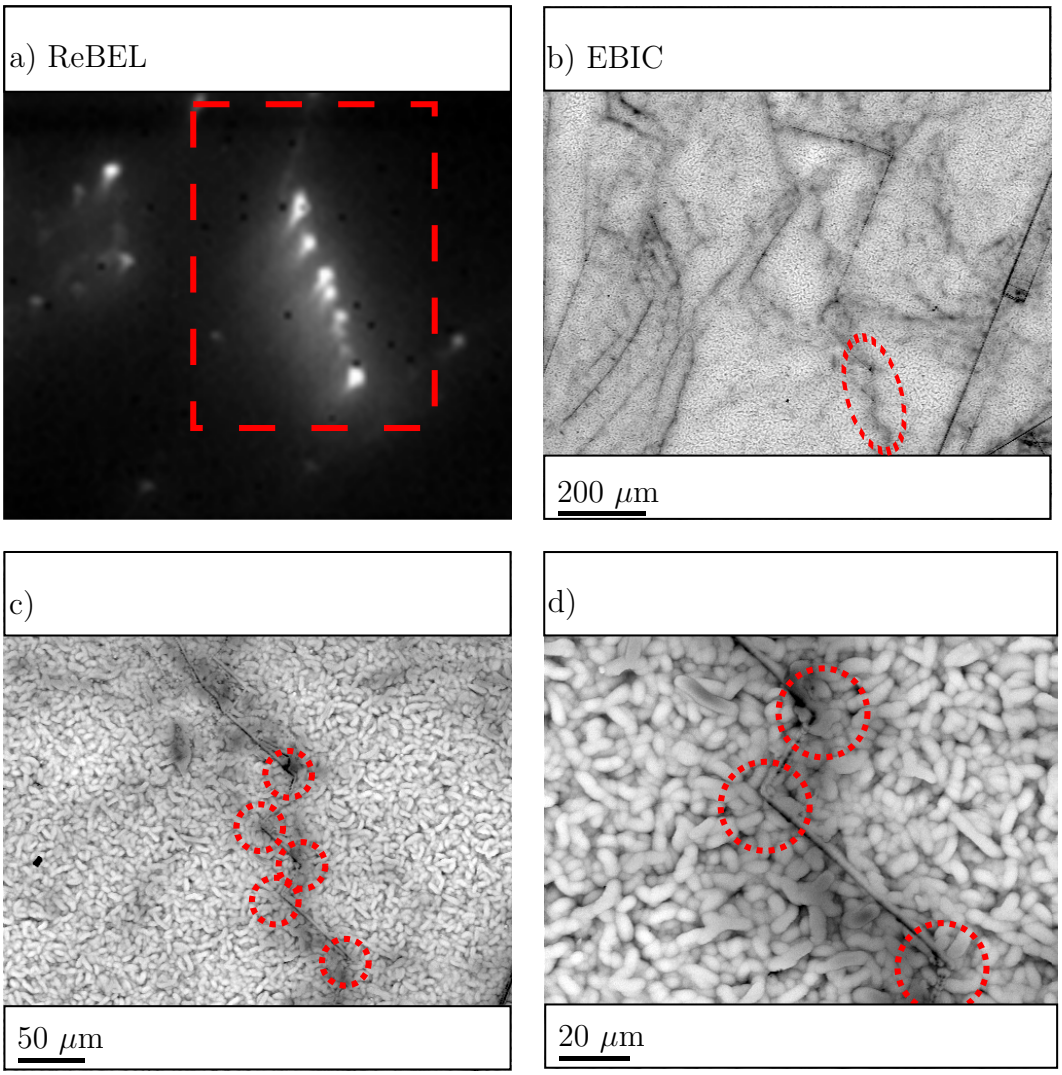

Figure 3.6: ReBEL image of breakdown type 3 *a)* and corresponding EBIC images with different magnifications *b)*, *c)*, and *d)*.

EBIC micrographs from the corresponding sample area with different magnifications. It reveals that the luminescence spots could be correlate with the step-like run of the grain boundary, marked in Fig.3.6 *c)* and *d)* with circles. The shadowed zone around the grain boundary indicates according to Mankovics, Krause et al. [58] a zone of enhanced recombination. Carriers generated in the vicinity of the GB recombining predominant at the grain boundary instead of moving toward the surface p-n junction and contributing to the EBIC [58]. At the marked spots are some recombination active defects to observe. It was suggested in [58] that at these breakdown sites the excess charge carriers are heavily depleted and could thus not combine radiative which according to the authors may explains the missing D1 luminescence there. It was also shown in Mankovics, Krause et al. [58] that sample areas emitting D1 luminescence and sample areas with

breakdown of type 3 seems to anti-correlate. The former mentioned etch pits [3; 9] could also be observed. One selected example is presented in Figure 3.7 showing an EBIC image in comparison to a secondary electron (SE) image with selected spots, which are suggested to be etch pits, marked with arrows, appear dark in the SE image on the right and bright in the EBIC image on the left side. A lower signal intensity in SE imaging process is usually related to a surface dip. The maggot-like structures are caused by the surface roughness resulting from the cell process.

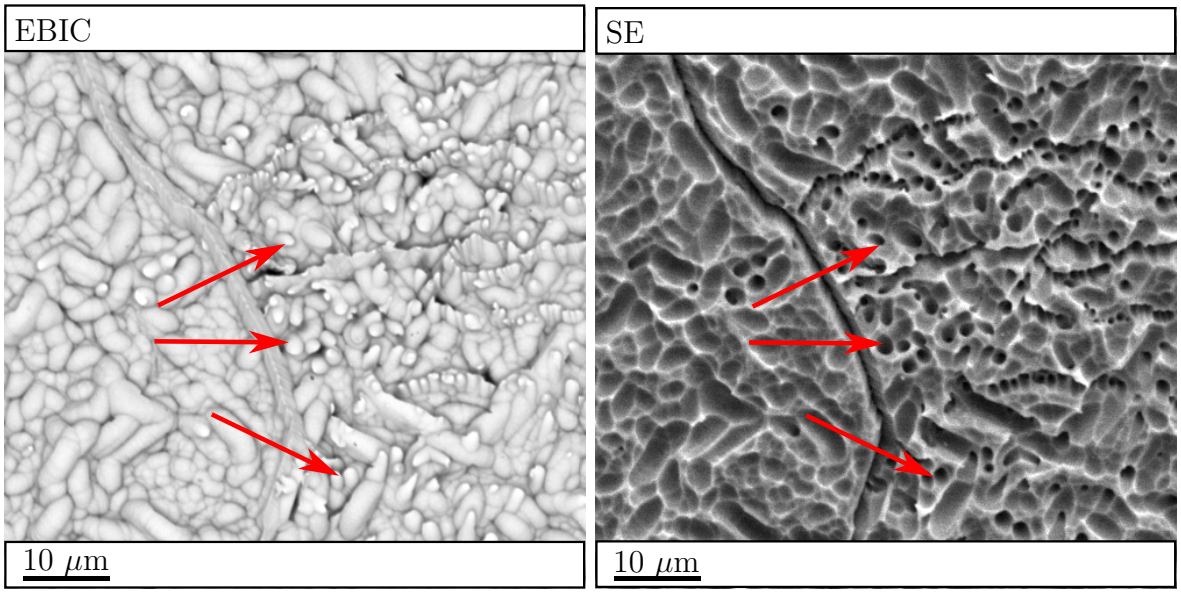

Figure 3.7: Comparison of EBIC (left) and SE (right) image at a breakdown defect side with selected marked etch pits.

Efforts were made to use a coupled EBIC-CL system to identify the spatial position of the breakdown spots with a higher accuracy, although unfortunately the measurements could not be completed with satisfying results. The emitted luminescence was possibly not sufficiently intense and thus could not be distinguished from the noise. To improve the signal to noise radio long time measurements were necessary. However, during conducting the investigation, the contacts at the sample do not withstand the high voltage this long and burn out. Besides the defect investigations at full processed umg solar cells (Mankovics, Krause et al. [58]) also other EBIC measurements at as-cut mc-Si block cast material were performed. Some of the observations that could occur are shown in the following.

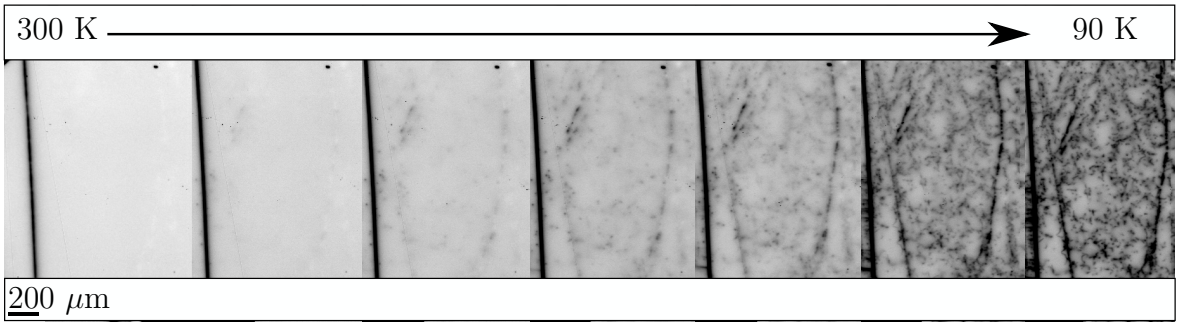

Figure 3.8: Temperature influence at observation of defects using EBIC at 30 keV and 100 pA.

Almost always dislocations appear dark while performing low temperature measurements at mc-Si. In Fig.3.8, the temperature influence at the EBIC investigations is shown. On the left side, there is only one dark GB to observe and the grain seems evenly bright. However, during the cooling process, increasingly more dark dots and lines were revealed. These dark features are attributed to thermal activated dislocation defect structures. For this reason, it is important to perform low temperature measurements. At room temperature, the most defects in the material are not observable but they could also affect the solar cell performance and are not homogeneously distributed over the entire sample.

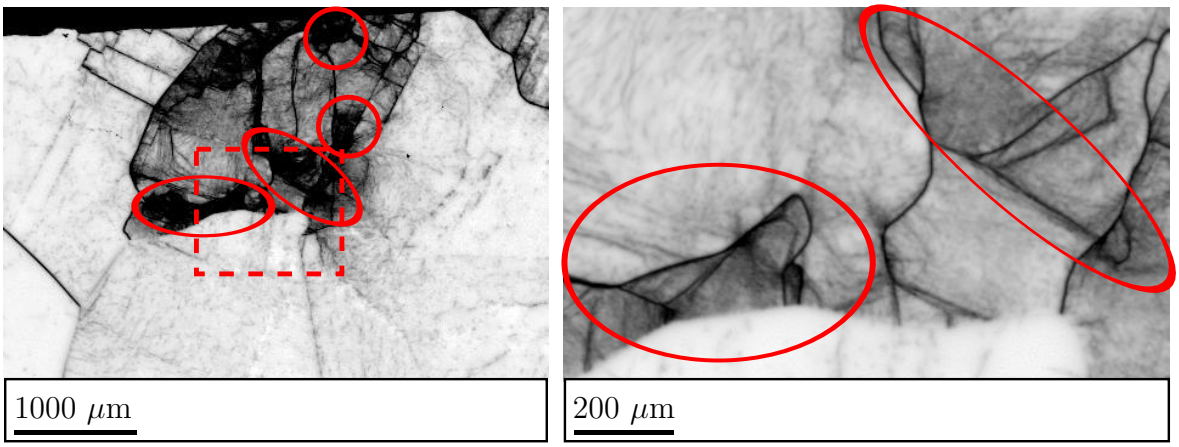

Figure 3.9: EBIC current variation caused by dislocation density alteration, marked spots containing high dense dislocation clusters, EBIC at 30 keV, 100 pA and 80 K.

As shown in Fig.3.9, there could be grains with almost no dislocation, bright on the left image, as well as grains with a high density of dislocations, dark on the left image. At the position marked with circles, dislocation clusters are located, which emerge as areas showing almost no EBIC collection efficiency. It looks like there is some kind of

seed and from this spot, the dislocation sprouts into the material. As shown in Fig.3.9 on the right and in Fig.3.10 *a)* it is possible that these low efficient areas are bordered by GB and the neighboring grain only contains a low amount of dislocations, revealing a certain higher collection efficiency.

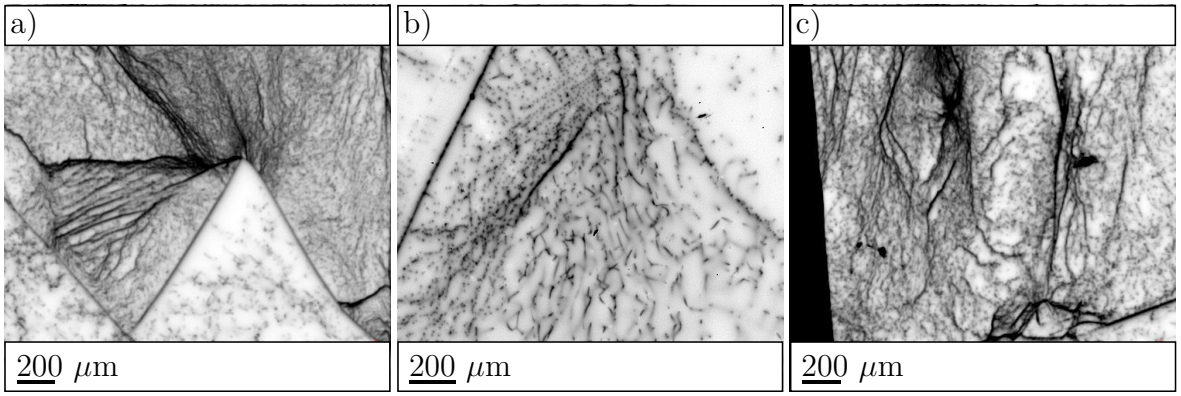

Figure 3.10: High dense dislocation clusters, EBIC at 30 keV, 100 pA and 80 K .

Furthermore, in Fig.3.10 *b)* it is obvious that the dislocations are run at an angle. It reveals at the upper part of the image where several short dark lines are visible. These lines have a black tip at the position where they hit the surface and they become slightly brighter the further away the dislocation slopes from the surface. When just a black dot is to observe the dislocation may lies perpendicular to the surface. Image *a)* of Fig.3.10 is a vertical cut of the bottom region of a silicon ingot. The most dislocations are located along the grow direction and show tree like structures. The entire sample, where the zoom shots Fig.3.10 *a)* and *c)* originate from, was previously shown in section 2.4.2 in Fig.2.23. The images of Fig.3.11 are also vertical cuts.

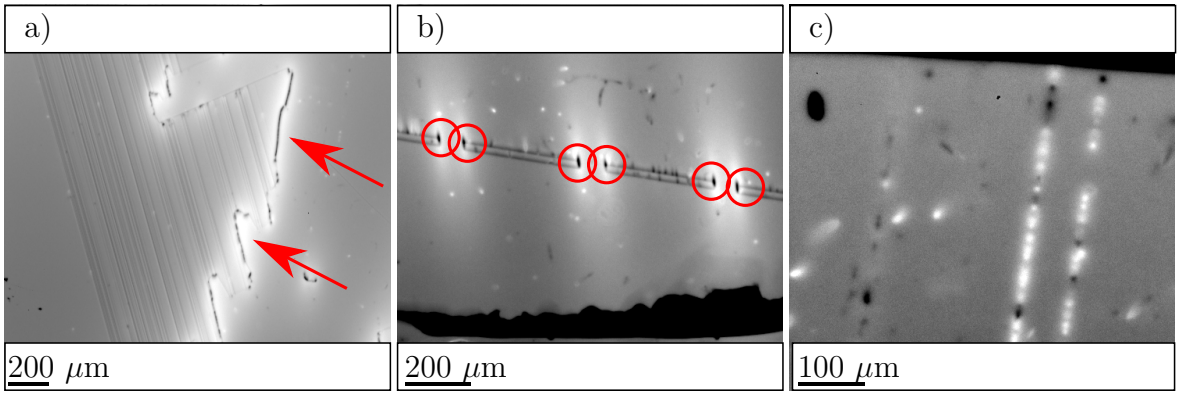

Figure 3.11: Getter zones around GB at bottom samples *a)*, *b)* and bright dots *c)*, EBIC at 30 keV, 100 pA and 80 K.

They were chosen because they show getter zones around GBs, observed at the highly

contaminated bottom of silicon ingots. GBs could act as getter centers. Defects of the surrounding material could accumulate by the GB and thus a bright belt around the GB appears, indicating a higher EBIC efficiency. In Fig.3.12, a line profile is superimposed over the EBIC micrograph at the position of the measured profile, marked dashed orange across the sample. It is noticeable that at both sides of the GB the efficiency rapidly increase while the electron beam approaches the GB. The GB core itself remains dark with a high recombination contrast.

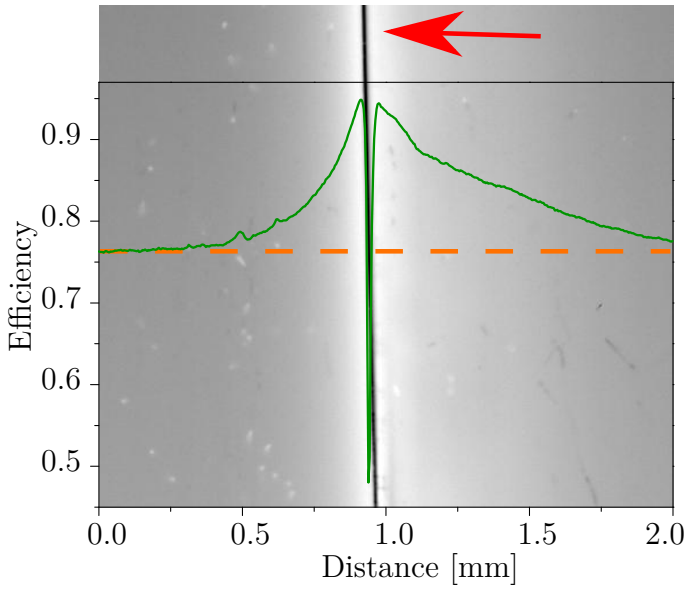

Figure 3.12: Getter zone around a GB and superimposed efficiency line profile from marked position, EBIC at 30 keV, 100 pA and 80 K.

Inside of these bright areas, marked with arrows in Fig.3.11 and in Fig.3.12, are less defects located than in the rest of the grains. The small bright dots are electrical active defects, which are usually only observable at contaminated material like block bottom or top. Image *a)* of Fig.3.11 shows a multi twin boundary structure with several closely located twins. At these twins are almost no dislocations or defects to observe. Twin boundaries will be the topic of chapter 5. Just the irregular dark boundary at the end of the twins shows a higher recombinations activity and an additional getter zone around them. The marked dark spots with bright belt marked with circles at image *b)* could be interpreted as GBs, pierce through the vertical cut. The almost regular structure of the black dots and the non-active GB lines could possibly indicate up and down steps between parallel vertical layers. However, further investigations remain necessary for a more detailed and accurate analysis. The electrical active defects appearing in Fig.3.11 *b)* and Fig.3.12, distributed all over the grains, could also be observed along GBs (Fig.3.11 *c)*) forming irregular pattern.

3.2 Thin-film Si

In addition to the established standard characterization methods at mc-Si material, some measurements at silicon thin-film material could also be successfully performed. As already mentioned in [42], there are many different thin-film solar cell setups with various materials, amorphous or crystalline silicon, for example. With these two materials, several types of cells were produced, p-n junction cells as well as p-i-n heterojunction cells, also with different amount of layers. To crystallize the thin-films are various possibilities available. Using an electron beam for crystallization is a possibility to produce thin crystalline layers. One of the investigated samples shown in Fig.3.15 is produced in the following way. "The samples consist of a 250 nm thick amorphous SiC:B layer, deposited by RF magnetron sputtering onto a commercial available glass substrate (Corning EagleXG) of around 1 mm thickness. This layer acts as diffusion barrier and supports the wetting of Si. The Si absorber is deposited as amorphous to nanocrystalline Si by a LPCVD process (Low Pressure Chemical Vapor Deposition). The nominal thickness is about 10 μm. After deposition, the absorber becomes subsequently crystallized by using a line shaped electron-beam with a constant scanning speed. So the silicon starts to crystallize to large grains with a typical grain size of a few hundred micrometers in the broadness and a few millimeters in the length" [41].

The sample shown in Fig.3.13 is an a-Si:H/μc-Si:H tandem cell at glass substrate.

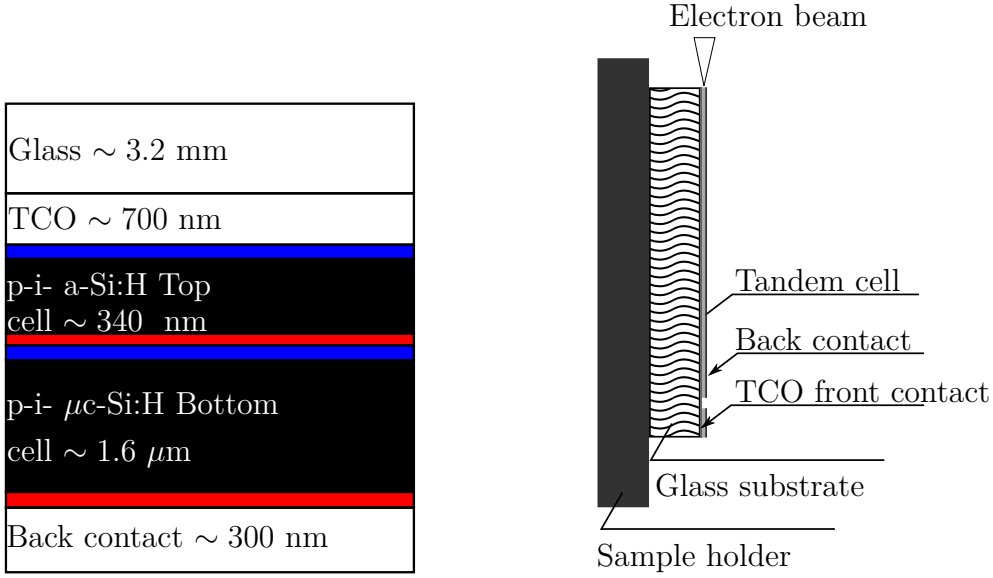

Figure 3.13: Scheme of the a-Si:H/μc-Si:H tandem cell. Blue, black and red are the p-, i- and n-layers, respectively; drawing after [42] (left). Scheme of the cross sectional EBIC setup for thin-film Si measurements (right).

The detailed description of the investigated samples is given by Klossek, Krause et al. [42] "They consisted of a hydrogenated amorphous silicon top cell (340 nm) to absorb the shorter wavelength of the sun spectrum. A hydrogenated microcrystalline silicon bottom cell (1.6 μm) was placed above the a-Si:H top cell to absorb the longer wavelength of the sun spectrum. Both cells were p-i-n structures. The p- and n-layers had a thickness of around $15 - 40$ nm, respectively. The silicon layers were deposited by plasma enhanced chemical vapor deposition (PECVD) on a 3.2 mm thick glass substrate. This was coated with front TCO consisting of SnO_2:F (0.7 μm). As a back contact a ZnO:Al/Ag layer with a total thickness of about 70 nm ZnO:Al and 200 nm Ag was deposited by sputtering". The EBIC measurements were conducted using the processed back contact and the TCO front contact of an entirely processed cell. In contrast to the measurements at bulk Si, described already in section 2.4.2, this time the investigation were performed in a cross sectional setup, which could be performed at tandem cells for the first time, according to Klossek, Krause et al. [42]. Cross sectional measurements were chosen to distinguish between the different layers of the samples. The standard front-side method would provide mingled information from all layers with no chance to differentiate between them. For the investigations a small sample must be provided by breaking the layers and the glass substrate producing an as flat as possible fracture plane. Sawing and or mechanical polishing would destroy the thin layer configuration in a way that the measurement analyzing would be impossible. Chemical treatment with acid for chemical polishing is also no option because in the worst case the thin-films could be vanished within seconds. The samples were mounted at a special developed sample holder to investigate the cross section of the layer-stack (Fig.3.13). The, compared to the Si-layer, thick glass substrates aggravated the measurement. Glass inclines to become charged and this could disturb the investigation. The optical imaging becomes unstable which shows up with a feigned "floating" of the sample, resulting in an unusable image. Another problem was the wish to distinguish between the layers. They are only some nm to a few microns thick and thus a high magnification is required at samples that tend to become charged. For this reason, the measurements were performed at a time where no one else uses any electrical equipment in the entire lab building to prevent disturbance in the signal processing between the SEM and the evaluating computer through the grid. Furthermore, beam energy and current was chosen in a way to reduce the substrate charging without affecting the EBIC and SE signal.

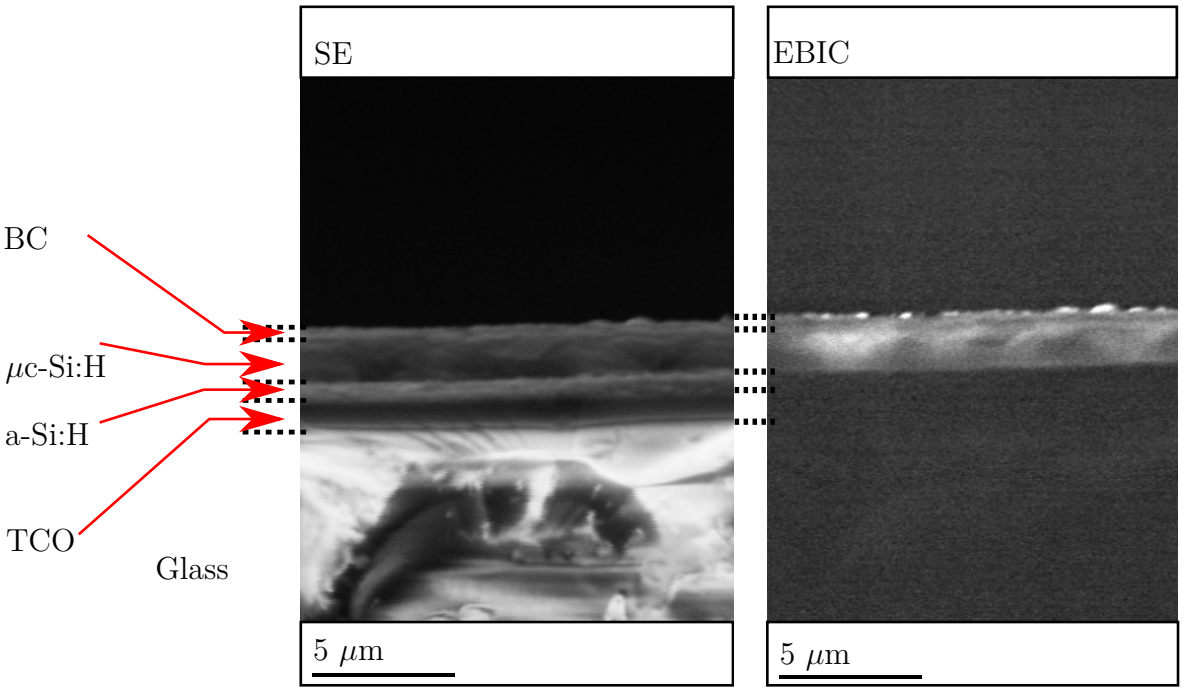

Figure 3.14: Cross sectional EBIC on tandem cells: Comparison of secondary-electron image (SE), giving topological information, with EBIC image showing the electrical activity. 25000x Magnification, 15 keV and 100 pA at 300 K [42].

As explained by Klossek [41], the missing EBIC signal from the a-Si:H layer could be caused by a high amount of non-radiative recombination. Another more probable reason could be a missing connection between the contact and the layer. Thus, no carriers from there could be collected.

The recombination contrast at EBIC measurements usually increases with decreasing sample temperature. However, the thick glass substrate, which is a bad heat conductor, rendered it complicated to cool down the sample. Even with longer cooling down periods, it is not possible to determine the sample temperature because there is no mounted temperature sensor at the sample surface. Nevertheless, cooling could reveal some interesting features at the thin-film samples. In Fig.3.15, an EBIC image taken with a standard EBIC setup from an electron-beam crystallized Si thin-film sample is presented. Measurements at thin-films with standard EBIC bring along some analysis problems [41]. The beam energy, which as in sections 2.4 and 2.4.2 described, determines the penetration and therefore the information depth. Due to the high interface roughness and the mostly unknown composition of the back contact, it is difficult to estimate a reliable information depth. The observable fish scale structure in Fig.3.15 indicates enhanced non-radiative interface recombination at the Si/SiC:B interface [41].

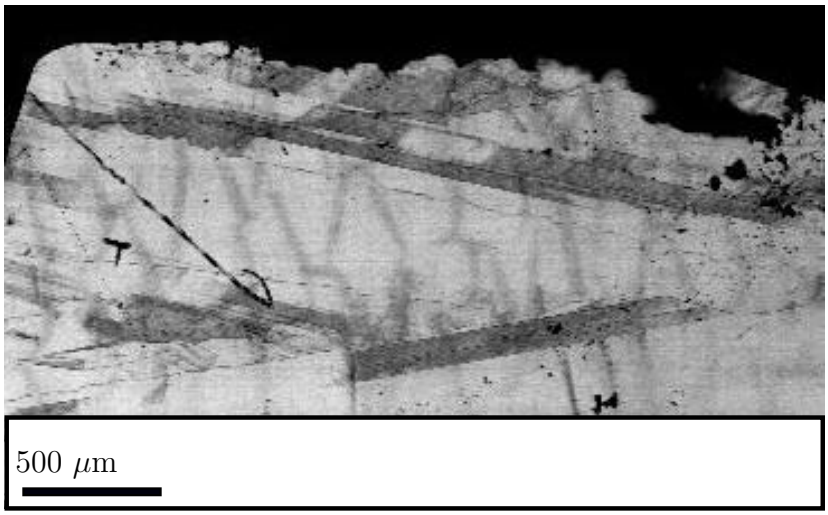

Figure 3.15: Low temperature EBIC-image at electron-beam crystallized sample, 10 keV and 100 pA.

Many other defects could also be found at thin-film samples. In Fig.3.16, EBIC-images are shown from an additional investigated thin-film sample at room temperature 300 K and at low temperature approximately estimated $\sim$ 90 K. At this laser crystallized

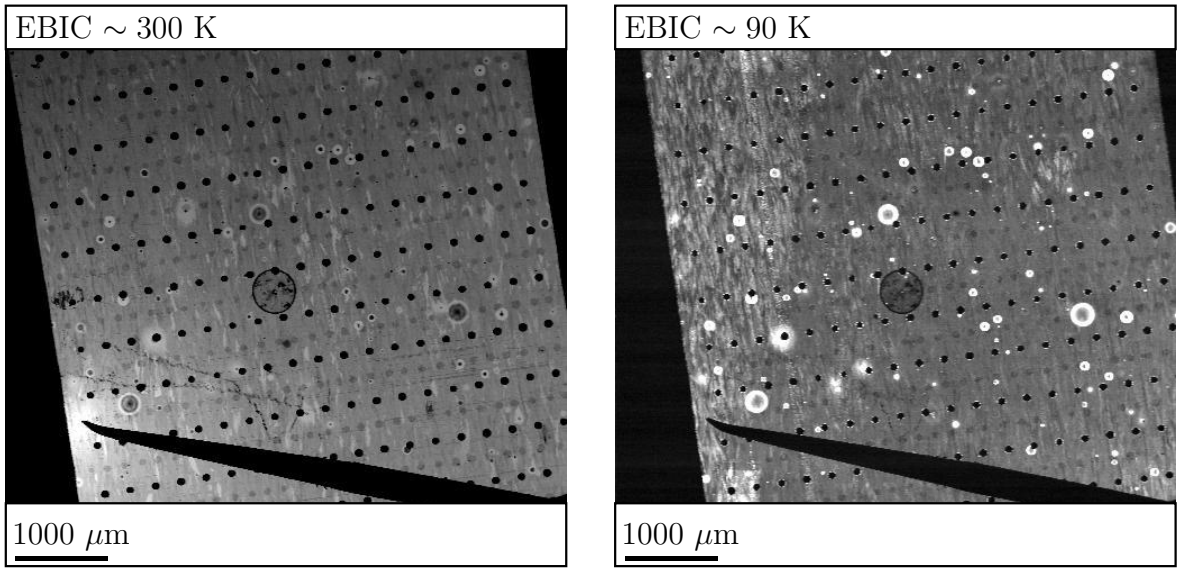

Figure 3.16: EBIC sample overview images at room temperature 300 K and at low temperature.

sample, the glass substrate was cut down to $\sim$ 120 μm to improve the cooling process. The attempt to entirely remove the glass substrate mechanical as well as chemical was not successful at any sample. After removing the glass substrate with HF-acid, the thin-layers become unstable and fall apart.

Further difficulties at this sample accrued through the contacts at the solar cell. One of the contacting needles was placed at one of the emitter touching holes and the other one was placed at one of the p-substrate contacting dimples. These needle placements have to be undertaken under optical magnification with the help of a microscope because the contacts have a diameter of just $\sim$ 100 μm. These small contacts generate an additional problem during the cooling due to different heat expansion. The needles tend to drift a little during cooling which could be sufficient to cancel the contact. The circular defects, which could be observed at the sample, are describe in detail by Schneider et al. [81]. It is supposed that they originate from "holes of a few μm diameter in the seed layer" [81] or "bulges formed by local delamination of a few μm at the seed/ epi layer interface" [81]. In the close up image, shown in Fig.3.17 *a)*

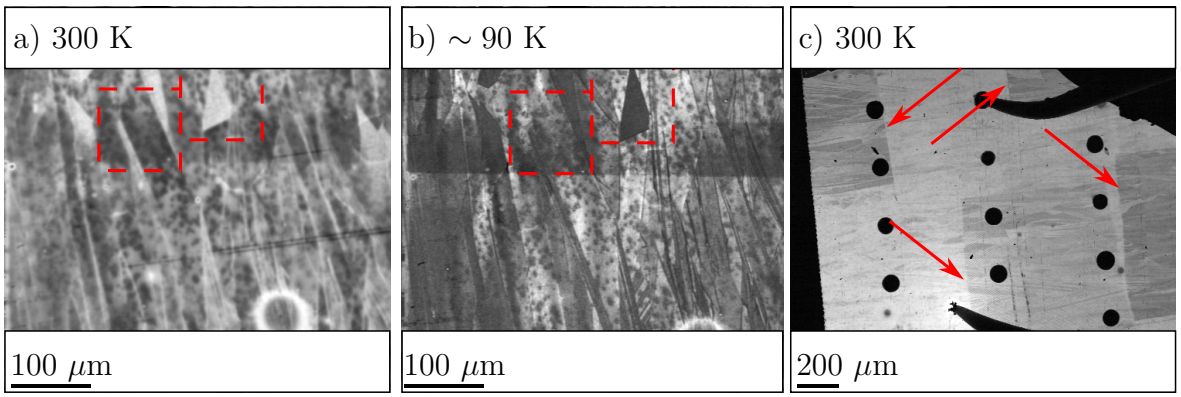

Figure 3.17: EBIC close up images at room temperature 300 K *a)* , at low temperature *b)* and at another sample at 300 K *c)*.

and *b)*, at higher magnification a contrast inversion could be seen. Up to the date of investigation it could be the first time that such investigations on crystalline silicon on glass were realised. In the marked areas, the measured current contribution switches during cooling, whereby some areas appearing bright at room temperature in image *a)* and switch at low temperature to dark in image *b)*. The opposite could also be observed, whereby dark areas from *a)* reveal bright at low temperature, as shown in image *b)*. To date, it is not entirely understood how the temperature induced change works. In general, an occupation of trap states could possibly be considered as an explanation. Image *c)* of Fig.3.17 should show the induced change of surface recombination due to electron beam irradiation. The arrows point to the rectangular structures build during investigation using higher magnification before the overview image was taken. This kind of enhanced surface recombination render it complicated to interpret the EBIC measurement data. Long time investigations have to be avoided and highly magnified investigations are also difficult to perform because the irradiation dose would increase.

Therefore, it is not possible to distinguish whether irregularities in the recombination active regions originate from the surface or from the bulk silicon.

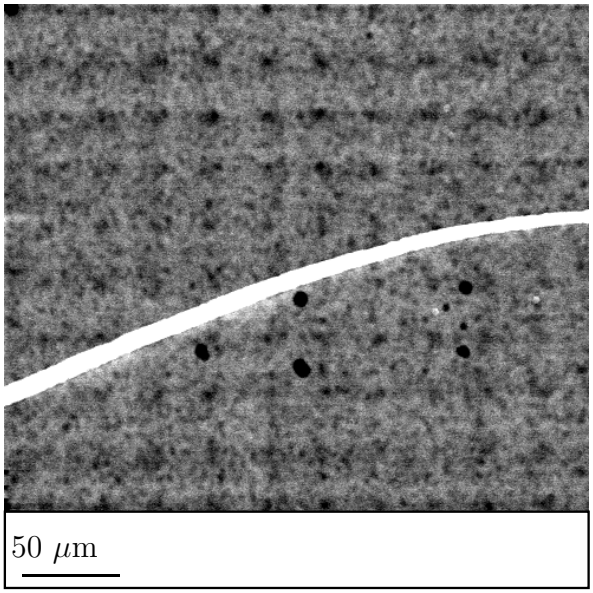

Figure 3.18: EBIC image at room temperature 300 K with electron beam damage, the white stripe across the entire sample is a scratch at the surface.

Furthermore, this sometimes high electron beam sensitivity of the samples leads to unexpected defect features as the grid like structures shown in Fig.3.18. The EBIC imaging process is a scanning process and to generate overview images for the localization of interesting investigation spots, the electron beam will scan fast over the sample at low magnification. It seems that thereby the sample becomes damaged and the produced grid will be visible at a higher magnification. Klossek [41] reported another also possible explanation for the grid structure. It is assumed that the observed structure is already latent in the cell structure and becomes activated by the electron beam. Due to the light-induced degeneration of the samples the point structures becomes visible through scanning the sample with the electron beam. If no scanning process is going on, the electron beam moved out of the investigated area and is placed above the left upper corner of the image. After changing the investigation area, the positions where the electron beam former strikes the sample appear as black dots, like in the middle of Fig.3.18. An also not negligible influence at the EBIC measurements is the surface structure. At high magnification in Fig.3.19, it is shown that the SE image *b)* correlates very well with the EBIC image *a)*. The superposition of *a)* and *b)* is shown in *c)* (EBIC signal in green and SE in red). The structure of the surface remains present at all electron beam energies.

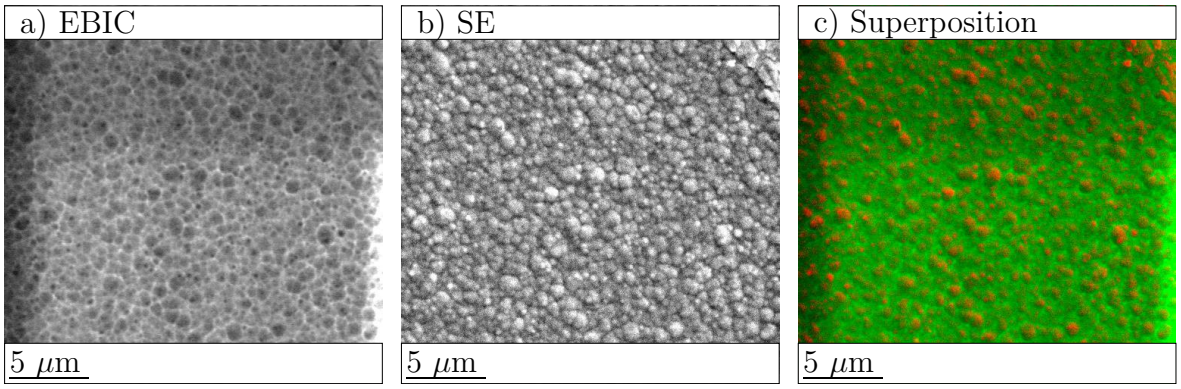

Figure 3.19: *a)* EBIC image at 20 keV, 100 pA and 25000x magnification compared with *b)* the SE-image with the same measurement settings and the superposition *c)* of *a)* and *b)*.

3.3 Summary

In the first part, a wide variation of different radiative and non-radiative defects in mc-Si could be observed during measurements for this work. The knowledge about the defect mechanism remains incomplete and that even after long time investigations by many researchers over recent years.

Through performing CL measurements, indications for oxygen related luminescence at room temperature and at 10 K could be found next to the D1 luminescence line. As already reported in literature, the observed luminescence at 0.77 eV should be the, so-called P-line, whose origin is still subject to heated discussions. In contrast to the previously reported results in literature, it was possible to observe the P-line and the D1-line clearly distinguishable from each other at once at 10 K. For this reason further investigation seems reasonable.

Enhanced BB luminescence at GBs in comparison to the surrounding grains could be observed. Unfortunately, it was not possible to prove these measurements through repeated measurement efforts in St. Petersburg. Due to the lack of satisfying explanations, future research is necessary.

An intense luminescence at 0.93 eV at room temperature could be detected. This luminescence will be the single topic of the next chapter.

Always, during standard EBIC investigations, many different recombination active defects occur. Temperature dependent EBIC contrast at GBs, non-recombination active twin boundaries, getter zones around GBs, and highly recombination active dislocation

clusters to name just a few of the often observed features. Furthermore, these are not fully understood at present. Due to the high amount of occurred defects and the time consuming measurements, it is only possible to pick a few defects and investigate them in more detail rather than focusing on every single one just for a short time. For this reason, in the fifth chapter solely low temperature investigations at twin boundaries are discussed.

The thin-film section shows the possibility to use established mc-Si measurement methods like EBIC at thin-film Si samples. Whereby measurement issues could appear due to high electron beam sensitive silicon thin layers and the glass substrate can also become charged during electron beam irradiation. Furthermore, the thick substrates render temperature dependent measurements much more challenging. Sample holders have to be customized to handle thick samples, provide cross sectional measurements, or enable placing the back contact also at the front side. Moreover, the sample preparation also becomes complicated. Chemical etching or polishing thin sample structures have to be undertaken extremely carefully to prevent layer damages. If the supplier provided no possibility to bond the backside-contact, it was difficult to produce good conducting self-made contacts. The interpretation of obtained measurement data is highly complicated because there is not much known about interface interaction between the different layers of the thin-film structure. Moreover, due to the thin layers, it is difficult to distinguish if the obtained data originate from surface, bulk, or the substrate. Nevertheless, for the first time cross sectional investigations at tandem cells could be successfully conducted. Furthermore, it could be possible that for the first time, up to the date of the measurements, contrast inversion at crystalline silicon on glass was investigated with a common EBIC setup.

4 Investigation of the intensive luminescence at 0.93 eV

This chapter embraces the investigation of the observed intense luminescence at the spectral position of 0.93 eV and is mainly based upon the two previous published articles by Krause et al. [45; 44].

"Typically, at RT the band-band (BB) radiative transition at around 1.1 eV and defect luminescence at around 0.8 eV are observable. This defect luminescence is usually associated with recombination on extended defects such as dislocations and grain boundaries. The spectral features (D1-D4) [16] were associated with different transitions on dislocations and usually observed in plastic deformed silicon below 130 K. [95] The four main dislocation related luminescence lines labeled D1 (0.81 eV), D2 (0.87 eV), D3 (0.93 eV) and D4 (1 eV) appear in multicrystalline (mc)-silicon as well, although their exact spectral positions may vary from sample to sample slightly" [45].

"Besides BB and D1 luminescence a defect-related feature has been recently reported at 0.93 eV. [2; 15] It is observed at room temperature on grain boundaries or in their vicinity. Usually, the region where that defect radiation is detected extends over several millimeters along the boundary. Although, the defect luminescence appears at the grain boundaries and its spectral position is close to that of D3, there are reasons to suppose that it differs from D3. Indeed, the ordinary D3 line usually appears together with D4, both have nearly equal intensity and both are not visible at RT" [45]. In contrast, this new feature at ~ 0.93 eV which is refer to as Di line, since Krause et al. [45], shows a remarkable intensity even at RT. "It could easily be identified by photoluminescence imaging at RT" [45].

"Di radiation is usually very intense even at low excitation levels. It is not absorbed in silicon and could be potentially utilized for fabrication of silicon based light emitting devices for the emerging silicon photonics. Light emitters based on Di radiation could provide a viable alternative to Er doped silicon [60] and germanium on silicon structures. [55] However, an origin of Di luminescence and a possibility for fabrication of the

relevant defect structures should be studied first. Previously, the intense luminescence near D3 has been attributed to various recombination centers. [2] Based solely on its photon energy Cu-Cu pairs, [97] carbon related complexes [13] chalcogen (sulphur and selene) contamination, [10] or a particular state of dissociated dislocations [75] could be suggested as origin for such luminescence center at 0.93 eV. Newly published work [95] treats the luminescence center as related to the D3/D4 doublet, which persists above 130 K. However, the unusually strong intensity of Di line at room temperature renders those suggestions low probable" [45].

The approach followed in this chapter "is to select typical areas of solar grade material showing Di luminescence and examine those by means of high spatially resolving cathodoluminescence (CL) spectroscopy. The local non-radiative recombination activity is investigated by electron beam induced current (EBIC)" [45]. Moreover, H.-M. Krause applied electron backscatter diffraction (EBSD) analysis to find the orientation of the grains forming the boundary and correlate their crystallographic structure with the appearance of Di luminescence. Dr. A. Hähnel performed additional TEM measurements with the aim to associate the Di luminescence with partial dislocations and confirm the suggestion of existing partial dislocations at Di luminescence spots.

4.1 Experimental results and discussion

The investigations were performed at mc-Si wafers at different stages of their processing to solar cells (as-cut, textured and full processed). "Detectable Di luminescence has been observed at all stages and there was no indication of modification of Di emission due to the cell process. That is why for further investigations pieces were used, cut from fully processed solar cells, where the passivation coating prevents recombination activity at the bare silicon surface [63] and allows an easy identification of the Di emitting regions by PL imaging. Samples of 1.1 × 1.1 cm were cut out from the wafer for further investigations by PL, CL, EBIC, and EBSD" [45].

4.1.1 First time localization of the luminescence with PL imaging and PL mapping

Due to the high intense luminescence, the first localization of the intense luminescence at entire wafers could be achieved through PL imaging [59; 78; 79] by D. Mankovics who performed the PL measurements. PL imaging is a camera based very fast measurement method. The samples were excited with an array of LEDs from the backside and the luminescence emitted was recorded with a CCD camera placed above the sample.

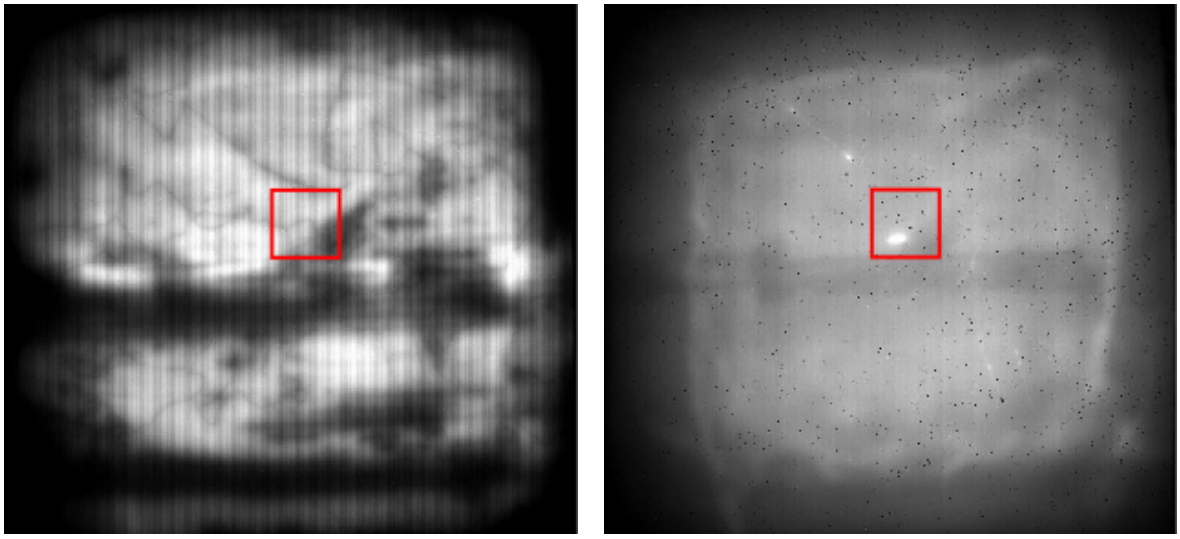

Figure 4.1: PL image of 6 × 6 in solar cell with BB (left) and D3 (right) filter at RT (300 K)

As shown in Fig.4.1, the observed luminescence in the marked area is remarkably high. The apparently low contrast is related to the used filter. The BB luminescence is not

entirely blocked by this D3 filter. Therefore, the whole sample seems to emit light in the region of D3 whereas it is just a BB tail. PL mapping provides a more detailed insight in the distribution of the luminescent defects. For this reason, it is possible to confine the investigation area in the following of a small part (1.1 × 1.1 cm) of the region where the intense luminescence feature is located (Fig.4.2). At the PL maps in Fig.4.2, the BB and D3 maps at 300 K and 80 K are compared with each other. The intense Di luminescence at just one GB is observable at 300 K *(b)* and as well at 80 K *(d)*. The BB map at 300 K *(a)* shows at this GB no noticeable contrast while at 80 K *(c)* there is an increased dark contrast to observe and the GB is clearly visible. GBs often contain an enhanced level of defects. Through the cooling process, these defects became activated and the BB luminescence will be reduced. As already explained in

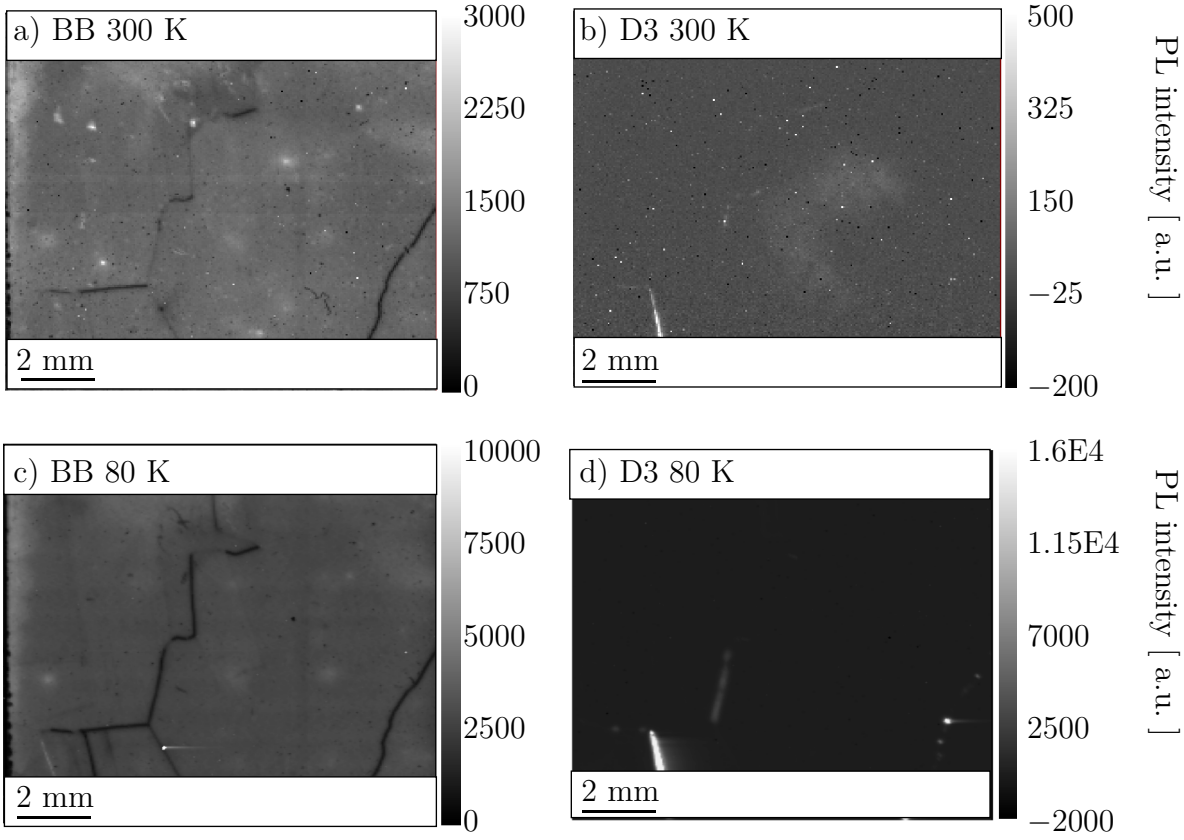

Figure 4.2: PL map of a 1.1 × 1.1 cm solar cell with *a)* BB 300 K, *b)* D3 300 K and *c)* BB 80 K, *d)*D3 80 K

[44], "typically, the luminescence spectra taken on multicrystalline silicon show two distinct futures, related to transitions on extended defects (D1) and to BB radiative transition. Fig.4.3 (left) shows two spectra recorded on a defect rich region from a solar cell at 300 K and at 80 K", where these two features are present. "The red shift of the

luminescence lines at room temperature compared to 80 K is always observed and is related to the temperature induced band gap narrowing of silicon [51]. The intensity of these luminescence lines depends on the local minority carrier concentration and the local defect density" [44].

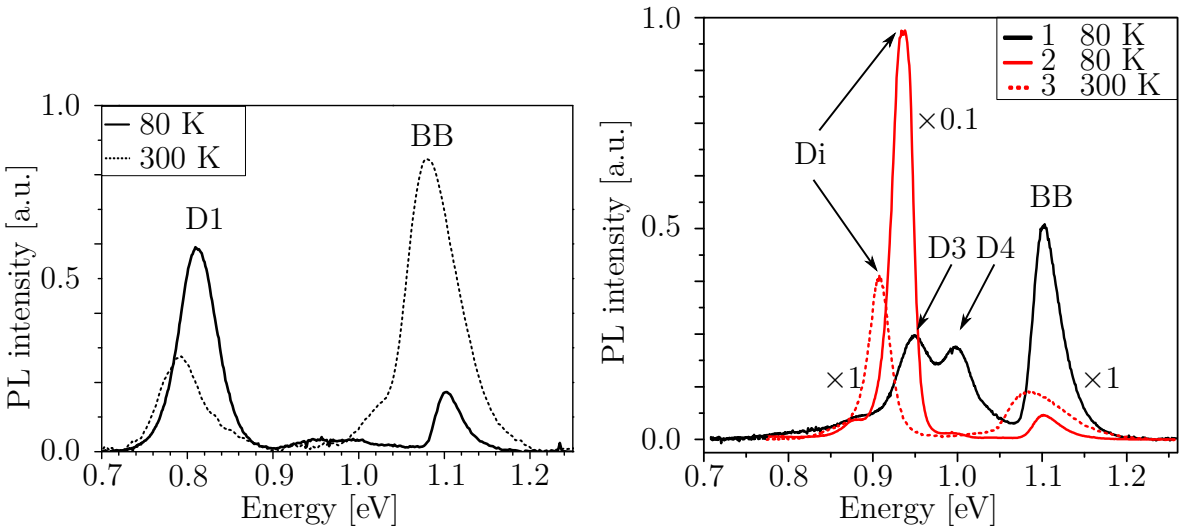

Figure 4.3: Typical PL spectra showing BB and D1 luminescence in mc-Si at 80 K and at 300 K (left)[44] and PL spectra detected from mc-Si: (1) spectrum from a location with ordinary D3/D4 doublet at 80 K; (2) and (3) spectra from a location with Di luminescence at 80 K and at 300 K, correspondingly (right)[45]. Note, that the amplitude of the signal for spectrum (2) was reduced 10 times.

"Besides D1 there are areas where other lines of the dislocation spectrum are present. An example is given in 4.3 (right). The figure also demonstrates the difference between the Di and D3/D4 luminescence. It shows three spectra: a spectrum with the usually observed doublet of D3/D4 (curve 1) and spectra with Di luminescence at 80 K *(2)*, and 300 K *(3)*. D3 and D4 are detectable at lower temperature only. Both peaks have similar intensities and widths. In contrast, Di appears as a single strong peak at room temperature and its intensity exceeds that of BB luminescence. It also shows a temperature-related red shift" [44].

4.1.2 CL and EBIC investigations with high spatial resolution

In the following, the investigations will be focused at the luminescent GB only. Due to the higher spatial resolution, provided by CL measurements, this method will be used to correlate the results with these collected with EBIC and EBSD. Temperature, beam current and beam energy dependent CL and EBIC results will be discussed also in this section.

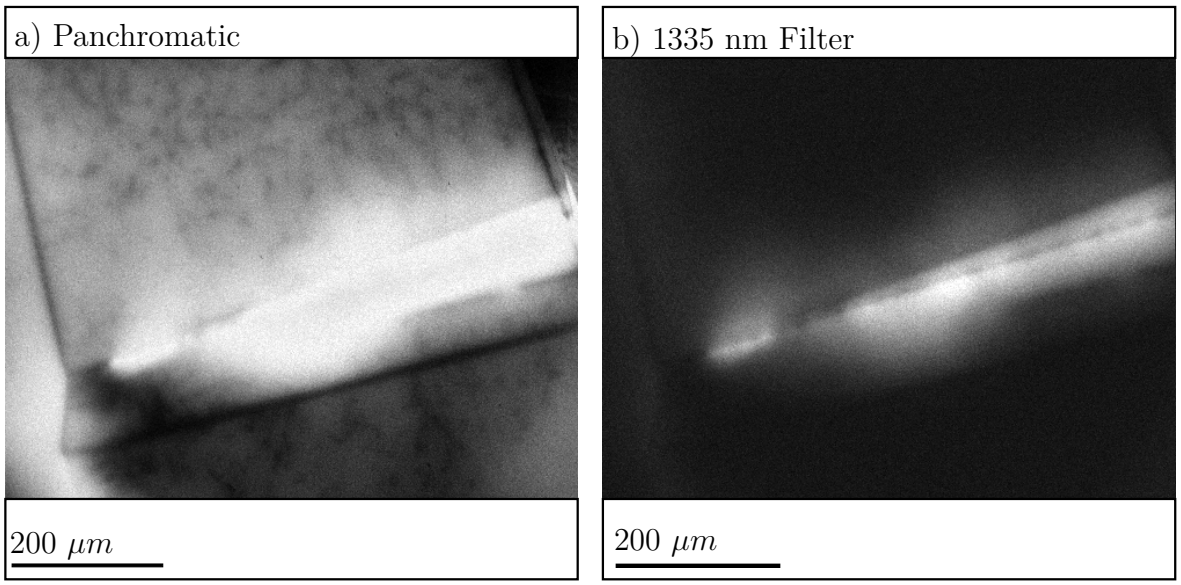

Figure 4.4: CL images of a preselected area with GBs *a)* Panchromatic CL image and *b)* Di (1335 nm) luminescence. Both images were taken at 10 K [45].

"A panchromatic CL image is shown in Fig.4.4 *a)*, which reveals areas of bright luminescence at the grains caused mainly by BB radiative transitions and dark linear images corresponding to some of the grain boundaries. At the grain boundaries non-radiative recombination prevails and the radiative transitions are suppressed. [63] The strong emission detected around some of the grain boundaries is mainly due to defect luminescence at 0.8 eV (D1) and 0.93 eV (Di). Figure 4.4 *b)* presents a monochromatic CL image of the same sample location taken at the spectral position of Di emission. An entire straight segment of a grain boundary emits Di radiation, whilst the rest of the grain boundaries and the grains themselves remain dark. One should note that the Di radiation is non-homogeneously generated along the grain boundary line, but appears at certain randomly distributed spots. Such pattern is not typical for grain boundary - originated luminescence. Usually, it appears as a homogeneous bright stripes running along the grain boundary. Previously, two types of pattern were reported. [75; 25; 86]

One was a bright stripe straight at the grain boundary and the other consisted of two parallel bright stripes running on both sides of a dark grain boundary line. The presence of isolated, closely spaced bright spots is not usual, but appears characteristic for the Di emission" [45]. This characteristic could be also observed at other GB at different samples, as shown in Fig.4.5.

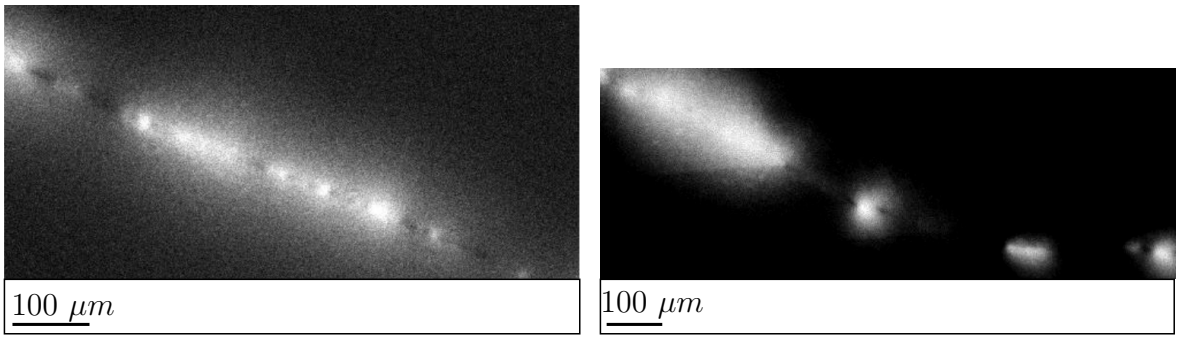

Figure 4.5: CL images of inhomogeneous Di (1335 nm) luminescence. Both images were taken at 80 K.

A typical Di spectra is shown in Fig.4.6. "In addition to the Di peak at 0.93 eV, a second one at 1 eV (D4) is present. Note that differently from the ordinary case of D3/D4 luminescence, the intensity of the D4 peak is much smaller than that of Di one" [45].

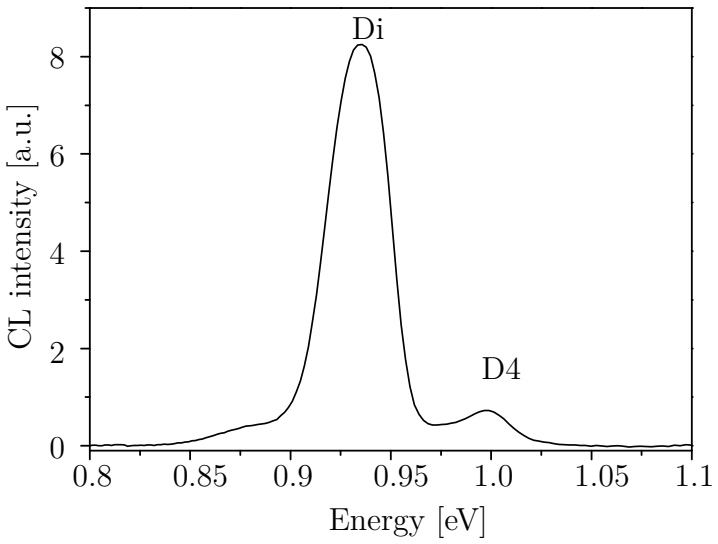

Figure 4.6: CL spectra of Di luminescence at 80 K, 30 keV and 28 nA and the temperature dependence of the Di luminescence at one chosen spot with 30 keV and 30 nA.

4.1.3 Estimation of the energetic position of the defect level

"Based on the temperature dependence of the recombination rate one can estimate the energy position of the band gap levels involved in the recombination" [45] (Fig.4.7).

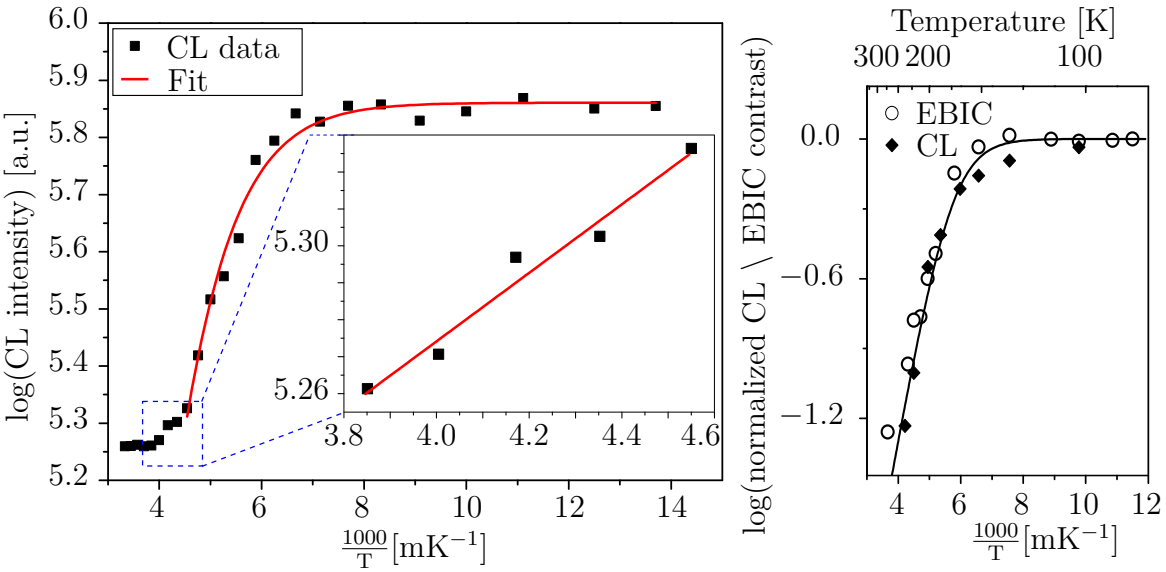

Figure 4.7: Arrhenius plot of the temperature dependence of the CL intensity; Inset with linear fit of the high temperature part (left). Arrhenius plot for the total recombination activity (EBIC) and radiative (Di) recombination activity (CL) together with a best fit to the model, for a grain boundary emitting strong Di radiation at another sample spot (right), after [45].

"The activation energy of Di recombination was determined by a fit of the temperature dependent CL intensity to a model for a transition between an electronic state in the band gap and the semiconductor bands. [76] The model takes into account, that the minority electrons trapped at certain level in the band gap can be activated thermally back to the conduction band. It is clear, that upon decreasing temperature the activation process would be suppressed and, accordingly, the probability for transition of those electrons into the valence band will increase. The energy offset of the defect level can be determined by fitting the experimentally measured recombination rates at different temperatures with: [76; 10]" [45]

$$R = \frac{1}{1 + CT^{\frac{3}{2}} e^{-\frac{E_A}{kT}}} \tag{4.1}$$

For Fig.4.7 (left) the recombination rate R is given by the intensity of the CL, C is a constant accounting for the degeneracy factor of the level and the density of

states in the band, kT is the thermal energy, and E_A is the energy offset between the defect level and the band edge. It is possible to obtain a value of 112 ± 9 meV for the activation energy E_A of the lower temperature part which is in a good agreement with the previously reported 115 meV [2]. The higher temperature part from 220 K up to 260 K shows another slope as the rest of the curve. Therefore, it is possible to conduct an additional linear fit for this region, which indicates an additional E_A of 93 ± 10 meV. This could suggest an additional defect level. Unfortunately the fit does not provide any information if the defect level is located below the conduction or above the valence band. In [45; 44] (Fig.4.7 (right)) we assume a recombination of the minority carriers through the estimated level located 120 meV beneath the conduction band in the p-type silicon. These former measurement data at another sample spot yield a comparable activation energy to the here presented data, but there was no indication for a change of the slope (Fig.4.7 (right)). But actually, the now suggested second defect level does not change the former provided band model. Fig.4.8 rather supports the model with the second missing energy. A similar energy barrier like the obtained $\approx 112 \pm 9$ meV could be introduce in the band gap of silicon by Frank partial dislocations [7; 33]. The "estimation of the activation energy of the level involved in the transitions is in agreement with those given in the references. Moreover, the photon energy of the radiative transition is also in good agreement with that theoretically estimated for transition at Frank partials. Indeed, the band gap narrowing due to the strain field around Frank partial dislocation [53] results in an energy of 0.9 eV, the value fairly well consistent with the experimentally observed 0.93 eV photon energy of the Di emission" [45].

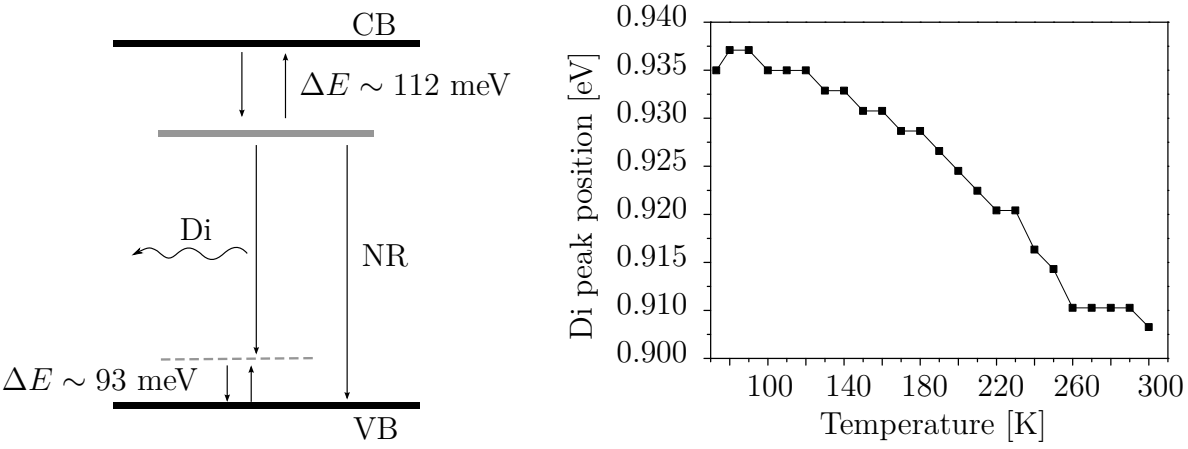

Figure 4.8: On the left image, the suggested band model for Di luminescent transition [45; 44] with additional energies and on the right the Di peak energy shift as function of temperature.

A similar pattern as shown in Figure 4.5 was also "observed on the EBIC micrographs, where the total recombination activity of the defects was monitored. Figure 4.9 (top) shows a pattern of dark points in the EBIC contrast of the grain boundary, previously examined by CL " [45] Fig.4.9 (bottom). It is evident that spots with intense Di luminescence also show a dark EBIC contrast.

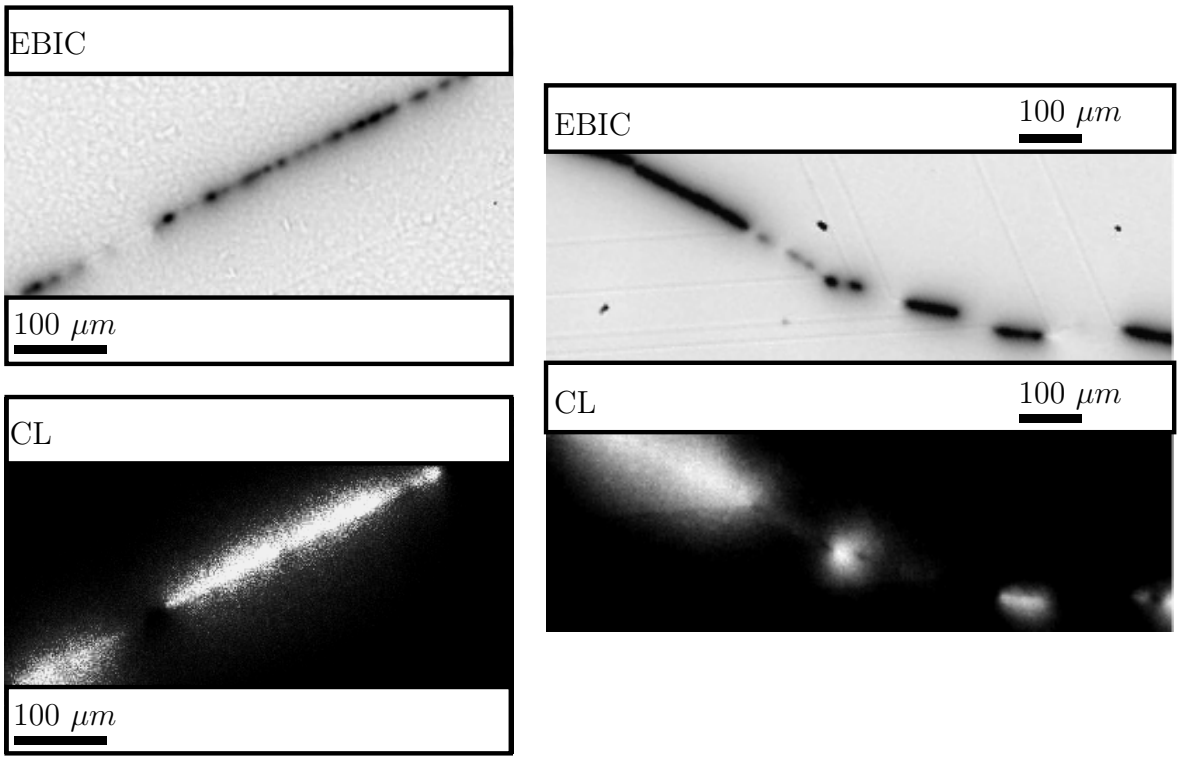

Figure 4.9: Correlation between EBIC micrographs and CL images at two different spots [45; 44].

Besides the spatial correlation, there could be also a correlation in the temperature dependence of the total recombination rate given by the EBIC contrast and the radiative recombination detected by CL. "The temperature dependence of the normalized EBIC contrast (EBIC contrast divided by the maximum contrast at low temperature) as well as the normalized CL intensity (Cl intensity divided by maximum CL intensity at low T) is given in Fig.4.7 (right). Both curve progressions are similar and indicate an increase of the total and the radiative recombination rates on decreasing temperature. The temperature dependence of the EBIC contrast [50; 52; 36] on dislocations and grain boundaries is determined by the degree of their contamination [50] and the crystallographic structure of the boundaries [52]" [44]. The EBIC contrast presents the total recombination rate at the defects. Applying the model to the EBIC results, assuming that the total recombination rate is proportional to the normalized contrast will

obtain similar activation energy as was estimated from the CL measurements [45].“The temperature dependences of EBIC and CL signals are related to thermally induced changes in the occupation of the Di level” [45].“Moreover, the radiative and the total recombination rates show similar temperature behavior and the sites of high radiative recombination coincide spatially with those of high total recombination. Therefore it is possible to suggest that the radiative processes prevail in the total recombination” [45].

To testify if this is true, an estimation of generated and collected carriers was performed. At a beam current of 50 nA with 30 keV acceleration voltage there will be a generation of $\approx 2.34 \times 10^{15}$ eh-pairs per second after equation 2.10. In contrast, only 2.5×10^5 per second counts will be registered at the detector. To compare the generated eh-pairs with the collected photons, it is necessary to calculate backward how much photons have to be emitted to realize the detected signal. Therefore, several loss processes have to be taken into account. Beginning with considering a quantum efficiency of $\approx 0.5\%$ at 1300 nm of the detector there should be $\approx 5 \times 10^9$ particle before the detector. Allowing for a further loss of $\approx 40\%$ due to passing the spectrometer at a slit width of 3 mm in comparison to a slit width of 10 mm, were almost all luminescence could pass, there should be $\approx 8.3 \times 10^9$ photons before the spectrometer. Finally, there is a loss due to the hole in the collecting mirror ($\approx 20\%$) and an unavoidable contamination of the mirror due to the not oil-free vacuum leads to approximately estimated $\approx 75\%$ signal reduction, caused by the complete mirror. That implies there should be $\approx 3.3 \times 10^{10}$ photons collected by the mirror. Eventually this shows that only a small fraction (less than 0.1%) of the excited carriers recombine radiative and thus still the non-radiative recombination prevails.

4.1.4 Estimation of the defect level position inside of the silicon band gap

As previously mentioned, the model 4.1 used for the estimation of the Di defect level does not provide any information if the defect level is located below the conduction or above the valence band. According to [83], there is a possibility to estimate the location of the defect level in the band gap of Si. Analyzing the peak energy as a function of temperature (Fig.4.8 *b)*) and correlate the slope with the temperature dependence of the band edge positions of conduction and valence band.

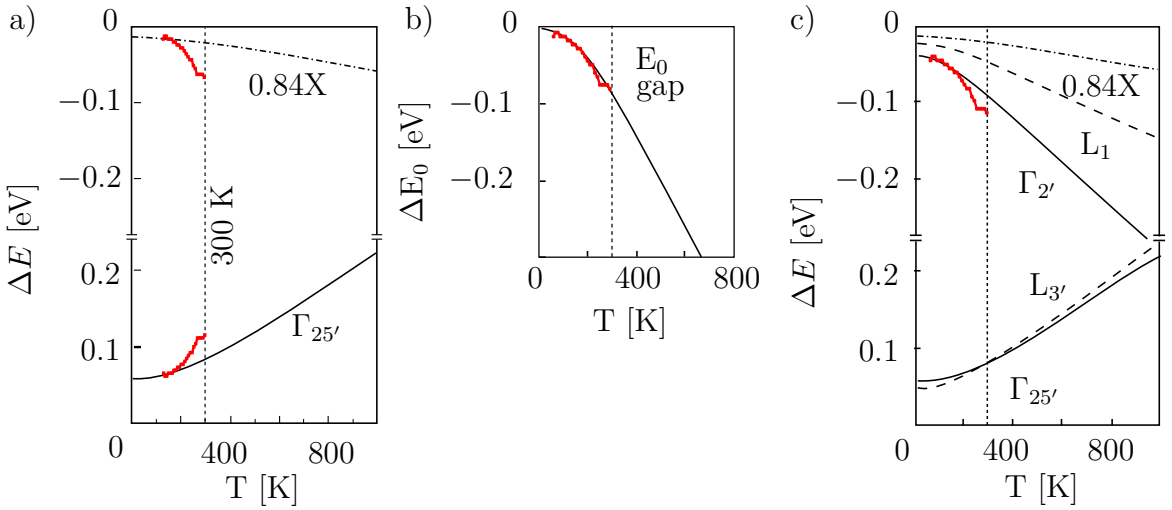

Figure 4.10: Temperature dependent shift of valence and conduction band at the indirect gap *a)*, of E_0 band gap *b)* and of states at the Γ, L and 0.84X points of Si *c)*, taken from simulations from [51] compared to the temperature-related shift of the Di luminescence peak.

A similar attempt shown in Fig.4.10 *a)* revealed that is not possible to evaluate the gathered data in the described way. Nevertheless, the peak energy shift of the Di luminescence could be almost correlated to the shift of the $\Gamma_{2'}$ band which is involved in the transition through the E_0 gap in Si (Fig.4.10 *b)* and *c)*). These direct E_0 gap is the second lowest gap in Si [51]. The comparison of the temperature dependent shift of the Di luminescence with that of the E_0 gap, also shown in Fig.4.10 *b)*, reveals a consistent agreement. The discrepancy between the measured data and the temperature dependent $\Gamma_{2'}$ band location (Fig.4.10 *c)*) could be explained with the existence of the expected second defect level which is possibly located next to the valence band. However, it is difficult to separate both defect levels and there different temperature dependences from the measured data. The attempt to estimate the location of the involved defect levels in Di luminescent recombination could not prove where the levels are located. At least it supports the suggested model (Fig.4.8 *a)*) in the manner that the position of one of defect levels below the conduction band and the other one closely above the valence band is probable.

4.1.5 Beam current and beam energy dependence of the Di luminescence

The luminescent recombination at these levels could be excited with remarkably small beam currents. This was for the first time obtained while conducting investigations during the already mentioned stay at the Electron- and Ion Microscopic Facility of Interdisciplinary Resource Center for Nanotechnology of Saint Petersburg State University (IRC-NT-Lab). One achieved result is shown in Fig.4.11.

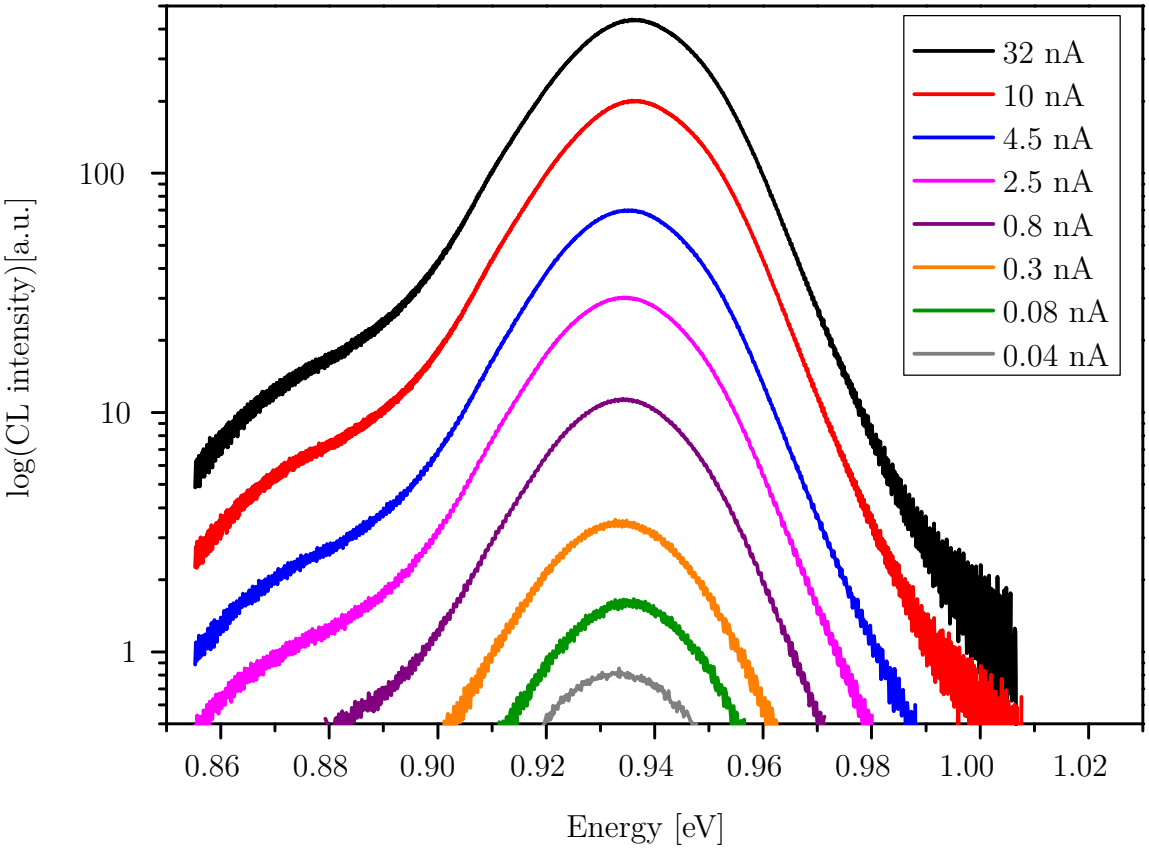

Figure 4.11: Beam current dependence from 40 pA to 32 nA of the Di luminescence at 80 K and 30 keV; measured during a stay at the IRC-NT-Lab St. Petersburg.

The following repeated measurements in Cottbus are presented in Fig.4.12 (inset). A detectable signal of Di radiation could be achieved even at beam currents below 10 pA, while typical values necessary for detection of BB luminescence are in the range of several 10 nA - 100 nA [52; 73].

The saturation effect observable in Fig.4.12 above 15 nA could be related to an occupation of the defect level. Also due to high injection condition, an increase of the non-radiative transitions is conceivable.

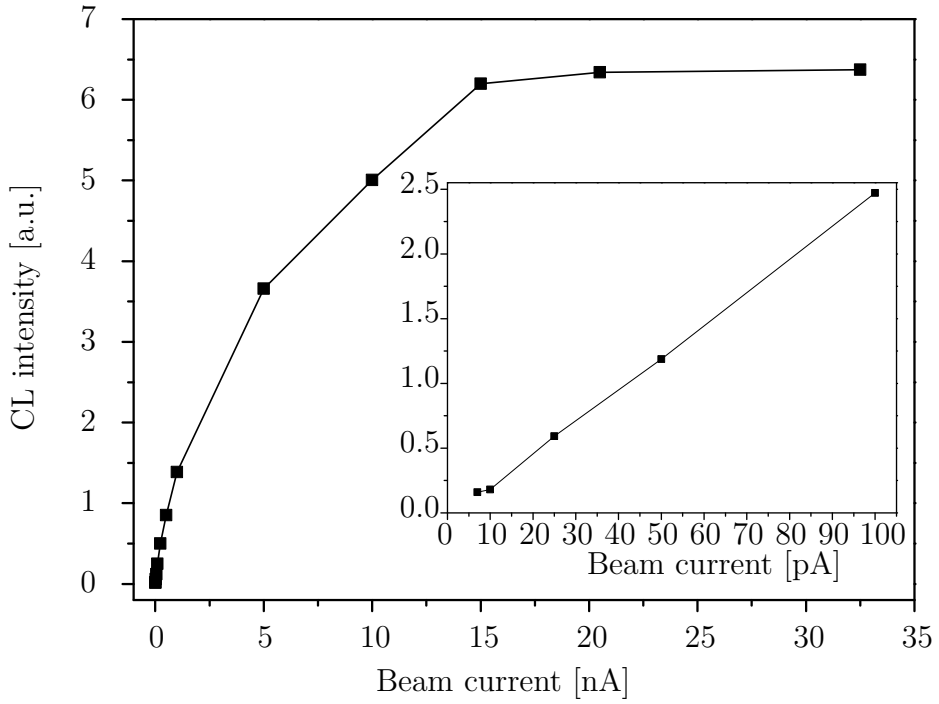

Figure 4.12: Beam current dependence of the Di luminescence at 80 K and 30 keV with saturation above 15 nA and luminescence with low injection condition from 0 up to 100 pA in the inset.

The energy dependence is shown in Fig.4.13, whereby an almost linear increase of the Di luminescence intensity is noticeable. According to equation 2.10, there is also a linear dependence between the beam energy and build eh-pairs in the material (Fig.4.13). However, the Di luminescence does not seem to be directly proportional to the eh-pairs generated. Since no saturation or decrease is observable, this could point to a structural defect in the Si material extending over the entire penetration range of the electron beam. The more defective material will be in or next to the eh-pair generation volume the more Di luminescence will be emitted.

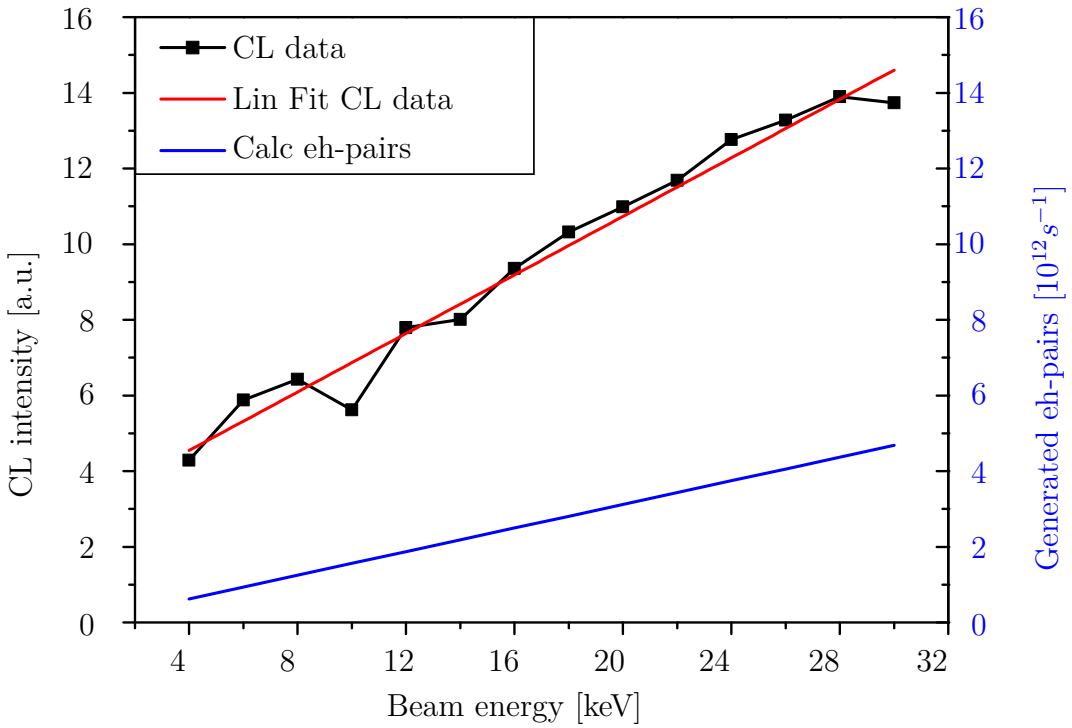

Figure 4.13: The beam energy dependence of the Di luminescence with a linear fit and the calculated eh-pair generation in dependence of the beam energy.

4.1.6 Structural investigations

The EBSD investigations were performed by H.-M. Krause to find the orientation of the grains forming the boundary where the Di luminescence appears and correlate its crystallographic structure with the Di emitting spots.

To correlate the appearance of the Di luminescence with structural and local electrical properties of the sample a region emitting Di luminescence was selected and additional EBSD was performed. “Figure 4.14 presents EBSD, EBIC and CL maps of such a region. A grain boundary running from top left to bottom right is visible in all three images. The monochromatic CL taken at the spectral position of Di reveals strong luminescence at certain sections of that boundary. The EBIC image in the middle reflects the local recombination activity of the boundary and shows a pattern similar to the CL image” [44].

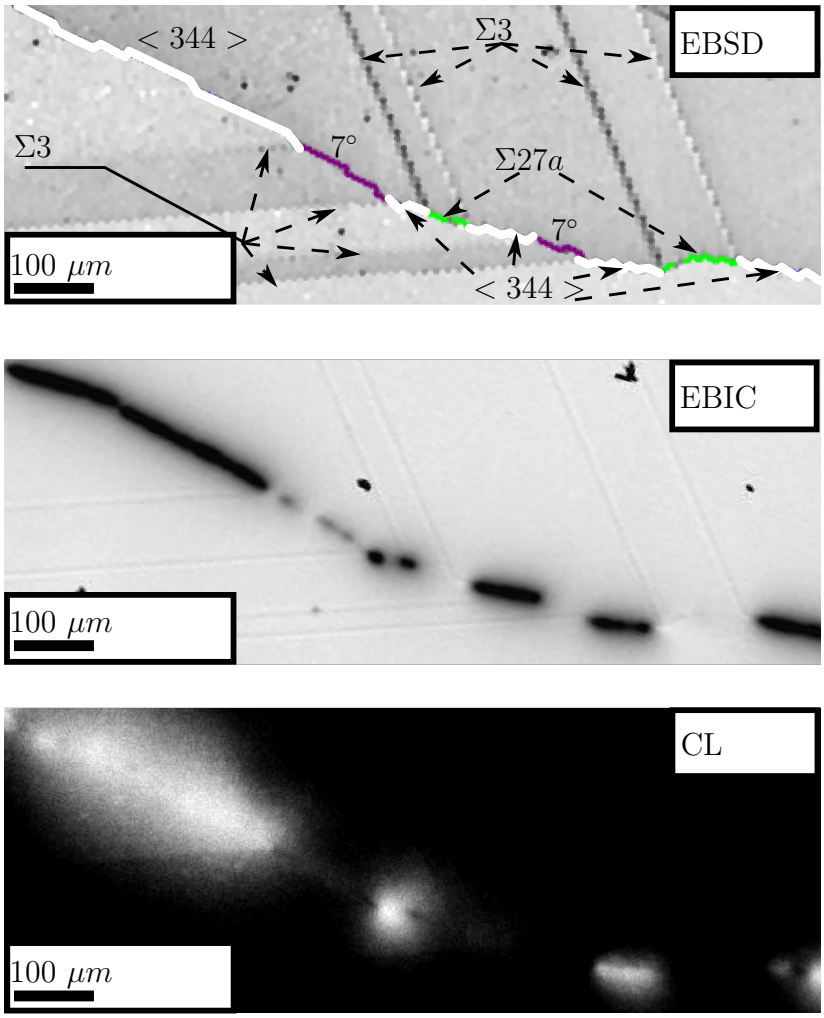

Figure 4.14: "Comparison between EBSD (top), EBIC (middle), and CL (bottom) maps. The < 344 > grain boundary (white) shows strong EBIC contrast and Di luminescence. The green marked segments in the EBSD image are identified as Σ27*a* and violet marked are small angle boundaries (7°)"[44].

"The EBSD image at the top shows all boundaries in the selected sample region and indicates their type. It is found that the boundary in question consists of segments of 3 types: (i) a boundary characterized by an about 60° rotation of the adjacent grains along a < 344 > axis (boundary labeled < 344 >), (ii) a small angle boundary (7°), and (iii) a Σ27*a* boundary. Only the < 344 > segments exhibit Di luminescence, while Di is not observed at 7° and Σ27*a* segments" [44]. A close up of another region is shown in Figure 4.15 to explain what is meant by < 344 > axis in more detail.

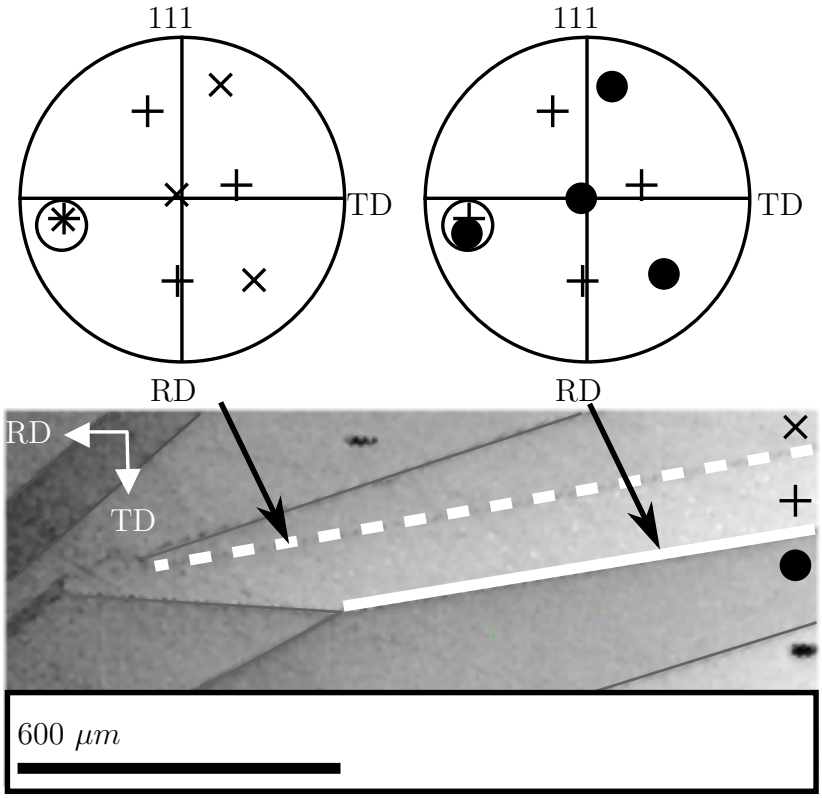

Figure 4.15: "Orientation of adjacent grains forming a dark grain boundary and a grain boundary emitting Di radiation as determined by EBSD analysis. To each of the grain boundaries a pole figure is given, showing the coinciding crystallographic directions for each of the crystallites"[45].

"The pole figures in Fig.4.15 present the orientation of the $< 111 >$ crystallographic directions on a stereographic projection. Each grain generates four marks corresponding to its four $< 111 >$ crystallographic directions. The overlap of the $< 111 >$ directions of two neighboring grains is shown in each of those pole figures. The different symbols indicate different grains. A coherent $\Sigma 3$ boundary presents a perfect overlap of the $< 111 >$ direction of both grains (left pole figure on Fig.4.15), whether a small misorientation produces two close to each other, but not overlapping marks (right pole figure on Fig.4.15). The distance between the marks at the closest $< 111 >$ position (marked with open circle) on the pole figure is a measure for the angle of misorientation between the crystallographic planes of the grains. The misorientation of the Di emitting boundary amounts 7 degree and is consistent with overlapping of one $< 344 >$ direction of both grains. The orientation of the boundary plane relatively to the crystallographic orientation of the grains should be considered as well. For a coherent $\Sigma 3$, the normal to the boundary plane coincides with both matching $< 111 >$ directions. Correspondingly, the boundary plane (and the dark line in the image) appears perpendicular to a

line connecting the center of the pole figure and the marks of both matching < 111 > directions on the pole figure. To facilitate the reading of the boundary orientation the image of the sample in Fig.4.15 is rotated by 90 degree. Thus the grain boundaries appear parallel to the line connecting the center of the pole figure and the mark of both matching < 111 > directions" [45]. It is supposed in Krause et al. [45] that the boundary, from where the luminescence seems to originate, is reconstructed, compensating the local misorientation by forming a uniform network of dislocations containing Frank partials. "Those dislocations surround areas of locally perfect Σ3 planes. The structure of those areas resembles the structure of <111> stacking faults. Therefore, the grain boundary could be regarded as a set of stacking faults in < 111 > plane closely aligned to one another" [45]. It is assumed in [44] that "a faceting of the < 344 > boundary plane occurs into a mixture of two lower energy boundary facets, one of which is < 111 >. Those < 111 > facets and the dislocation surrounding them resemble the structure of the stacking faults. Due to the misorientation, a dense local dislocation network is formed at the boundary. Those findings suggest that this dense dislocation network, containing Frank partials can be considered as origin of the strong 0.93 eV emission in mc-Si" [44].

To receive detailed structural information about the luminescent parts of the boundary, scanning transmission electron microscope (STEM) investigations were performed and analyzed by Dr. A. Hähnel at the the MPI of Microstructure Physics Halle. First a FIB lamella of the cross section at a certain luminescent and EBIC active part of the GB was prepared by H. Blumtritt, also at MPI Halle Fig.4.16 (left).

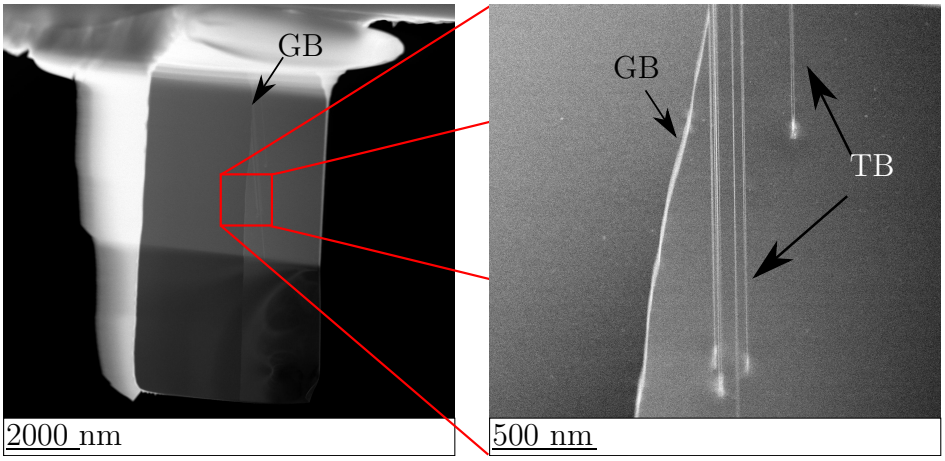

Figure 4.16: FIB lamella from preselected part at a luminescent GB (left), observable twins(mid) and dislocations along the boundary to compensate the misfit between the two grains, steps are projected by tilting approximately to the [121] orientation (right).

The left image of Fig.4.16 shows the prepared FIB lamella which was characterized in detail by STEM. As can be seen in Fig.4.16 (right), twin lamellae are grown from the grain boundary into the right grain. Further zooming in the grain boundary structure (Fig.4.17) demonstrates that there are closely neighbored dislocations located along the grain boundary.

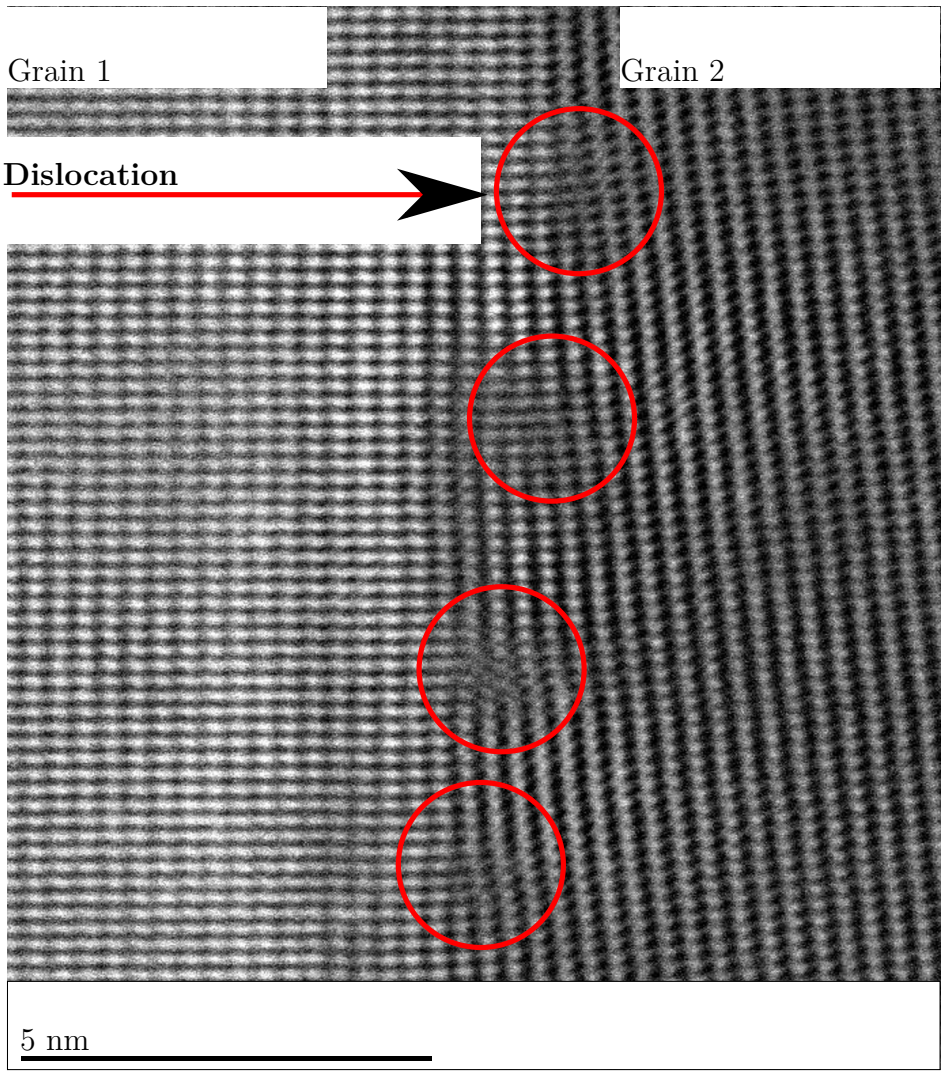

Figure 4.17: Dislocations along the boundary, shown in Fig.4.16, to compensate the misfit between the two grains, steps are projected by tilting approximately to the [121] orientation.

These dislocations compensate the small mistilt of $\approx 7 - 8°$ to the perfect twin orientation between the adjacent grains. That way a step-like interface is build up which differs from the known perfect $\Sigma 3\{111\}$ structure. By analyzing STEM annular dark field images it is possible to identify the type of dislocation in the GB.

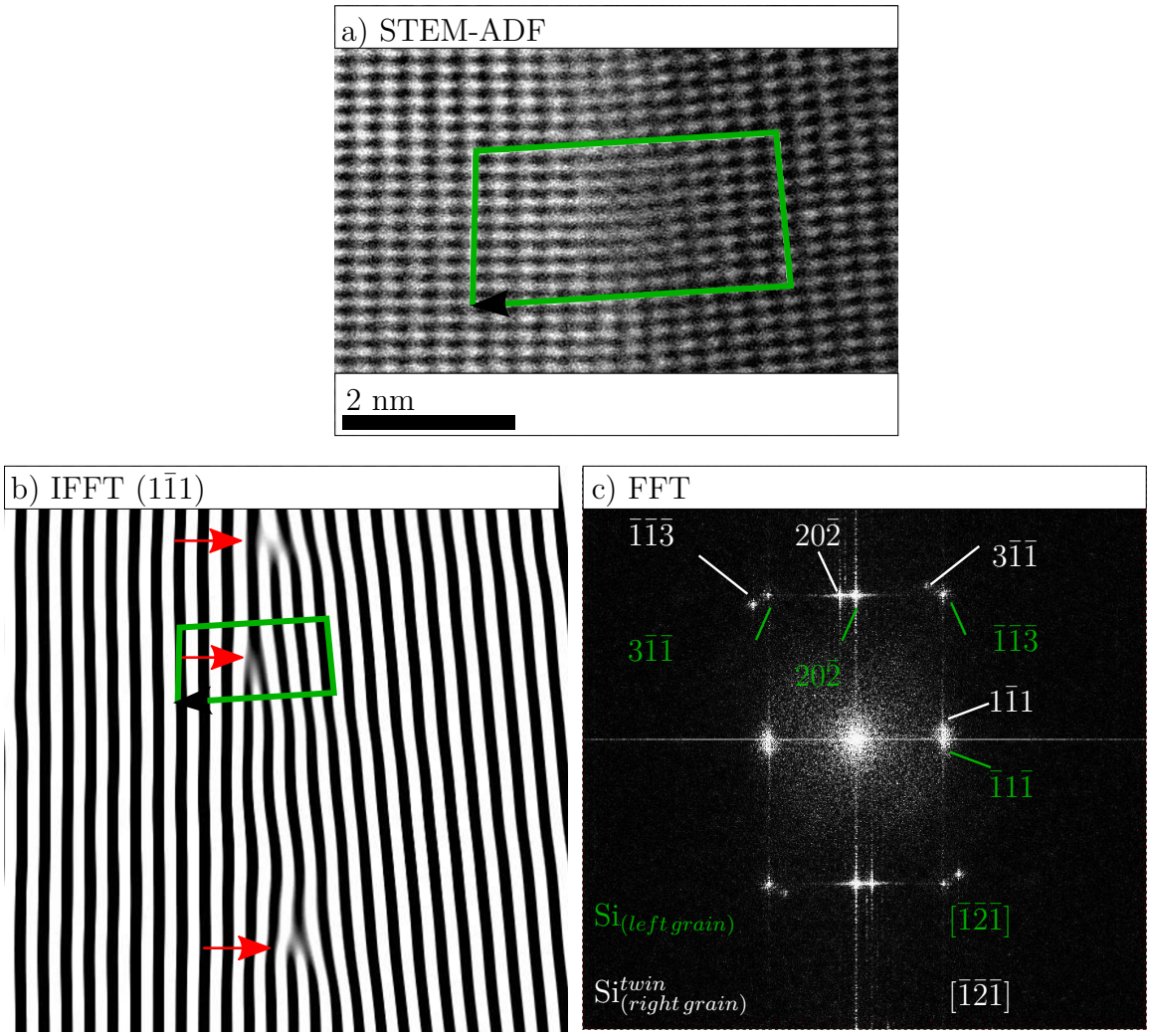

Figure 4.18: STEM-ADF analysis of the dislocation type: Image showing GB dislocations and a Burgers circuit *a)*, IFFT image calculated by selecting the (1$\bar{1}$1) reflection (from the right grain) as well as the ($\bar{1}$1$\bar{1}$) reflection (from the left grain) in the FFT *c)*. The Burgers circuit round the dislocation demonstrates the Burgers vector to be $\vec{b} = 1/3[1\bar{1}1]$, which corresponds to a Frank dislocation *b)*.

This is demonstrated in Fig.4.18, in which the top image is a highly resolved STEM-ADF image of a GB dislocation. It is possible to see that a single row of atoms split into two rows. In the inverse fast Fourier transform (IFFT) image, Fig.4.18 *b)* it is much easier to observe. The green marked Burgers circuit around a dislocation identifies the Frank-type of the dislocation by its Burgers vector which is $\vec{b} = \frac{1}{3}[1\bar{1}1]$. This is illustrated by the IFFT, which was calculated by selection of the (1$\bar{1}$1) reflection (from the right grain) as well as the ($\bar{1}$1$\bar{1}$) reflection (from the left grain) in the fast Fourier transform (FFT) of the STEM-ADF image Fig.4.18 *a)*. The Frank partial dislocations

with $\vec{b} = \frac{a}{3}[1\bar{1}1]$ are located in $[10\bar{1}]$ direction with a distance of ≈ 3 nm above each other. In addition, the FFT image Fig.4.18 *c)* shows the mistilt between the left and the right grain and the mirror plane being $(1\bar{1}1)$.

Figure 4.19 presents a zoom shot of the GB, which demonstrates the arrangement of extrinsic stacking faults in the GB. The extrinsic stacking faults are located parallel to the $(\bar{1}1\bar{1})$ plane and act as seeds of secondary twin lamellae with extended $\Sigma(\bar{1}1\bar{1})$ boundaries.

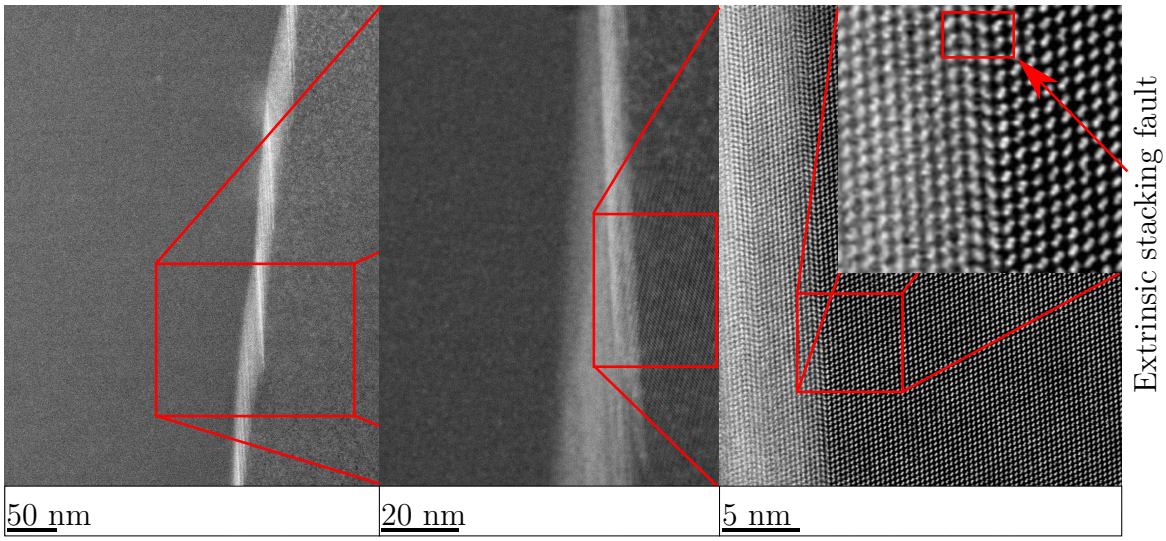

Figure 4.19: Zoom on the GB to show the extrinsic stacking faults.

Furthermore, the stacking faults are probably bordered by Frank partial dislocations. These findings strongly support the previously postulated hypothesis of the involvement of Frank partial dislocations as root-cause of Di luminescence. Unfortunately, it is difficult to prove whether Frank partials are the origin of the Di luminescence. It would be necessary to investigate specifically produced samples with $< 344 >$ GB which contains Frank partial dislocations. Only if Di luminescence could be observed there, the hypothesis could be proven in the last step. However, at locations where Di luminescence occurs, a high total recombination exists, and the GB segment could be identified to be $< 344 >$ oriented, Frank partials are located at this spot.

4.2 Summary

The intense 0.93 eV luminescence at room temperature observed with PL imaging originates from GB. This luminescence was named Di luminescence throughout the course of investigation. With high spatial PL mapping and CL it could be shown that the luminescence is emitted inhomogeneously along certain GBs. Analyzing the temperature dependence of the intensity indicates a defect level inside of the Si band gap 112±9 meV below the conduction band and also provides a second level 93 ± 10 meV above the valence band. Based upon this estimated defect levels a band model for the Di luminescent is suggested. The considered ascendance of radiative recombination could be denied through estimation of build eh-pairs in comparison to detected phonons. The ascertained temperature-related energy shift of the Di luminescence is almost similar to the change of the direct E_0 band gap of Si. Also it is shown that the temperature dependent position of the $\Gamma_{2'}$ band correlates about a certain distance with the shift of the Di luminescence. The mismatch at higher temperature is explainable with the second suggested defect level above the valence band. Furthermore, there is no correlation to the bands involved in the indirect band gap. Through beam current dependent measurements, it was possible to show that the luminescence could be excited with remarkably small beam currents even below 10 pA. Moreover, the Di intensity saturates above 15 nA. This indicates an occupation of the defect level or an increase of non-radiative recombination could also be possible. The beam energy dependent CL intensity results reveal a linear behavior, which could be interpreted in a way that there exist a structural defect area, which extends over the entire electron beam penetration range.

The orientation of the luminescent sections of the investigated GB is according to EBSD measurements identified to be $< 344 >$. The $< 344 >$ orientation indicates a small misorientation compared to the $< 111 >$ twin boundary orientation and the energy of the emitted luminescence is comparable with that reported in literature for Frank partial dislocations. Therefore, these dislocations, which are built to compensate the misorientation between two adjacent grains, are proposed as a first hypothesis for the origin of the Di luminescence. This suggestion was proved through TEM measurements. These show that Frank partials, bordering extrinsic stacking faults, could be found in the GB, at locations where Di luminescence appears.

5 Collection efficiency at twin boundaries - low temperature investigation

Our work group observed the first sign of the uncommon behavior of twin boundaries (TB) in 1996 [37] (Fig.5.1).

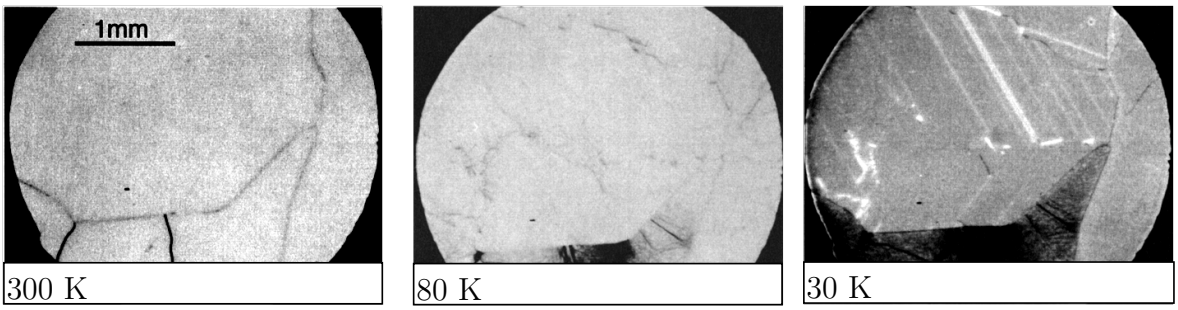

Figure 5.1: EBIC temperature dependence of collected current [37].

In the following section the bright contrast at the TB (Fig.5.1 right image) will be investigated in more detail with the aim to exhibit the behavior of TB at low temperature ($\approx 15 - 30$ K). Temperature dependent EBIC measurements will be used to determine which temperature is necessary to observe the enhanced collection efficiency. Using various electron beam currents should enable the opportunity to provide a statement to the carrier concentration dependence. In addition, current dependent measurements could provide information about conductivity differences between TB and grains. The electron beam acceleration voltage was altered to discuss the occurrence of the multi TB behavior at areas with several closely neighbored TB. The build-in potential of the diode could be estimated through measurements with applied bias in forward and reverse direction with beam on as well as with blanked beam. Furthermore, investigations with a narrowed ohmic back contact were performed, to show resistivity issues in the mc-Si sample at low temperature. To examine the extension width of the depletion region, capacitance-voltage measurements where performed by Dr. W. Seifert. EBIV investigations were realized to reveal alterations in the local resistance.

5.1 Experimental results and discussion

At first, a few words about what is actually observable during low temperature EBIC investigations. It is easily visible in Fig.5.1 that from 300 K to 70 K the TB are hardly recognizable, while below 30 K the EBIC current of the grains decrease (grains becomes darker) and the current of the twin boundaries remain at a higher level (bright at the images). For a better insight is a schematic drawing presented in Fig.5.2.

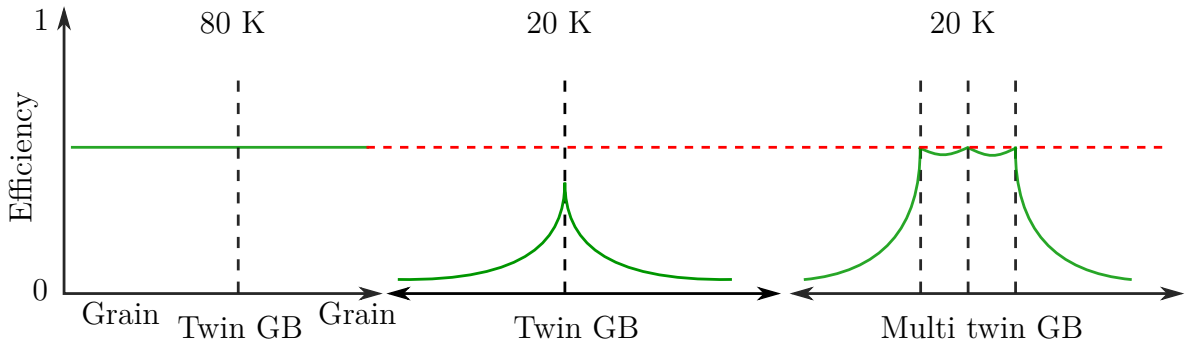

Figure 5.2: The schematic drawing of EBIC current properties through cooling.

The change of the efficiency during the cooling process is shown in Fig.5.2. On the left image, at 80 K there is no difference in efficiency between grains and the TB. On the middle image, at 20 K a clearly visible breakdown of the grain efficiency in contrast to just a slightly reduction at the twin location happens. Finally, on the right image, an overlap from several twin boundaries is observable, marked as multi twin GB, which leads to a high almost plain efficiency level along the twinning area. This behavior of single as well as multi twin boundaries will be explained and investigated in more detail in the following sections.

5.1.1 Estimation of critical temperature

For the estimation of the critical temperature, where the collection efficiency of the TB extends the efficiency of the grains, the sample was cooled down to 20 K and then stepwise slowly heated up. It is generally accepted that the defect density at the bottom of the ingot block is, due to the nearby crucible bottom, very high. Therefore, as suspected, the EBIC image 5.3 *a)* shows a high amount of defects already at room temperature (300 K). The strong recombination active GBs *A* and *B* reveal an additional bright getter zone at 80 K in image *b)*, whereas the TBs *(C, D, E)* just show a low activity. At further cooling down to 20 K *c)* the GB *B* vanish, GB *A* shows a low EBIC contrast, and the twins at *C, D, E* reveal an enhanced charge collection compared to the surrounding grains.

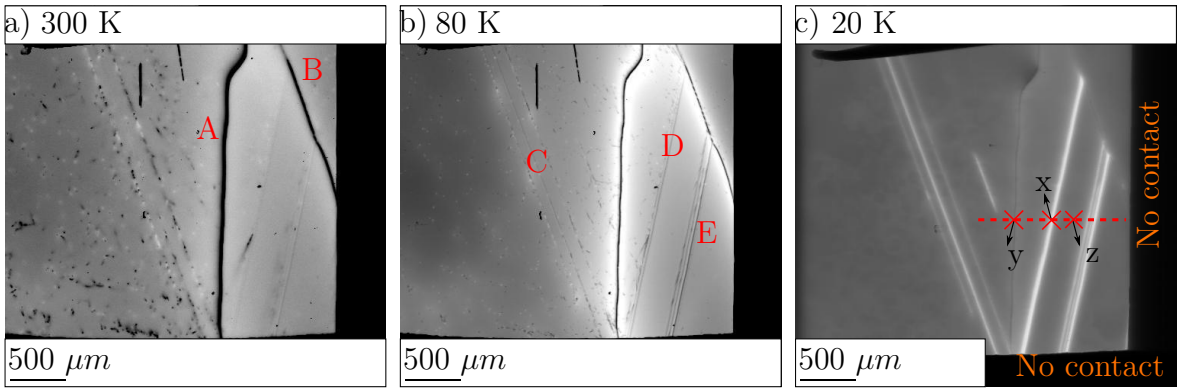

Figure 5.3: EBIC images with 30 keV 100 pA from a bottom-sample at different temperatures *a)* 300 K scale 0.8 to 1.0 *b)* 80 K scale 0.4 to 0.8 and *c)* 20 K scale 0 to 1.0.

Temperature-related efficiency measurements (according section 2.4.2 and equation 2.11) were performed to determine the temperature where the electrical behavior at the TBs begins to change (Fig.5.4). The first guess that the TBs act like conducting dislocation networks [34] could be ruled out. The conducting networks show EBIC current even in areas not covered with the Al front contact. In contrast, in Fig.5.3 *c)* a hard cut of the EBIC signal is found at the border of the contact, visible at the lower end of the image.

The EBIC profile was recorded along the dotted red line in Fig.5.3 *c)*. At the marked points x at the single TB, y at a random GB, and z at a plain grain the values were plotted in Fig.5.4 for 15 to 80 K. It is evident that the EBIC current of the random GB (blue) and the plain grain (black) starts to decrease at 30 K respectively at 25 K while the TB efficiency decline not until 23 K. In the inset the entire detectable temperature range from 15 to 300 K is shown. Beginning from 300 K down to $\sim$ 80 K (blue), respectively $\sim$ 50 K (green, black) a decrease of efficiencies is observable, followed by a strong ascent, ending at 30 K (blue), 25 K (black) and 23 K (green).

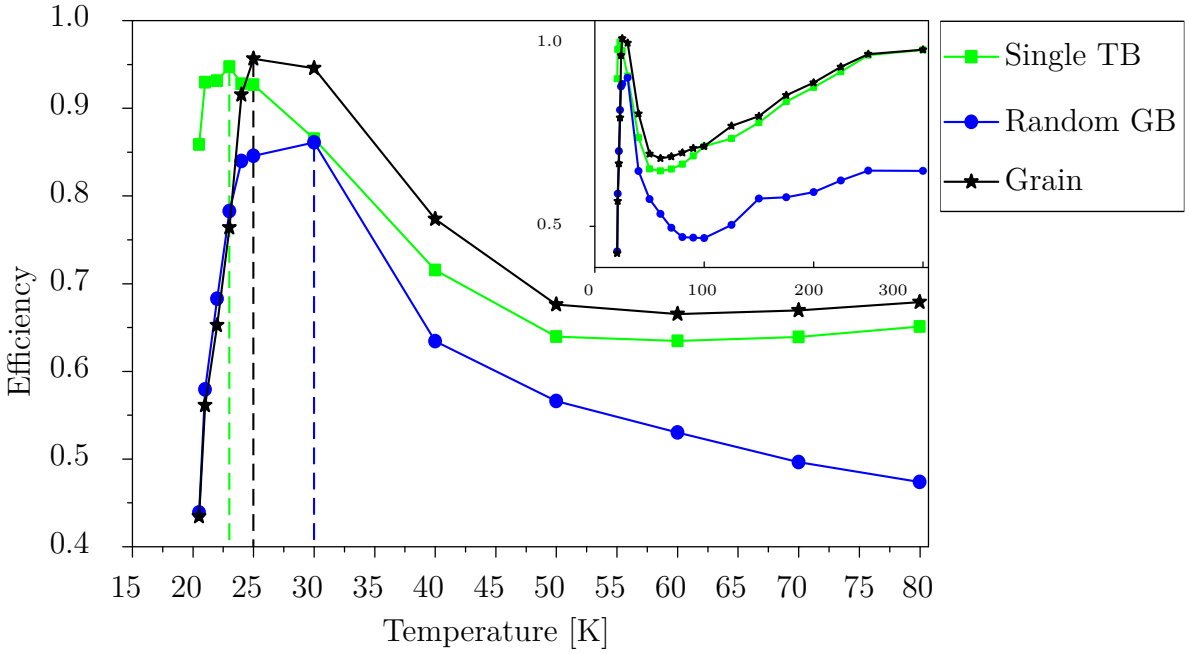

Figure 5.4: Temperature dependence of the collection efficiency from 15 to 80 K at a bottom sample (Fig.5.3) at a single TB (x), a random GB (y) and at a grain position (z) with 100 pA and 30 keV. Inset shows the temperature dependence from 15 to 300 K.

To verify that the uncommon electrical behavior below 30 K is not related to the degree of contamination, a sample from the same block was investigated next, albeit this time from the middle (Fig.5.5). At this block position, the influence of the crucible can be neglected. At image Fig.5.5 *a)* a common 80 K EBIC image is shown. In general, there was measured a high collection efficiency over the entire sample and several recombination active dislocations become visible. In the right corner, some TB can be observed, which become visible due to the chosen contrast scaling.

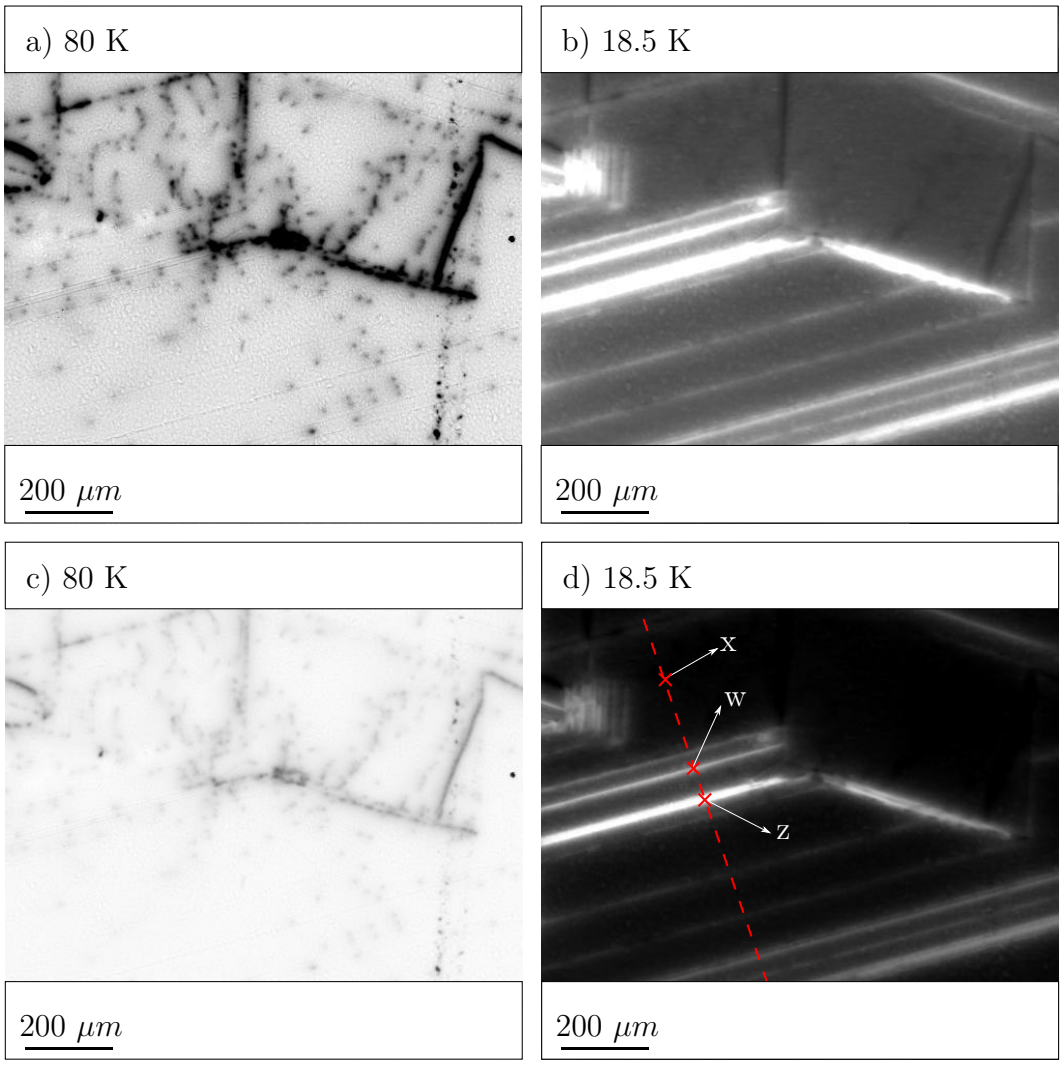

Figure 5.5: EBIC images with 30 keV 100 pA recorded at a sample taken from the middle of the block at different temperatures *a)* 80 K scale 0.8 to 0.95 *b)* 18.5 K scale 0.2 to 0.65, *c)* 80 K and *d)*18.5 K same scale 0.3 to 0.95 with marked measurement points: *x* grain, *w* single TB and *z* multi TB.

The scaling in*a)* and *b)* is chosen in a way that the most sample details are visible. In contrast, both images *c)* and *d)* are scaled similarly to enable comparing the contrast of both images. With same-scaled images, no evidence of TBs at image *c)* is noticeable.

The related measurements to the marked positions in Fig.5.5 *d)* are shown in Fig.5.6, whereby the position x is located at a grain, w at a single TB, and z at an intensive bright EBIC location where some TB are located close to each other (multi twins Fig.5.2). At position z, the efficiency shows no noticeable decline in the investigated temperature range, whereas the efficiency decrease at the grain starts at 24 K, followed by the TB efficiency at 22.5 K, which is comparable with the value from the block bottom Fig.5.4. To test if the measurement results are reproducible, investigations were repeated at two different positions at the same TB as in Figure 5.5 and at another single TB at the same sample.

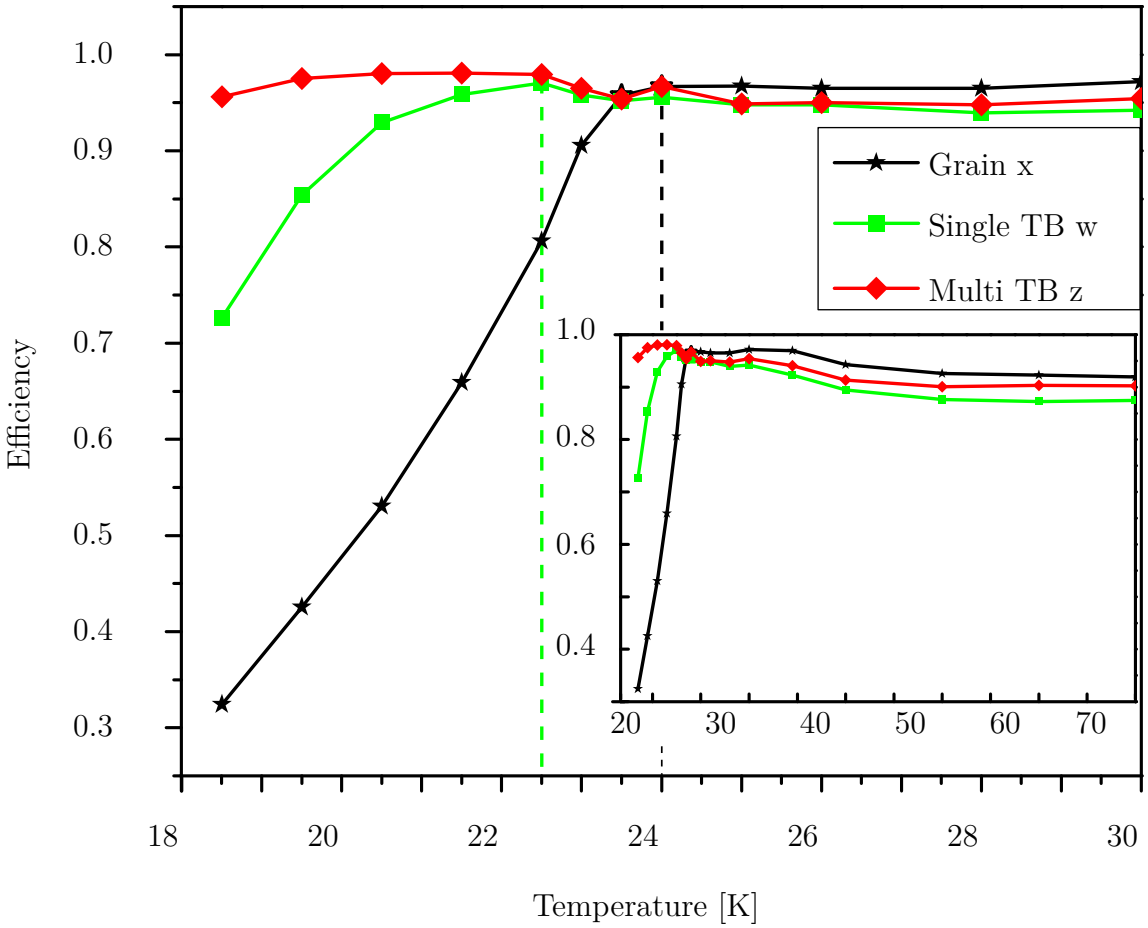

Figure 5.6: Temperature dependence of the collection efficiency from 18 to 30 K at a mid-sample (Fig.5.5) at a single TB (w), a multi TB (z) and a grain position (x) with 100 pA and 30 keV; Inset: 18 to 70 K.

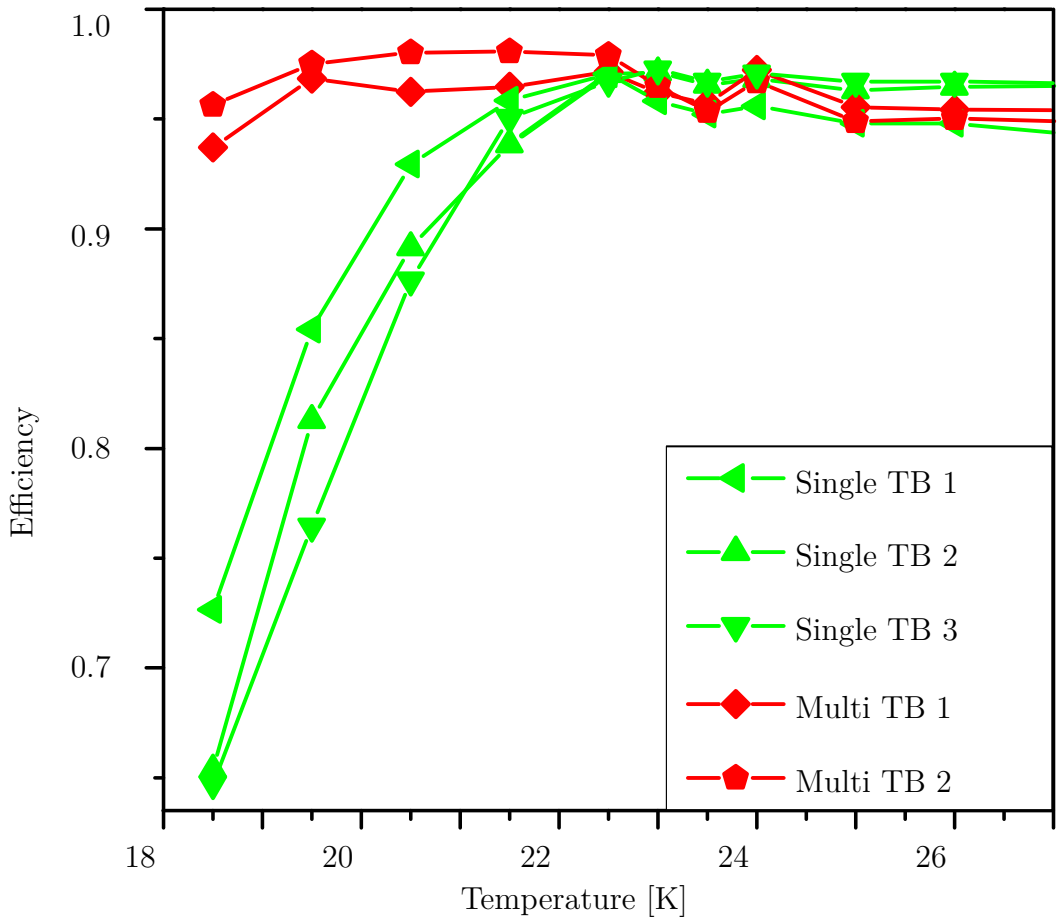

Figure 5.7: Temperature dependence of the collection efficiency from 18 to 27 K at two different points at the same single TB, one other TB and two different points at the same multi TB with 100 pA and 30 keV.

Fig.5.7 exhibits that at different measurement points similar behavior can be observed. Because it does not matter at which position of the TB the measurement was performed, the same investigations were also performed at samples from a different supplier to check if the observations are generally unrelated to a special selected kind of samples.

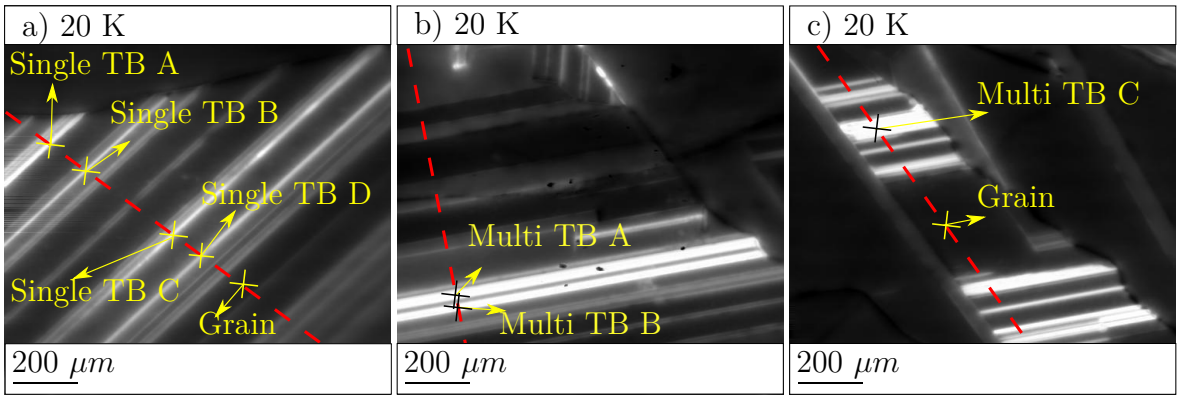

Figure 5.8: EBIC images with 30 keV 100 pA at a sample from the middle of the block at 20 K with marked measurement positions.

In Fig.5.8, the samples from the other supplier show at low temperature, 20 K, the same behavior as the previously measured ones. It seems that usually at TB location the collection efficiency remains at a higher level during cooling below 30 K.

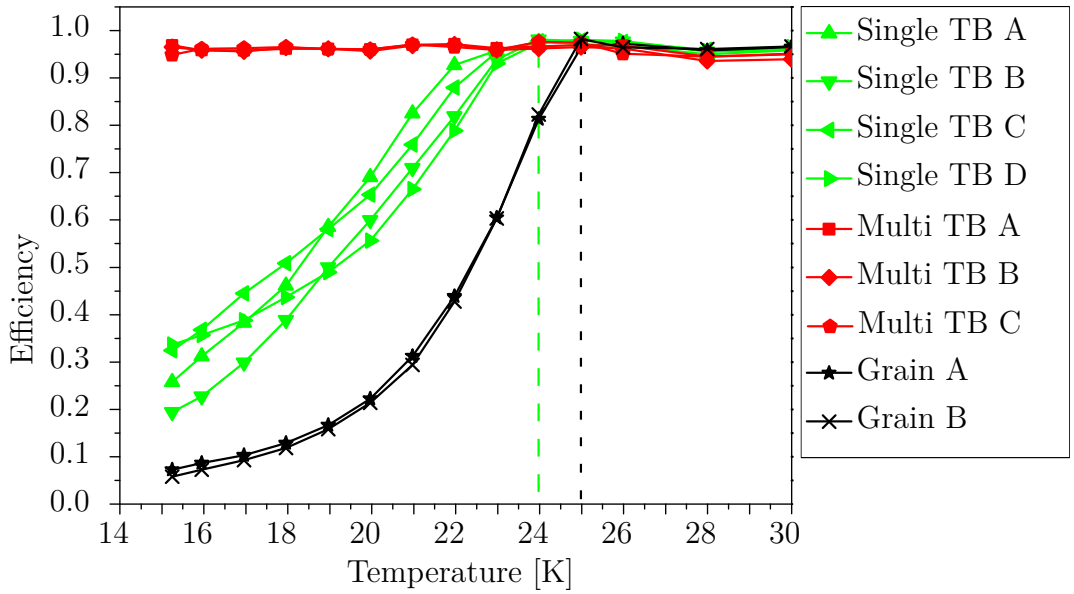

Figure 5.9: Temperature dependence of the collection efficiency from 15 to 30 K at different points at different single TB, different points at the multi TB and at different plain grains with 100 pA and 30 keV.

It is not important at which of the marked TB the measurements were performed, given that all of them show similar behavior (Fig.5.9). The single TBs as well as the multi TBs are comparable with each other and also with these measured at the first samples at block mid and block bottom.

A potential reason to explain the difference between the temperature where the grain efficiency starts to decrease and the slightly lower temperature at where the TB efficiency subsequently decreases could be a different "freeze out" temperature. Accordingly, Figure 5.10 schematically shows how it perhaps could be imagined. At the top is the standard EBIC setup shown at a temperature at which no difference between TBs and surrounding grains could be observed. In the middle, it is visualized what might happen through cooling down to 20 K. At first, the carriers in the grains freeze out while they remain alive in the TB. Therefore, the suggestion is that grains act more like semi-insulators than semiconductors and the semiconductor properties still dominate in the TBs. This would lead to an EBIC signal like drawn at the bottom of Fig.5.10 (left). A possibility to achieve the suggested difference in the "freeze out" temperature between grains and TB could be a local shrinkage of the Si band gap in the TB region, as shown in Fig.5.10 (right)

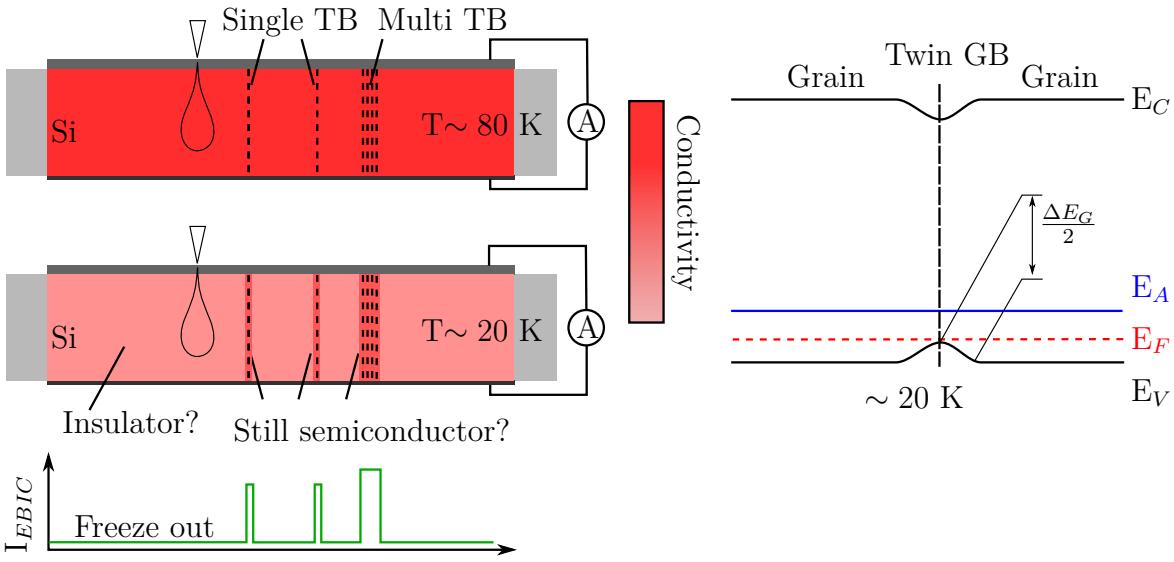

Figure 5.10: (left) Schematic drawing of the standard EBIC setup (top), hypothetical imagination of changes at low temperature (middle) and resulting conceivable EBIC-signal (bottom); (right) Schematic drawing of Si band gap shrinkage at TB at 20 K

To estimate the extent to which he band gap has to be shrunk, the carrier concentration at a given temperature was calculated and subsequently compared with the concentration at a 2 K lower temperature. It was revealed that a ~ 4 meV decrease of the band gap would be sufficient to achieve the same carrier concentration as calculated for a 2 K lower temperature, but without lowering the temperature. A band gap shrinkage of only 4 meV would end in a 2 K lower "freeze out" temperature. It is shown in Figure 5.10 (right) in simplified terms.

It is known that stress influences the band structure of Si [11]. An increase of the band gap can be produced with compressive strain, wich would reduce the lattice distance. This would result in a higher "freeze out" temperature in the strained material. Otherwise, if we induce tensile strain the lattice distance would be increased and the band gap energy will be decreased, which leads to a lower freeze out temperature. Moreover, it is common to use stress in the production process of microelectronic devices. Aimed induced strain could influence the carrier mobility and other silicon properties. Devices could be designed in the desired way [89; 57]. Möller [66] reported a reason for stress in TB. He investigated Edge-defined film-fed growth (EFG) silicon and reveals carbon monolayers inside of the TB. Caused by the EFG production process there is a real high amount of carbon inside the material. Carbon inside TB leads to a reduced lattice constant which is similar to comprehensive stress and results in an increase of the band gap energy. However, an increase of the lattice distance can also be found in TB.

That twins are able to induce stress is shown through TEM measurements and following geometric phase analysis (GPA) of TEM/ HRTEM images through investigation of (111) reflex in Fast Fourier transform (FFT) at the University Göttingen by P. Schwager at electron beam crystallized thin-film Si on glass substrate (Figure 5.11). Also large strain at multi TB regions where reported by Chen et al. [12] investigating mc-Si samples.

Another conceivable reason for the electrical behavior, besides the already discussed discrepancy in the "freeze out" temperature, could be a change in the depletion area during the cooling. An increased SCR width results in a decreased electrical field, which leads to a decreased carrier separation and a lower collected current. If there is a difference between the SCR at areas with TB and at spots without, it should be visible through a CV-measurement. A different SCR width should be shown as a different capacitance behavior because of the difference in the influenced capacitor width. A schematic setup is drawn in Fig.5.12. The resulted data are plotted in Fig.5.12 (right) and they reveal a slower decrease of the capacitance at regions with a high amount of TB than at the region without TB. Unfortunately, it could be the case that there was a measurement problem affecting the collected data. It could be possible that the serial resistivity was changed due to the cooling process. This also could lead to results like those observed. Up to now, this parasitic influence could not be ruled out. Therefore, the obtained CV-data could be adulterated and the measurement should be repeated.

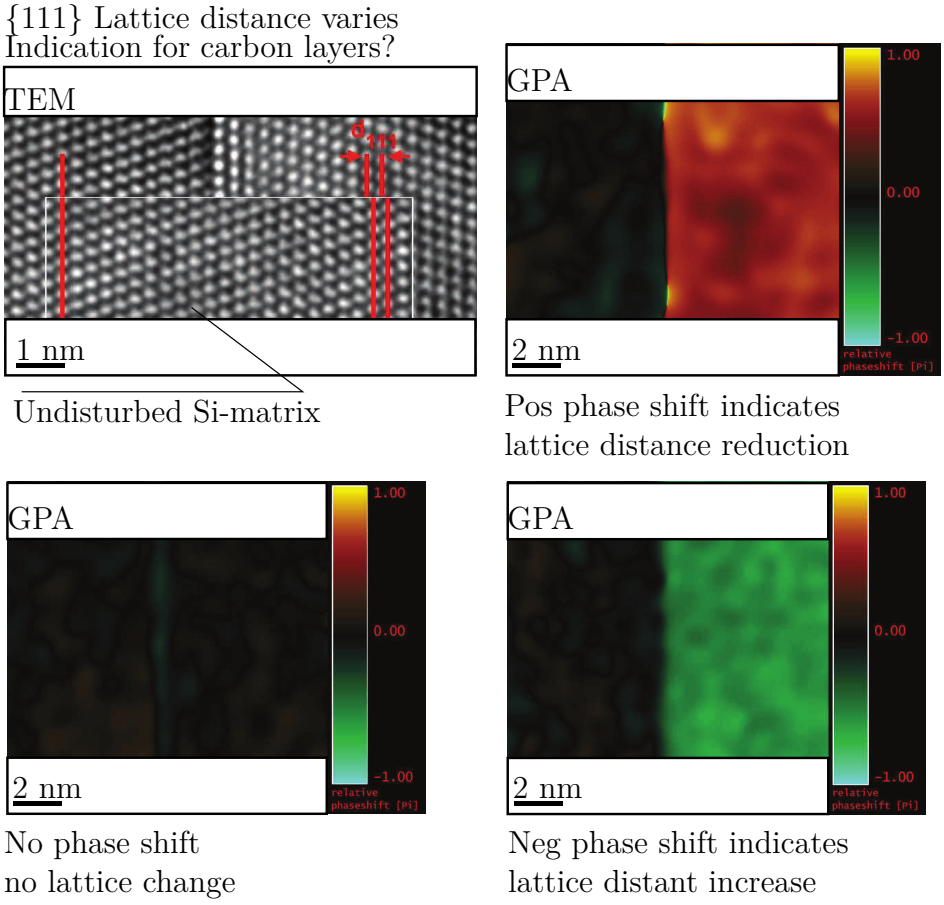

Figure 5.11: TEM thin film Si on Glass: undisturbed Si lattice compared to disturbed once (top left); Geometric phase analysis (GPA): stress induced reduction of lattice constant (top right), no lattice variation (bottom left) and stress induced increase of lattice constant (bottom right) (P. Schwager, Uni Göttingen)

However, the formula to calculate the SCR width do not show any direct temperature dependence. Therefore, it is suggested that the properties of the SCR could have simply an additional side influence at the TB behavior.

Another additional side influence could emerge through carrier freeze out in grains surrounding TB while they remain alive in them. This enables the build of a potential barrier at the TB. Through the barrier, a local SCR is built, which enhanced the local field strength. Because of the local higher field strength, an increase of the collection efficiency at the TB seems possible. A schematic drawing of how it might be imaginable is shown in Fig.5.13 (left).

Besides the mentioned strain, defect states in the band gap could as well cause a local band gap shrinkage. In section 2.4.2 it is already pointed out that there is a tentative

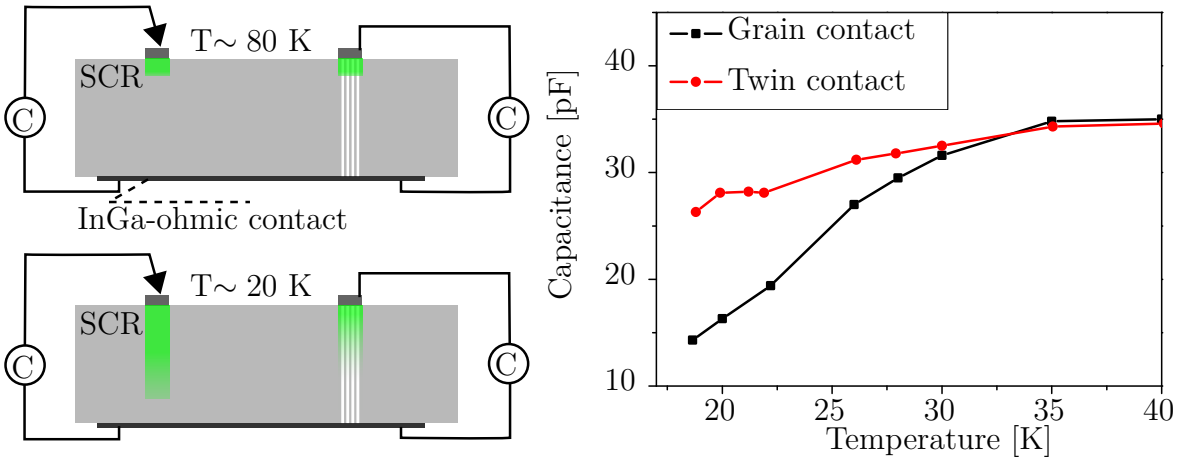

Figure 5.12: Schematic setup of CV-measurements at different 80 K (top) and at ≈ 20 K (bottom), capacitance decrease during p-EFG sample cooling at contacts with twins and without them with −0.1 V (right).

classification of defects, which is attributed to the contrast behavior of the defect. In Fig.5.13 (right) is the EBIC contrast profile of one of the single TB presented. The general curve shape looks like the contrast-temperature relation from group 1 defects (Fig.2.24) which are attributed to deep states in the band gap. These deep defect levels localized at the TB could act like a band gap shrinkage and cause a difference in the "freeze-out" temperature between grains and TB.

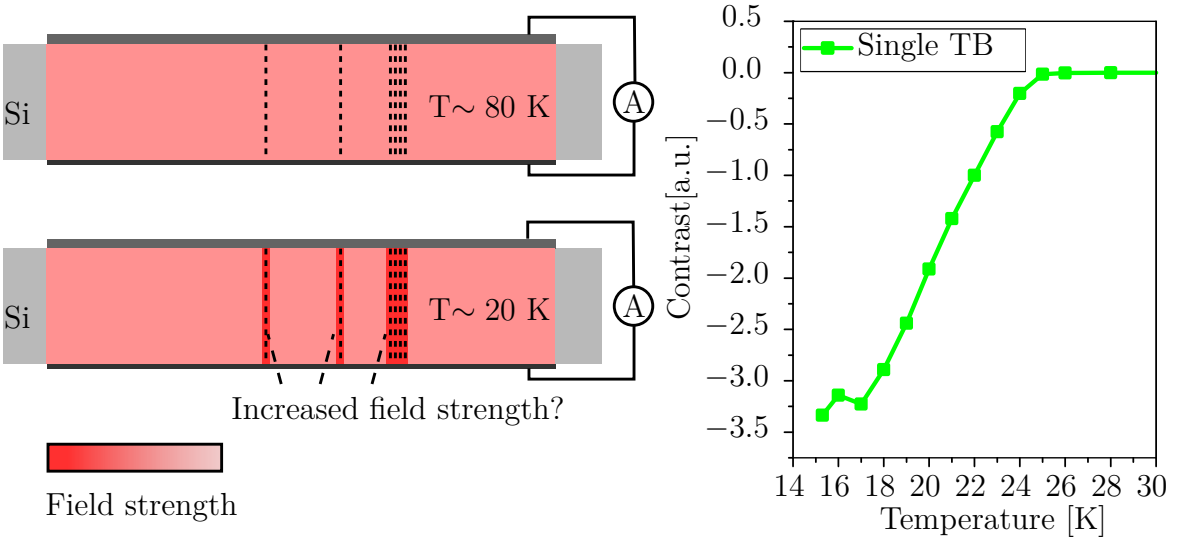

Figure 5.13: Schematic change of local SCR and field strength(left). EBIC TB contrast from 15 to 30 K (right).

However, if we consider the current dependence, like at the temperature-related measurements in Fig.5.13 (right), the contrast behavior is plotted in Figure 5.14. It is difficult to associate the measurement results to one of the suggested defect groups. The right image at 30 K could be attributed to group 1 like the temperature dependence in Fig.5.13 (right). In contrast, the run of the 15 K curve, on the left, above 100 pA rather looks like the group 2 drawing in Fig.2.24. Below 100 pA no clear behavior could be identified. It is also possible that there exist some kind of mix type defects, also reported by Kittler et al. [38]. In general, it is doubtful to use this kind of classification in this case. The investigated defects in [38] always shows a dark contrast (positive) which indicates a recombination center somewhere but in this case there only exist bright contrasts (negative) and according to the EBIC measurements there is also no indication of any recombination center at the TB.

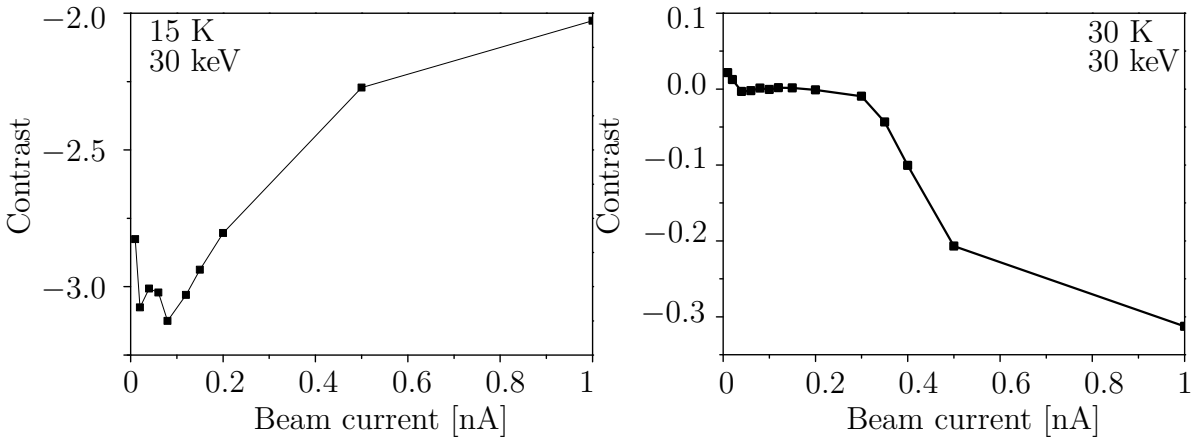

Figure 5.14: Beam current dependence of the EBIC contrast at 15 K and 30 K, 30 keV.

That the electrical behavior from the TB is not related to the doping type could be proved by investigations at n-type Si (Fig.5.15 *a)*) which show similar results like the measurements at p-type Si. Furthermore, investigations at EFG-Si were performed which also show the same features at the closely neighbored twins (Fig.5.15 *b)*). Indeed, at the EFG samples the characteristic seems enhanced, possibly caused by the high concentration of twins. In contrast, a repetition of measurements at EFG samples reveal no changes of the EBIC efficiency at all. No sign of "freeze-out" was to observe. The efficiency of grains and twin boundaries remain at a high level over the entire investigated temperature range. This could possibly be explained with the close density of the TB and thus the multi TB behavior could be valid over a broad sample area. The effect, special observed at multi TB, will be discussed in the following sections. In addition, the EFG samples could contain a high amount of carbon impurities. It is, up to now, not possible to estimate the influence of these impurities to the low temperature behavior. Furthermore, it should be mentioned that the EFG material, related to the production process, is different compared to block cast mc-Si, and could thus hold other properties. Finally, the reliability of the EFG results seem questionable.

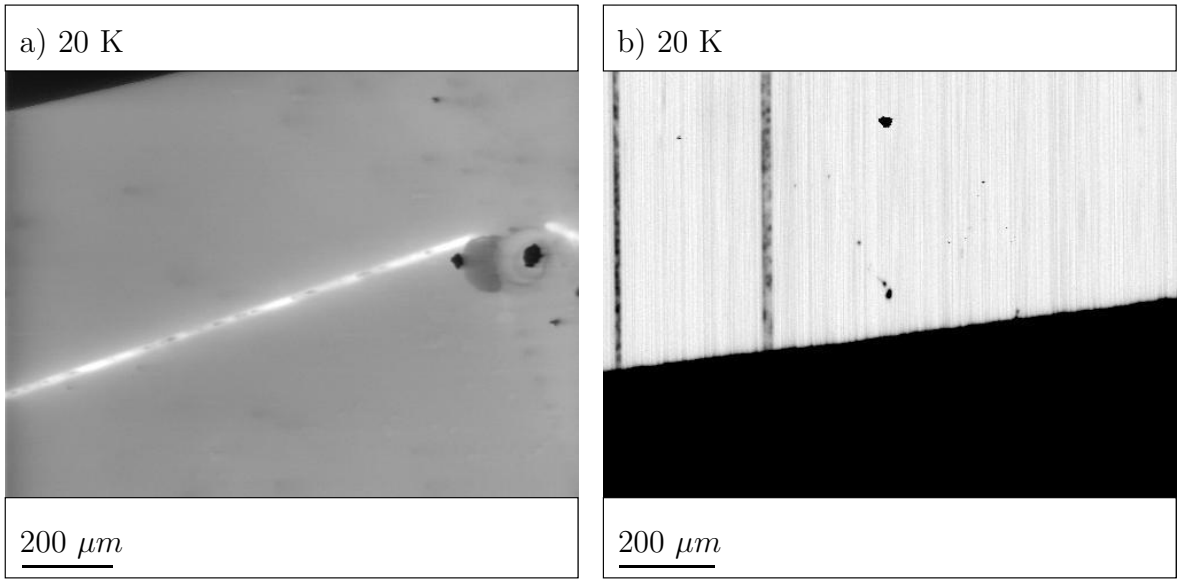

Figure 5.15: EBIC images 30 keV 100 pA: *a)* n-type Si sample at 20 K and *b)* p-type EFG also at 20 K.

5.1.2 Influence of excess carrier concentration

Due to the similarity of the results at samples from both suppliers, the focus in the following will be at the presentation of measurements from the last discussed mc-Si samples from the second supplier (Fig.5.8). Changes in the measurement setup were performed, like mounting a thermal shield around the sample and cutting of the helium jack, which enables working at lower temperature. These lower and more stable temperature conditions during the measurements are an additional reason to remain focused on the last investigated samples from now onwards.

Through comparison between the current dependent efficiency at 30 K and 15 K (Fig.5.16), a change in the behavior becomes evident. Before the curve declines, the efficiency measured at 30 K at the grain remains above 0.9 until 300 pA, respectively 500 pA for single and multi TB. The TB curves and the grain curve are bifurcate after 300 pA, which indicates a similar change in the collection efficiency like before at $22 - 23$ K and 100 pA, as described before in section 5.1.1 and also shown in Fig.5.17. Even at 34 K, it is possible to provoke the enhanced collection at the TB with ~ 2200 pA.

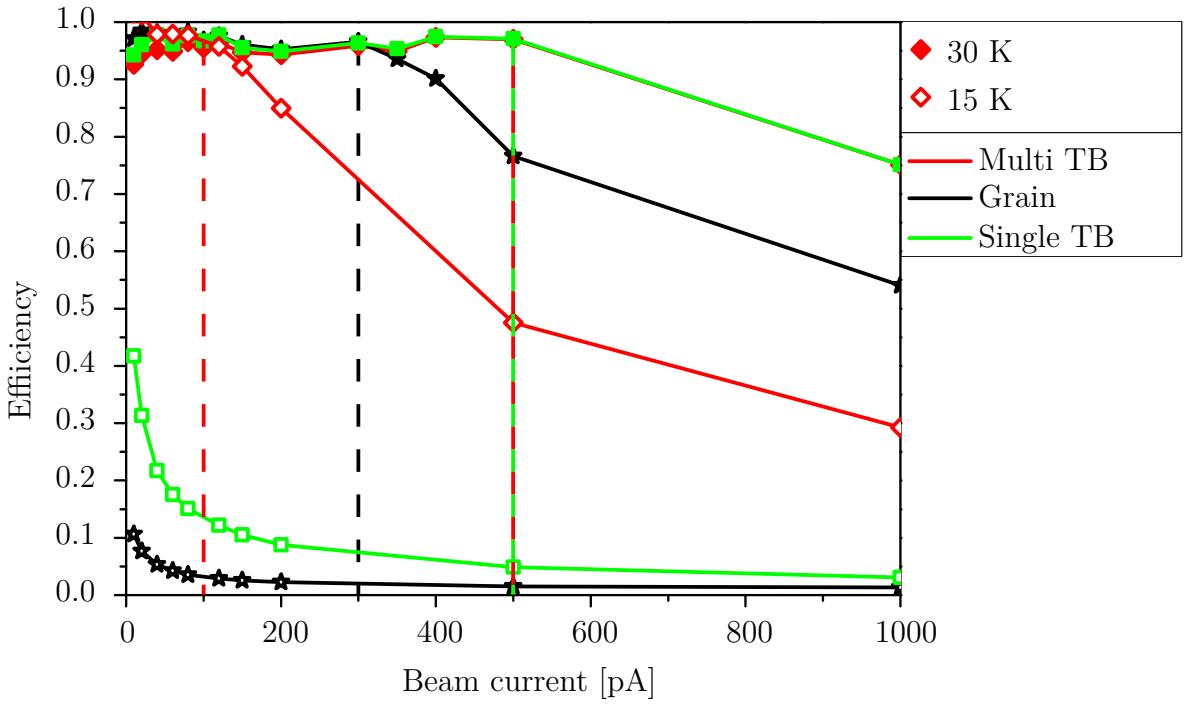

Figure 5.16: Beam current dependence of the collection efficiency from 0 to 1 nA at the same measurement points at 15 K (open symbols) compared to 30 K (filled symbols) at 30 keV.

This behavior could may be explained with eventuate high injection conditions at 30 K. Hence, it is necessary to examine the carrier concentration in the material through doping in comparison with generated eh-pairs by electron beam. The investigated silicon should have a resistivity of $0.7 - 1.1$ Ωcm which indicates a doping concentration of $\sim 2.2\times10^{16}-1.3\times10^{16}$ cm^{-3}. With an effective hole concentration at 30 K in the valence band of about 3.6×10^{17} cm^{-3} and therefore, with equation 2.3, the hole concentration should be decreased to about $1.5 \times 10^{13} - 1.15 \times 10^{13}$ cm^{-3}. The generated eh-pairs at $300-500$ pA are estimated with equation 2.10 to $\sim 1.4\times10^{13}-2.3\times10^{13}$ cm^{-3}. Hence, it can be supposed that low injection conditions are no longer valid and high injection influences might have to be taken into account. One consequence of high injection could be an enhanced recombination. Thus, on the assumption that at TB are less recombination centers located than in the grains it is conceivable that the collection efficiency at the grains declines at increasing beam current while at TB still more carriers could be collected. However, a strong influence regarding enhanced recombination seems improbable, because for enhanced Auger recombination, which could be increased due to high injection, although the complete carrier density should be too low. SRH recombination, which is the main recombination part in silicon, is under high injection conditions independent of doping, trap energy, and injection level. If taking into account

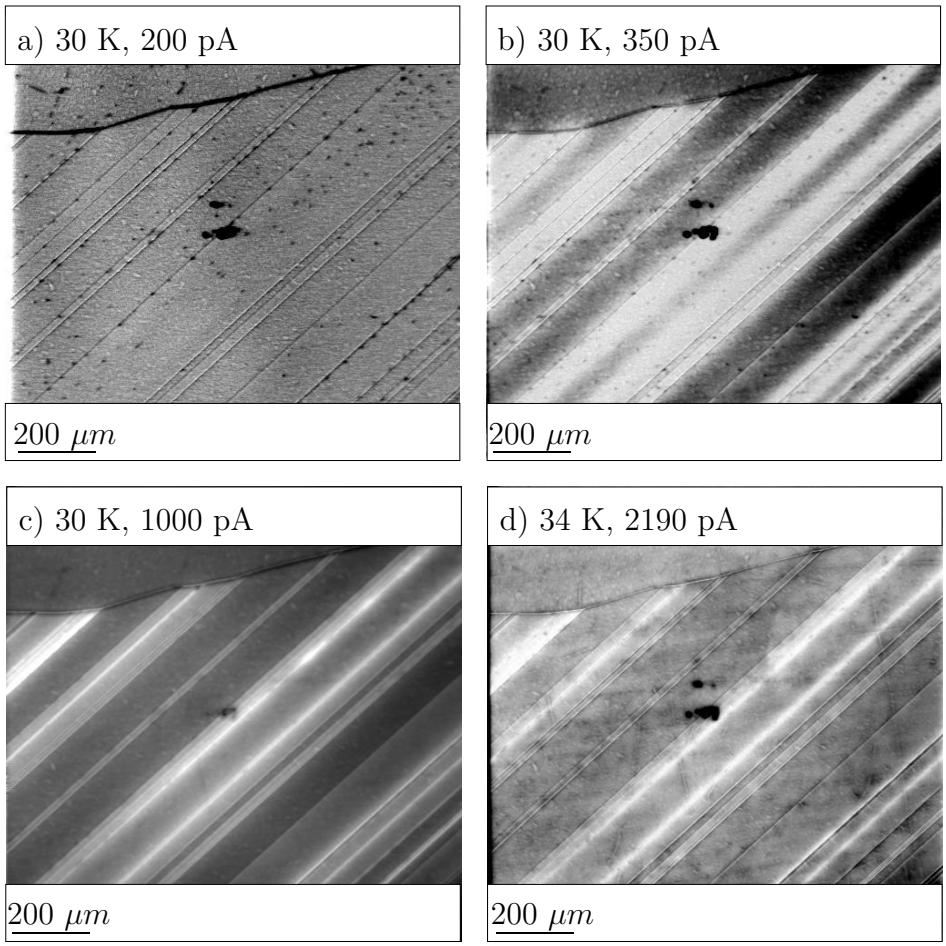

Figure 5.17: Beam current dependence of the collection efficiency at 30 K *a)* 200 pA scale: $0.94 - 0.96$, *b)* 350 pA scale: $0.9 - 0.96$, *c)* 1000 pA scale: $0.44 - 0.75$ and *d)* at 34 K with 2190 pA scale: $0.17 - 0.19$.

that the recombination contrast in the grains increases with decreasing temperature respectively with increasing injection level enhanced SRH recombination appears unlikely. To validate or exclude high injection effects or even clarify the influence, further detailed investigations remain necessary. Another also imaginable approach is that the changing efficiency at increased beam current could indicates an alteration of the serial resistance. A higher current needs a higher conductivity to be collected. If there is a conductivity difference between TB and grain regions and the introduced current will be exceeds a certain value the amount of collected current would also show a difference. The result could be the investigated enhanced collection efficiency shown in Fig.5.17.

To show how the material resistance influences the charge collection, a small sized ohmic back contact was placed at some TB, instead of covering the entire sample.

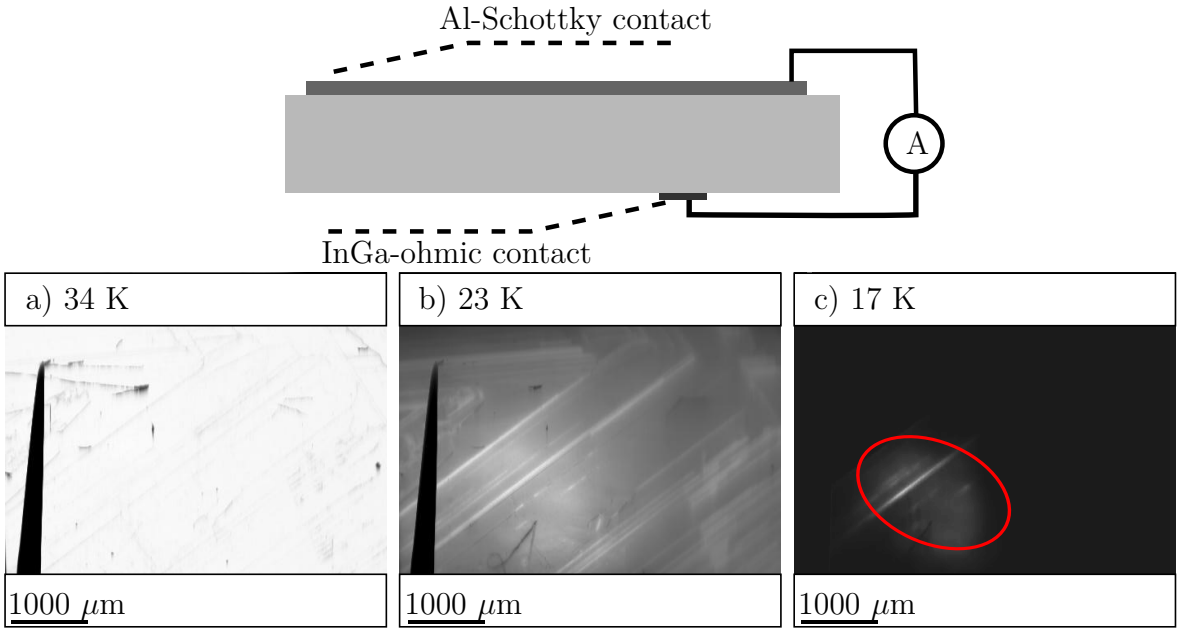

Figure 5.18: EBIC setup with just a small ohmic back contact (top); EBIC images at *a)* 34 K, *b)* 23 K and *c)* 17 K (bottom).

The schematic setup is shown at the top of Fig.5.18. At 34 K an EBIC signal can be measured all over the Al contact. Through cooling the sample slowly down it is noticeable in Fig.5.19 (right) that the size of the area where charge collection could be detected decreases. At 17 K, the collection area is almost narrowed to the size of the backside ohmic contact, marked red in the inset of Fig.5.18 *c)*. Due to the high resistance the amount of separated charged carriers, which are able to reach the ohmic contact, is strongly decreased. Only carriers generated next to the contact could be collected. This is schematic shown in Fig.5.19 (left).

The noticeable contrast between the curves in Fig.5.20 and partly in Fig.5.16 could possibly be explained with the size of the eh-pair generation volume. A lower beam acceleration voltage induces a smaller carrier generation volume with a smaller penetration depth in the material. Therefore, the curve shape in Fig.5.20 could also be explained. There is the comparison between the current dependence at 10 keV and 30 keV at 15 K presented. At 10 keV, the generation volume is smaller and thus leads to a higher carrier concentration next to the front contact. This could be a reason why the 10 keV curves from the grain and the single TB are situated above there 30 keV curves. The multi TB exhibit a different behavior. The 30 keV curve is located above the 10 keV data.

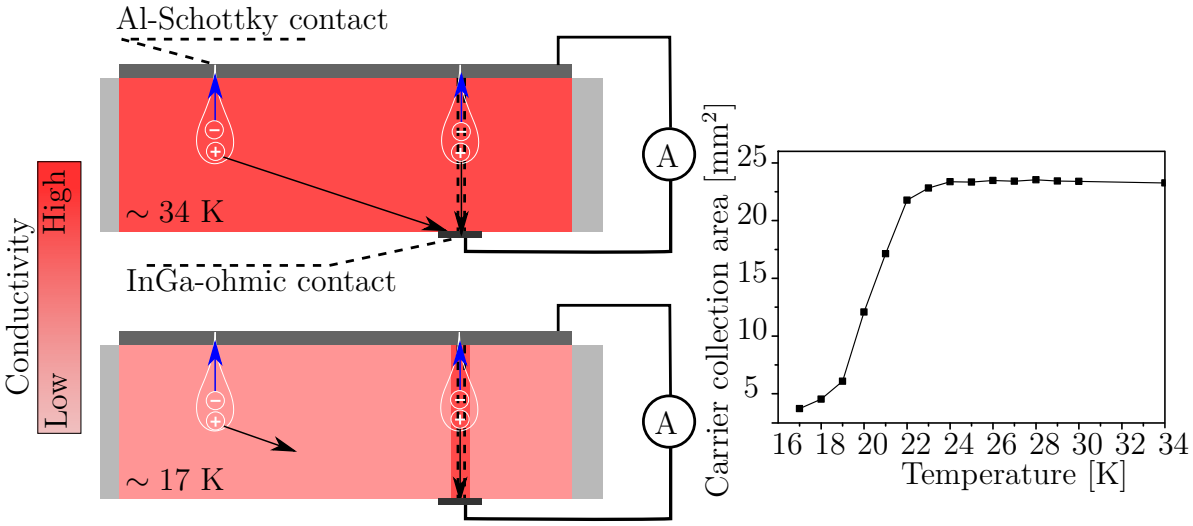

Figure 5.19: (left) Carrier separation with just a small ohmic back contact at 34 K top and at 17 K bottom. Size of the temperature dependent EBIC collection area (right), 100 pA and 30 keV.

The multi TB structure has a larger width than the single TB. The generation volume does not extend the size of the multi TB so much at 30 keV and thus at increased carrier concentration still more carriers can be collected at the position of the multi twins. At the single TB at 30 keV the size of the generation volume could extend the width of the TB and more carriers will be generated next to the TB structure instead of inside them. These generated carriers might not be counted to the EBIC signal. This possibly explains why more carriers were collected at the multi TB than at the single TB (Fig.5.16 (15 K) and Fig.5.20).

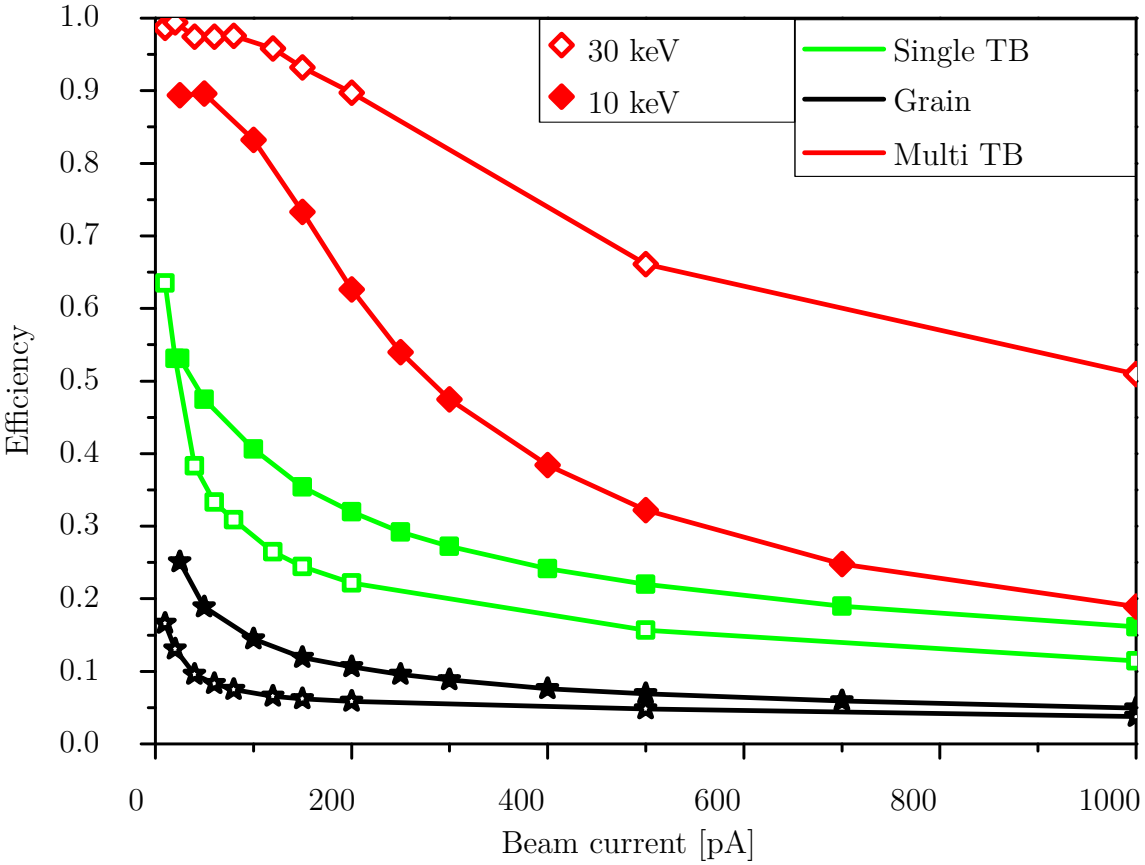

Figure 5.20: Beam current dependence of the collection efficiency from 0 to 1 nA at the same measurement points at 15 K and 30 keV (open symbols) in comparison with 10 keV (filled symbols).

5.1.3 Multi TB behavior

To investigate the influence of the penetration depth and thus the size of the generation volume at the collected EBIC current, beam energy dependent measurements were performed. Again, like in section 5.1.2, the same measurement points (Fig.5.8) were used. Additionally, in Fig.5.21 (left), there is a plot of a dataset collected at 30 K in comparison to 15 K, which shows the difference in the electrical behavior at very low temperature below 30 K.

It is evident that the three curves from the grain, single and multi TB at 30 K superpose each other and display an expected behavior for beam energy dependent EBIC measurements. The efficiency rises with increasing beam energy. With rising beam energy the penetration depth as well as the generation volume expands thus leading to a higher amount of generated eh-pairs as well as a higher collection current. At 15 K, another manner can be observed, whereby the efficiency at the grain measurement point

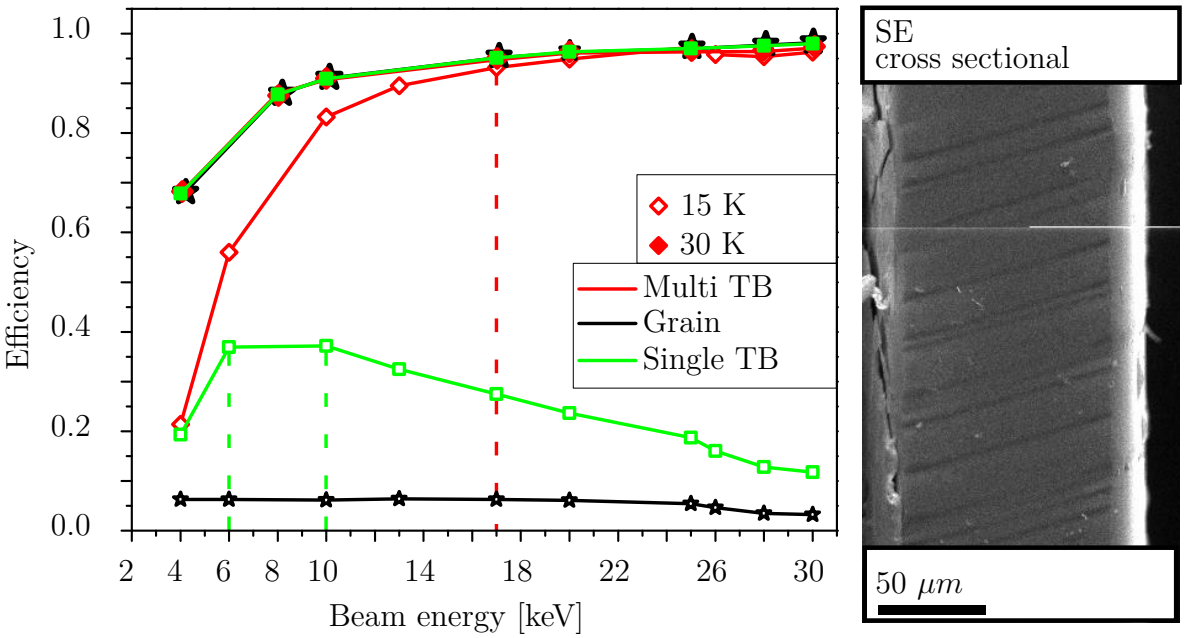

Figure 5.21: Beam energy dependence of the collection efficiency from 4 to 30 keV at 15 K (open symbols) and 30 K (filled symbols) (left). Cross sectional SE TB image (right).

runs almost straight below 0.1. The single TB exhibit a maximum above 0.35 between 6 and 10 keV where the generation volume is located closer to the front contact, has a smaller size and due to that contains a higher concentration of carriers. This could be an explanation for the maximum collection. After 10 keV, the curve goes down below 0.25 at 30 keV. The excess carrier concentration is decreased and the generation volume extends about 6 to 8 μm into the sample. Furthermore, the volume of the generation area extends the width of the TB as mentioned in section 5.1.2. This is shown in Fig.5.22.

Therefore, more eh-pairs will be created in a larger distance to the TB. Thus, a lower amount of carriers can be collected. At the multi TB, a different curve shape is revealed. Starting at the same efficiency like the single TB at 4 keV, the carrier collection ascends over the entire energy range until reaching 30 keV. As explained in section 5.1.2 and shown in Fig.5.22 the width of the multi TB structure is larger than that of the single TB. Thus, more of the generated eh-pairs will be collected in the area of the TB. Already at 17 keV the run of the curve follows the behavior of the efficiency at 30 K. Also cross sectional measurements (Fig.5.21 (right)) reveal that the TBs are not run perpendicular to the sample surface but rather they run obliquely. Therefore, the TBs area in the EBIC images as well as the current profiles (Fig.5.2 (left)) seem wider than they actually are. Even if the electron beam passed the TB at the surface, the generation

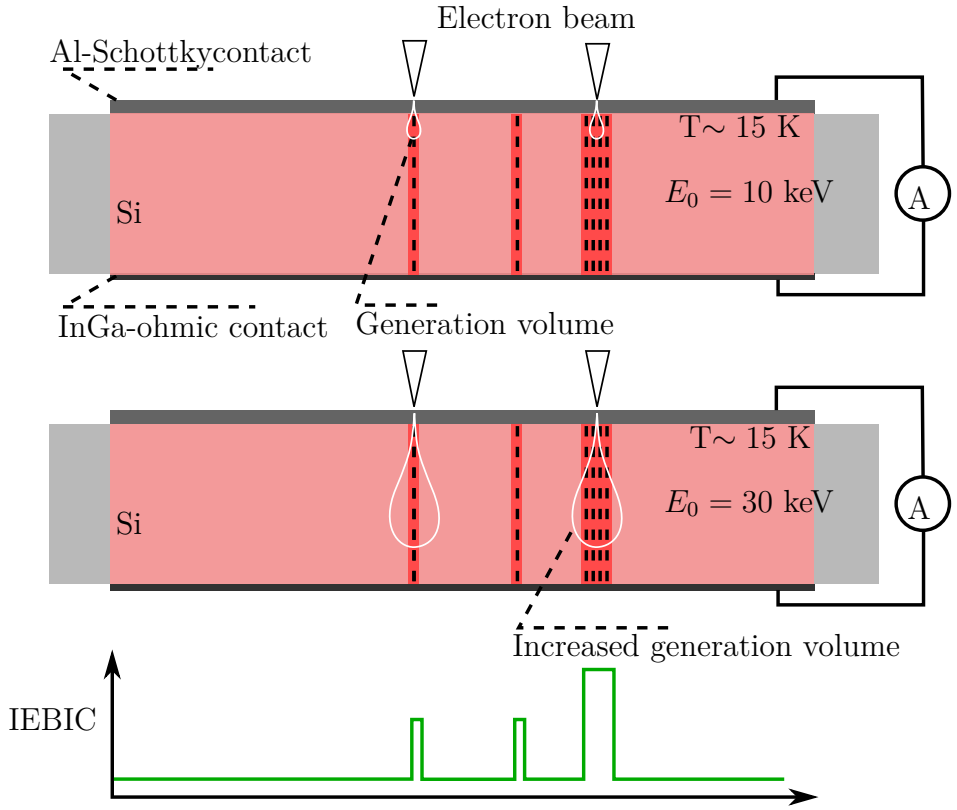

Figure 5.22: Schematic beam energy dependence of the generation volume width for 10 keV and 30 keV at 15 K.

volume still strikes the TB structure below the sample surface. Another reason to explain the multi twin boundary behavior as well as the TB efficiency increase during beam current dependent measurements, which should be taken into consideration, is the increase of generated current in both measurement cases. The amount of generated carriers is related to the beam current as well as to the beam energy. Thus, a certain higher generated current in the sample could lead to a breakdown of the diode barrier at the grain position, which consequently results in a lower collection of carriers at the front contact. It is suggested that there exists a higher barrier at the TBs, which still provides the necessary electric field for the carrier separation. This thought will be taken up again in the next section.

5.1.4 Estimation of build-in potential

Through EBIC measurements with applied bias on the sample, it is possible to estimate the build-in potential. In Fig.5.23 (left), the significant difference between the black grain curve and the colored curves of single and multi TB is clearly observable. From

−2.5 to 0.2 V the grain curve reveals ohmic properties while the single and multi TB curves show the characteristic line of illuminated solar cells. The efficiency of the single TB starts to decrease right after forward bias at the sample was applied, saturates from 0.8 to 1.2 V at ∼ 0.12, and break down at 1.5 V to almost 0. The multi TB efficiency begins to decrease a little after the single TB at 0.2 V. This could possibly indicate a difference between the field strength in single and multi TB.

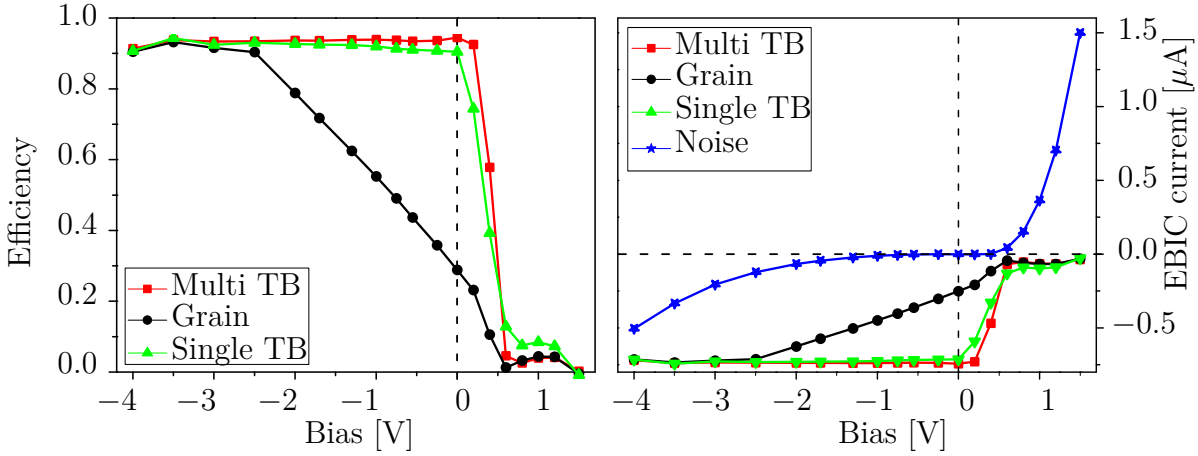

Figure 5.23: EBIC efficiency from 4 V reverse bias to 1.5 V forward bias at 15 K(left). EBIC current versus bias voltage with noise current at blanked electron beam (right).

More probable seems again the explanation through the width of the generation volume and the size of the multi TB structure, as previously mentioned in section 5.1.2 and 5.1.3. The multi TB efficiency declines to ~ 0.9 and saturates from 0.6 to 1.2 V before the final break down to almost 0. These results lead to an estimated build in voltage between 0.6 and 0.8 V at the TBs where the efficiency is decreased about $\sim 90\%$. In contrast at the grain the potential barrier seems lower. It is shown in 5.23 (left) that the grain efficiency starts to decrease already at -2.5 V, while the TBs efficiencies remain at a high level. Thus could indicate a lower potential barrier at the grain than at the TBs. Also the previously shown current dependence in Fig.5.16, where the grain efficiency decrease at 15 K starts 200 pA before the TBs efficiencies, could support the conjecture of a barrier difference between TBs and grains.

In addition to the EBIC measurements, EBIV was performed. Therefore, another amplifier was used with a high input impedance. Thus, current independent voltage measurements should be able to perform. EBIV micrographs (Fig.5.24 (right)) should show the differences in the resistance without the influence of additional serial resistances which may could influence the EBIC current investigations (Fig.5.24 (left).

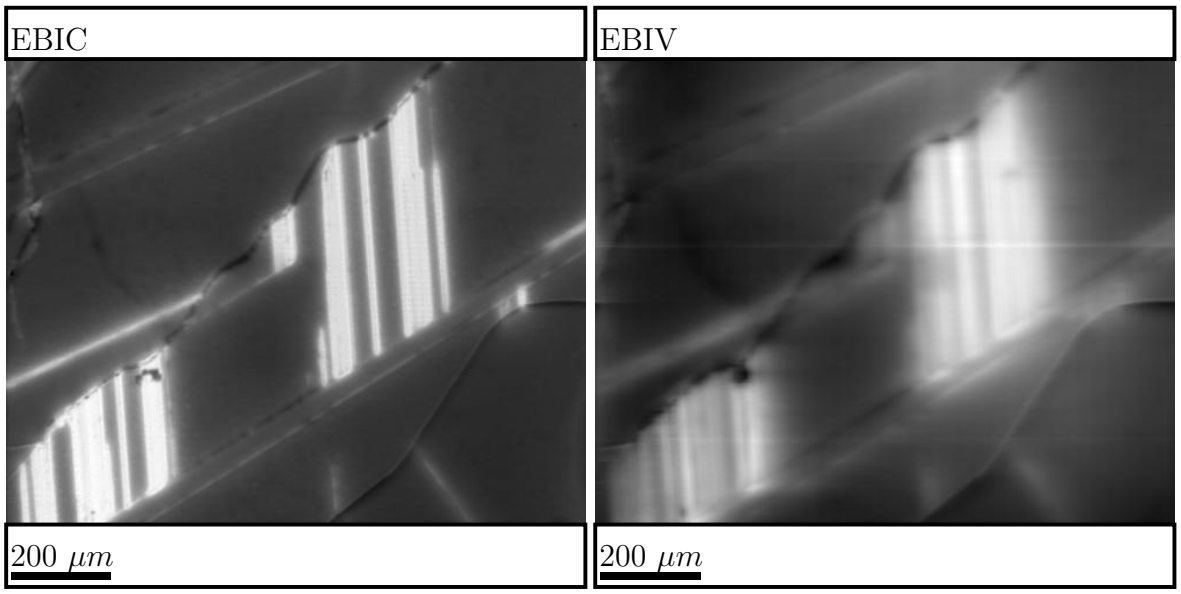

Figure 5.24: EBIC (left) and EBIV (right), 30 keV, 100 pA at 15.5 K.

It is noticeable that both EBIC and EBIV images looks almost similar. To show that in more detail in Fig.5.25 normalized EBIC and EBIV profiles were compared with each other.

The green arrows and circles mark the most evident similarities. One problem with the EBIV measurement should be mentioned, namely if the resistance of the material exceeds the input impedance of the amplifier, the assumption of measuring the current independent voltage is no longer valid.

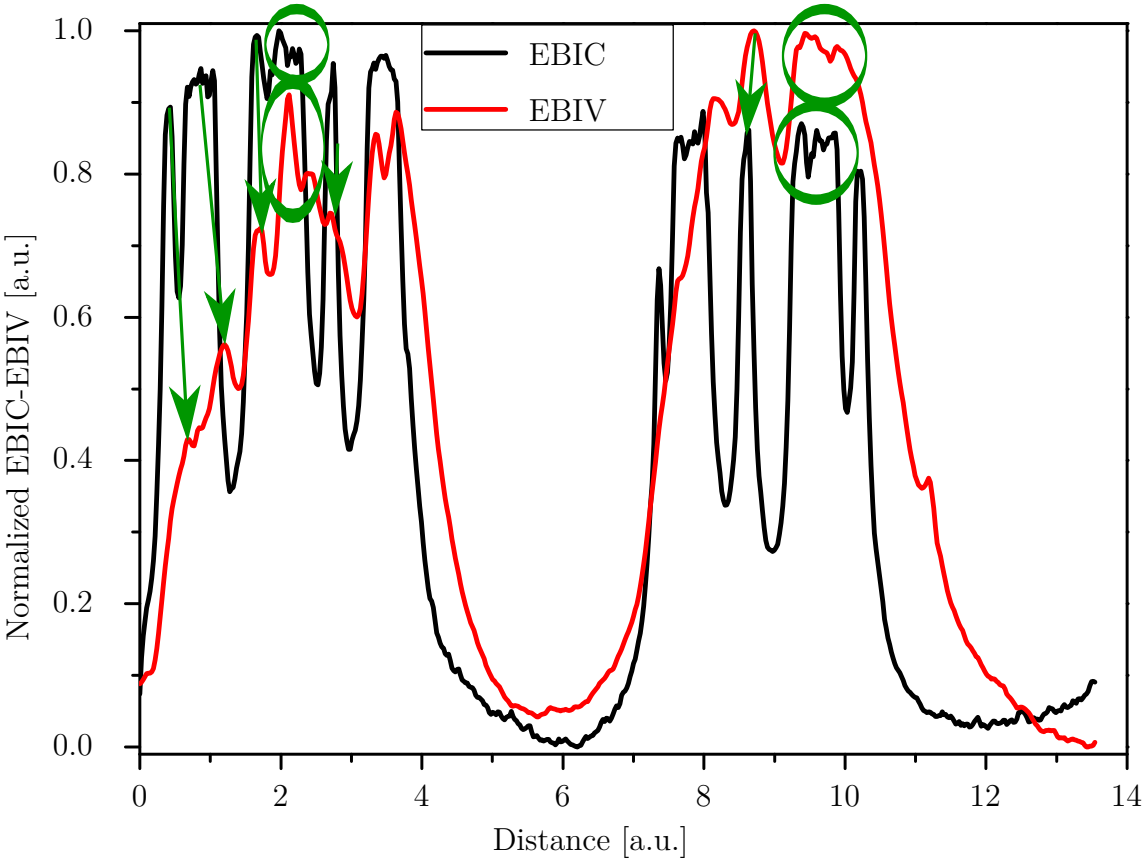

Figure 5.25: Normalized EBIC and EBIV profile taken at the same position across the sample shown in Fig.5.24, 30 keV, 100 pA at 15.5 K.

The also measured characteristic IV curve, with blanked electron beam, (Fig.5.23 (blue at right)) of the sample reveals a diode with a differential resistance of $\sim 0.8\ M\Omega$ at the operating point at 0.9 V with an input resistance of 100 Ω at the EBIC amplifier. Because of the high differential resistance, it is conceivable that the measured EBIV values are no longer current independent. Therefore, the evaluation of the EBIV values with respect to estimate local differences in the resistance is unfeasible.

5.2 Summary

Twin boundaries that reveal no EBIC contrast from 300 K room temperature down to 80 K liquid nitrogen temperature, show bright features below 30 K with liquid helium cooling. Below a certain temperature the collection efficiency at grain positions dramatically decrease while the efficiencies at TB remain at a higher level for a few more K. Furthermore, areas with several close neighbored TB remain at high collection efficiency over the entire investigated temperature range.

The critical temperature where the grain efficiency starts to decrease could be estimated at this samples with temperature dependent EBIC measurements to $27 - 24$ K. The single TBs follow $2 - 3$ K later. It was possible to show this behavior at different p-type mc-Si samples at varied block heights and also from different suppliers. It should be mentioned that the measured samples have an almost similar doping level. Additionally, the bright features could also be observed at n-type mc-Si. To ensure that the findings are not gathered at special selected spots the measurements were repeated at different spots at the same TB, as well as at several various TBs.

A model to explain the difference in the electrical behavior between grains and TB could be suggested. An alteration in the so-called "freeze out" temperature is conceivable. While the carriers in the grains freeze out, the carriers in the TB remain alive. This may lead to a more semi insulating characteristic of the grains than semi-conductive in the TB. With this assumption, EBIC signals like the measured once are probable. The "freeze out" temperature should be dependent of the doping level. To achieve a difference in the "freeze out" temperature between grains and TB a shrinkage of the local band gap at the TB could be a potential reason. A shrinkage of just ~ 4 meV would lower the "freeze out" temperature about 2 K, which is just about the estimated difference between the efficiency decrease at the grains and the TB. The band gap shrinkage is possibly related to local strain.

A main influence at the electrical behavior through a possible temperature dependent enlargement of the SCR seems improbable. As a side-effect, it is possible that a local SCR is built around the TBs and enhanced the field strength there.

Furthermore, it was pointed out that deep defect levels are also able to cause a band gap shrinkage, but it was no dark EBIC contrast to observe. Just the temperature-related bright contrast is comparable with the previously reported behavior of group 1 defects attributed to deep defect levels. The current dependent contrast could not be clearly counted to one of the reported defect groups. Due to the absence of dark

contrast at the EBIC investigation, it is doubtful to use this classification of defects for this case in any way.

It is suggested that also enhanced recombination could be involved in triggering the difference in the collection efficiency. This is considered because at the measurement conditions at where the bright features could be observed, low injection is no longer valid and high injection effects might have to be taken into account. Further investigations to clarify the influence of high injection conditions to the carrier recombination at low temperatures below 30 K are necessary.

Otherwise, a more probable explanation for the appearing behavior under higher beam current excitation is an alteration of the resistivity in the grains compared to the TB, because a higher current also needs a higher conductivity to be transported. This suggestion is supported by placing just a small ohmic contact at the backside. This shows that at low temperatures due to the increasing resistivity just a few amount of carriers are able to reach the contacts. Only carriers next to the contact are count to the detected EBIC signal.

Due to the absence of an EBIC signal next to the front contact, it was possible to rule out dislocation networks as reason for the low temperature TB behavior.

The multi TBs show always a deviation from the single TB behavior, which could be explained with the size of the generation volume, the width of the multi TB structure as well as with the tilted progression of the TB. Another conceivable explanation for the behavior of the TBs during beam current as well as beam energy dependent measurements could be a possible potential barrier break down of the Schottky-diode. At a certain generated current, the diode potential at the grains will break down and cause a lower charge collection. The suggested difference in the barrier heights of grain and TB sites could be supported through measuring the EBIC current with applied bias. Thus enables the estimation of the build-in potential at the TBs to about $0.6 - 0.8$ V. In contrast, at the grains, the efficiency already starts to decrease at -2 V. Thus, the barrier tends to be lower than at the TBs. This assumption is supported by the current dependence of the grain and TBs efficiencies, which show that the grain efficiency decrease starts at first and the TBs efficiencies follow only when 200 pA more are applied. Accordingly, it is possible that the necessary electric field for the carrier separation is still provided at the TBs, while at the grains the potential is reduced and thus the electric field is also weaker than that of the TBs. As a result, the carriers at the TBs could be separated and count for the EBIC signal, whereas at the grains the collected current is reduced.

Additionally, investigations with blanked electron beam provide a characteristic line of a diode with a differential resistance of 0.8 $M\Omega$.

The evaluation of a deviation in the local resistance using EBIV instead of EBIC is unfeasible because it is possible that the material resistance exceeds the input impedance of the amplifier.

Finally, to ascertain a satisfying explanation for the higher collection efficiency at the TBs compared to the grain, additional investigations have to be conducted. It should be noted that the investigations in this chapter were highly complicated to perform. Due to the high amount and high cost of liquid helium, which was necessary to provide stable low temperatures over a certain time it was simply possible to measure three connected days at each can of helium. After two - three days the temperatures become unstable and the collected data unreliable. Every delay within the investigation procedure could wreck the entire three day measurement period. Bad contacts at the sample below 80 K, inexplicable cooling problems caused that temperatures below 30 K could not be reached, frozen helium jack including the needle valve to control the helium flow, and unstable beam currents with following cathode rupture to name just a few problems occurring and disturbing the investigations for this chapter.

6 Conclusions

After the first two introducing chapters, the third was focused on the usual appearing defects. For this reason radiative as well as non-radiative defects features were shown, appearing through CL and EBIC measurements. Performing these investigations also reveal some uncommon and unexplained defect features. It was possible to show a luminescence line at 0.77 eV at room temperature which is related to OP, according to the literature. This line could be identified to be similar to the already reported P-line. However, in contrast to the reported properties by Tajima et al. [94], it was also possible to detect this luminescence at 10 K next to the D1-line clearly distinguishable from each other at once. These contradictory measurements results will fuel the existing discussion about the oxygen related luminescence lines and their relation to the long time known D1 luminescence. Moreover, due to the unexpected results, further investigations could be considered necessary.

Besides the oxygen related luminescence the occurrence of an enhanced BB luminescence at a few GBs, in comparison to the surrounding grains, could be shown briefly. Unfortunately, it was not possible to establish the same observation through repeated measurements in the laboratories of the Electron and Ion Microscopic Facility of Interdisciplinary Resource Center of Nanotechnology in Saint Petersburg. It is conceivable that the usable beam current there was not sufficiently high to excite the BB luminescence. Therefore, it is reasonable to perform additional investigations to offer a satisfying explanation for the occurrence of the intense BB luminescence at all.

One remarkable success is the highly educated guess of the relation between the investigated intense luminescence at 0.93 eV, named Di luminescence after previous reports by Krause et al.[45; 44], and the occurrence of Frank partial dislocations at the luminescent grain boundary spots. At room temperature, usually just D1 luminescence could be observed. Given that defects that show recombination activity at room temperature could potentially affect the solar cell performance, the question of where this luminescence originates from has gained interest. The strong luminescence appears inhomogeneous at GBs, which also show a strong EBIC contrast. Through electron

beam scattering diffraction measurements, it was possible to identify these luminescent parts of the grain boundary to have a <344> orientation. Additionally detailed structural investigations with transmission electron microscopy show the occurrence of Frank partial dislocations bordering stacking faults at the Di luminescence emitting grain boundary spots. Energy levels induced by Frank partials are similar to these ones necessary to cause luminescence in the energy range of the Di-line. A conceivable two level model to explain the energetic transitions is supposed, containing one level located at 120 meV below the conduction band and the second one at 90 meV above the valence band. For these summarized reasons, Frank partials are strongly suggested to be a root-cause for the observed Di luminescence at 0.93 eV.

In addition to the observed and presented radiative defect features with luminescence methods like PL and CL, methods were also used to observe recombination active defects in general. With EBIC, it was possible to show dislocation clusters and getterzones around certain GBs and at dislocation spots.

The second accomplished main aim was to explain the unexpected electrical behavior of twin boundaries. In general, these TBs do not show an EBIC recombination contrast. However at a certain low temperature, $27 - 24$ K for a sample doping level of $\sim 10^{16}$ cm^{-3}, the EBIC collection efficiency of the grains decrease strongly while the charge collection at the location of TBs remain at a higher level. Because this effect could be demonstrated at samples from different suppliers, different p-type mc-Si ingot block heights and at samples with a different kind of doping, n-type mc-Si, the revealed twin boundary property is supposed to be a general one. It is suggested that the difference in the charge collection could be related to a difference in the "freeze-out" temperature between grains and TBs. The alteration could possibly be explained with a local shrinkage of the band gap at the TBs. A possibility to achieve such a band gap decrease is the local existence of tensile stress, induced through the TB structure.

With certain higher beam currents, it was possible to achieve the higher collection efficiency at the TBs also at a higher temperature, above 27 K, even at 34 K. Therefore, it is conceivable that there is also an influence through the generated current and the diode potential to the collection efficiency. It was shown that beam current and beam energy dependent measurements indicate that there could be a breakdown of the diode potential barrier at the grain sites due to increasing generated current. The diode potential barrier at the grains seems lower than the estimated one, $0.6 - 0.8$ V, for the TBs. An existing increase of the material resistivity due to temperature decrease was presented through measurement results by EBIC investigations with a smaller ohmic

back contact. At low temperatures, just carriers generated next to the back contact could be collected, far away generated carriers were unable to reach the contact, and consequently these are not contributed to the collected EBIC signal. The possibility of an existing conductive dislocation network, like reported in the literature [34], could be ruled out due to the missing bright EBIC contrast next to the contact. To provide a complete detailed satisfying explanation of the TB behavior at low temperatures, further investigations are remain necessary. One of the open questions remain whether the eventuation of high injection at a certain temperature - beam setting relationship with the coincidentally occurrence of the higher collection efficiency at the TB is simply accidental. In addition, the potential barrier breakdown should also be verified in future measurements.

In addition to the presented research at mc-Si, results from investigations at thin-film Si samples were also shown. First time cross sectional EBIC investigations at tandem cells could be performed. These measurements reveal recombination differences between the various layers. With the information gathered through the measurements, contacting as well as material problems could be demonstrated. It was shown that thin-films could be highly sensitive to electron beam radiation and that the underlaying glass substrate could influence the properties of the silicon layer. Common EBIC measurements could show interaction problems between interlayers and the silicon film. Furthermore, probably first time investigations of contrast inversion at crystalline silicon thin films at glass substrate could be conducted. Additionally, it was pointed out that the interpretation as well as the analysis of the acquired data are rather complicate at thin-film than at mc-Si samples. It seems appropriate to continue with further investigations at thin-films to provide a broad basic knowledge to improve the data interpretation as well as the conduction of the measurements themselves.

Scientific visibility

Publications in peer-reviewed journals

1. C. Krause, T. Arguirov, W. Seifert, D. Mankovics, H.M. Krause, M. Kittler, „Properties of strong luminescence at 0.93 eV in solar grade silicon“, Solid State Phenomena 205 – 206, 83 – 88 (2014)
2. C. Krause, D. Mankovics, H.-M. Krause, T. Arguirov, M. Kittler, „On the origin of intense luminescence at 0.93 eV in multicrystalline silicon“, J. Appl. Phys. 114, 034902 (2013)
3. A. Klossek, C. Krause, T. Arguirov, H.-M. Krause, W. Seifert, F. Friedrich, S. Calnan, O. Gabriel, B. Stannowski, and M. Kittler, „Characterization of thin-film a-Si:H/μc-Si:H tandem solar cells on glass substrates“, Cryst. Res. Technol. 48, 279 – 286 (2013)
4. D. Mankovics, A. Klossek, Ch. Krause, T. Arguirov, W. Seifert, M. Kittler, „Luminescence of defects and breakdown sites in multicrystalline silicon solar cells“, Phys. Status Solidi (A) 209(10), 1908 – 1912, (2012)

Own presentations at conferences

1. C. Krause, W. Seifert, M. Kittler, „Low temperature EBIC investigation of the electrical behaviour at twin boundaries in mc-silicon“, 12th International Workshop on Beam Injection Assessment of Microstructures (BIAMS 2014), June 22 – 26, 2014, Tsukuba, Japan
2. C. Krause, W. Seifert, M. Kittler, „Electrical behavior of twin GBs in mc-silicon below 30K - an EBIC investigation“, 49. Punktdefekttreffen, April 4 – 5, 2014, Dresden, Germany
3. C. Krause, W. Seifert, M. Kittler, „Electrical behaviour of twin GBs in mc-silicon below 30 K“, Projekttreffen SolarWinS, January 28 – 30, 2014, Ochsenfurt, Germany
4. C. Krause, T. Arguirov, D. Mankovics, H.M. Krause, M. Kittler, „Properties of D3-like (0.93 eV) luminescence in solar grade silicon“, GADEST 2013, September 22 – 27, 2013, Oxford, UK
5. C. Krause, D. Mankovics, T. Arguirov, M. Krause, M. Kittler, „Characteristic and cause of the 0.93 eV defect-luminescence in mc-silicon“, Projekttreffen SolarWinS, July 9 – 11, 2013, Apolda, Germany
6. C. Krause, D. Mankovics, T. Arguirov, M. Krause, M. Kittler, „Investigation of D3-like luminescence in mc-solar silicon“, DPG-Frühjahrstagung, 10 – 15. March 2013, Regensburg, Germany
7. C. Krause, D. Mankovics,„Unknown origin of very intense D3 like luminescence in solar silicon“, 48. Punktdefekttreffen, October 13 – 14, 2011, Dresden, Germany

References

1 Amkreutz, D. ; Müller, J. ; Schmidt, M. ; Hänel, T. ; Schulze, T. F.: Electron-beam crystallized large grained silicon solar cell on glass substrate. In: *Progress in Photovoltaics: Research and Applications* 19 (2011), Nr. 8, S. 937–945

2 Arguirov, T. V.: *Electro-optical properties of dislocations in silicon and their possible application for light emitters*, BTU Cottbus, Dissertation, 2007

3 Bauer, J. ; Wagner, J.-M. ; Lotnyk, A. ; Blumtritt, H. ; Lim, B. ; Schmidt, J. ; Breitenstein, O.: Hot spots in multicrystalline silicon solar cells: avalanche breakdown due to etch pits. In: *Phys. Status Solidi (RRL)* 3 (2009), Nr. 2-3, S. 40–42

4 Binetti, S. ; Pizzini, S. ; Leoni, E. ; Somaschini, R. ; Castaldini, A. ; Cavallini, A.: Optical properties of oxygen precipitates and dislocations in silicon. In: *J. Appl. Phys.* 92 (2002), S. 2437

5 Binetti, S. ; Somaschini, R. ; Donne, A. L. ; Leoni, E. ; Pizzini, S. ; Li, D. ; Yang, D.: Dislocation luminescence in nitrogen-doped Czochralski and float zone silicon. In: *J. Phys.: Condensed Matter* 14 (2002), S. 13247

6 Blumenau, A. T. ; Jones, R. ; Öberg, S. ; Briddon, P. R. ; Frauenheim, T.: Dislocation Related Photoluminescence in Silicon. In: *Phys. Rev. Lett.* 87 (2001), S. 187404

7 Bo, S. ; Kai, Y. ; Peng, C. ; Rong, Z. ; Yi, S. ; You-dou, Z. ; Sekiguchi, T. ; Sumino, K.: Electrical Activity of Frank Partial Dislocations and the Influence of Metallic Impurities in Czochralski-Grown Silicon. In: *Chinese Physics Letters* 14 (1997), Nr. 6, S. 436

8 Borghesi, A. ; Pivac, B. ; Sassella, A. ; Stella, A.: Oxygen precipitation in silicon. In: *Journal of Applied Physics* 77 (1995), Nr. 9, S. 4169–4244

9 Breitenstein, Otwin ; Bauer, Jan ; Bothe, Karsten ; Kwapil, Wolfram ; Lausch, Dominik ; Rau, Uwe ; Schmidt, Jan ; Schneemann, Matthias ; Schubert, Martin C. ; Wagner, Jan-Martin ; Warta, Wilhelm: Understanding junction breakdown in multicrystalline solar cells. In: *Journal of Applied Physics* 109 (2011), Nr. 7, S. –

10 Brown, T.G. ; Hall, G.: Optical emission at 1.32μm from sulfur-doped crystalline silicon. In: *Appl. Phys. Lett.* 49 (1986), S. 245

11 Cai, J. ; Ishikawa, Y. ; Wada, K.: Strain induced bandgap and refractive index variation of silicon. In: *Opt. Express* 21 (2013), Mar, Nr. 6, S. 7162–7170

12 Chen, J. ; Chen, B. ; Sekiguchi, T. ; Fukuzawa, M. ; Yamada, M.: Correlation between residual strain and electrically active grain boundaries in multicrystalline silicon. In: *Appl. Phys. Lett.* 93 (2008), S. 112105

13 Davies, G. ; Brian, H. ; Lightowlers, E. C. ; Barraclough, K. ; Thomaz, M. F.: The temperature dependence of the 969meV 'G' optical transition in silicon. In: *Semicond. Sci. Technol.* 4 (1989), S. 200–206

14 Donolato, C.: On the theory of SEM charge-collection imaging of localized defects in semiconductors. In: *Optik* 52 (1978), S. 19

15 Dreckschmidt, F.: *Strahlende Defektübergänge in multikristallinem Silicium*, Technische Universität Bergakademie Freiberg, Dissertation, 2012

16 Drozdov, N. A. ; Patrin, A. A. ; Tkachev, V. D.: Recombination radiation on dislocation in silicon. In: *JETP Letters* 23 (1976), S. 597

17 Dziewior, J. ; Schmid, W.: Auger coefficients for highly doped and highly excited silicon. In: *Appl. Phys. Lett.* 31 (1977), S. 346

18 Everhart, T. E. ; Hoff, P. H.: Determination of Kilovolt Electron Energy Dissipation vs Penetration Distance in Solid Materials. In: *J. Appl. Phys.* 42 (1971), S. 5837

19 Föll, H.: *Defects in Crystals*. online Script

20 Föll, H. ; Kolbesen, B. O.: Agglomerate von Zwischengitteratomen (Swirl-Defekte) in Silizium- Ihre Bedeutung für Grundlagenforschung und Technologie. In: *Jahrbuch der Akademie der Wissenschaften in Göttingen* (1976), S. 27

21 Green, M. A. ; Basore, P. A. ; Chang, N. ; Clugston, D. ; Egan, R. ; Evans, R. ; Hogg, D. ; Jarnason, S. ; Keevers, M. ; Lasswell, P. ; SullivanSullivan, J. O. ; Schubert, U. ; Turner, A. ; Wenham, S. R. ; Young, T.: Crystalline silicon on glass (CSG) thin-film solar cell modules. In: *Solar Energy* 77 (2004), Nr. 6, S. 857 – 863. – Thin Film {PV}

22 Grundmann, M. ; Rhodes, W. T. (Hrsg.) ; Stanley, H. E. (Hrsg.) ; Needs, R. (Hrsg.): *The Physics of Semiconductors - An Introduction Including Nanophysics and Applications*. Springer-Verlag, 2nd

23 Hall, R. N.: Electron-Hole Recombination in Germanium. In: *Phys. Rev.* 87 (1952), S. 387

24 He, Liang ; Wang, Gang ; Rong, Yi-ming: Modeling on directional solidification of solar cell grade multicrystalline silicon ingot casting. In: *Journal of Shanghai Jiaotong University (Science)* 16 (2011), Nr. 3, S. 316–319

25 Higgs, V. ; Kittler, M.: Investigation of the recombination activity of misfit dislocations in Si/SiGe epilayers by cathodoluminescence imaging and the electron beam induced current technique. In: *Appl. Phys. Lett.* 63 (1993), S. 2085

26 Hull, D. ; Bacon, D. J.: *Introduction to Dislocations*. Fifth Edition. Butterworth-Heinemann (Elsevier), 2011

27 Inoue, M. ; Sugimoto, H. ; Tajima, M. ; Ohshita, Y. ; Ogura, A.: Microscopic and spectroscopic mapping of dislocation-related photoluminescence in multicrystalline silicon wafers. In: *Journal of Materials Science: Materials in Electronics* 19 (2008), Nr. 1, S. 132–134

28 Ishikawa, T. ; Koga, K. ; Itahashi, T. ; Vlasenko, L.S. ; Itoh, K.M.: Photoluminescence from triplet states of isoelectronic bound excitons at interstitial carbon-intersititial oxygen defects in silicon. In: *Physica B: Condensed Matter* 404 (2009), Nr. 23 24, S. 4552 – 4554. – Proceedings of the 25th International Conference on Defects in Semiconductors

29 Jones, R. ; Coomer, B. J. ; Goss, J. P. ; Öberg, S. ; Briddon, P. R.: Intrinsic Defects and the D1 to D4 Optical Bands Detected in Plastically Deformed Si. In: *Phys. Status Solidi B* 222 (2000), S. 133

30 Kanaya, K. ; Okayama, S.: Penetration and energy-loss theory of electrons in solid targets. In: *J. Phys. D: Applied Physics* 5 (1972), S. 43

31 Kenyon, A. J. ; Steinman, E. A. ; Pitt, C. W. ; Hole, D. E. ; Vdovin, V. I.: The origin of the 0.78 eV luminescence band in dislocated silicon. In: *J. Phys.: Condens. Matter* 15 (2003), S. 2843

32 Kerr, M. J. ; Cuevas, A.: General parameterization of Auger recombination in crystalline silicon. In: *J. Appl. Phys.* 91 (2002), S. 2473

33 Kimerling, L. C. ; Leamy, H. J. ; Patel, J. R.: The electrical properties of stacking faults and precipitates in heat-treated dislocation-free Czochralski silicon. In: *Appl. Phys. Lett.* 30 (1977), Nr. 5, S. 217

34 Kittler, M. ; Reiche, M. ; Seifert, W. ; Yu, X. ; Arguirov, T. ; Vyvenko, O.F. ; Mchedlidze, T. ; Wilhelm, T.: Regular Dislocation Networks in Silicon as a Tool for Novel Device Application. In: *ECS Transactions* 3(4) (2006), S. 429–450

35 Kittler, M. ; Seifert, W.: *Methodische und angewandte Arbeiten zum EBIC-Verfahren an Halbleiter-Silizium und Bauelementen auf Silizium-Basis.* 1984

36 Kittler, M. ; Seifert, W.: On the Origin of EBIC Defect Contrast in Silicon, A Reflection on Injection and Temperature Dependent Investigations. In: *Phys. Status Solidi A* 138 (1993), S. 687

37 Kittler, M. ; Seifert, W.: EBIC defect characterisation: state of understanding and problems of interpretation. In: *Mater. Sci. Eng. B* 42 (1996), S. 8–13

38 Kittler, M. ; Seifert, W. ; Higgs, V.: Recombination Activity of Misfit Dislocations in Silicon. In: *Phys. Status Solidi A* 137 (1993), S. 327–335

39 Kittler, Martin ; Reiche, Manfred: Dislocations as Active Components in Novel Silicon Devices. In: *Advanced Engineering Materials* 11 (2009), Nr. 4, S. 249–258

40 Klossek ; Mankovics, D. ; Kittler, M.: Distribution of Defects and Breakdown Sites in UMG-Si Solar Cells Studied by Luminescence Imaging. In: *Energy Procedia* 27 (2012), Nr. 0, S. 143 – 146. – Proceedings of the 2nd International Conference on Crystalline Silicon Photovoltaics SiliconPV 2012

41 Klossek, A.: *Optical characterisation of thin-film Si solar cells and knowledge transfer from bulk mc-Si*, Brandenburgischen Technischen Universität Cottbus, Dissertation, 2013

42 Klossek, A. ; Krause, C. ; Arguirov, T. ; Krause, H.-M. ; Seifert, W. ; Friedrich, F. ; Calnan, S. ; Gabriel, O. ; Stannowski, B. ; Kittler, M.:

Characterization of thin-film a-Si:H/ μc-Si:H tandem solar cells on glass substrates. In: *Cryst. Res. Technol.* 48 (2013), S. 279–286

43 Krause, C.: *Charakterisierung von GaN für LEDs gewachsen auf Si- und Al2O3-Substraten unter Verwendung von Pufferschichten*, IHP/BTU Joint Lab, Diplomarbeit, 2010

44 Krause, C. ; Arguirov, T. ; Seifert, W. ; Mankovics, D. ; Krause, H.-M. ; Kittler, M.: Properties of strong luminescence at 0.93 eV in solar grade silicon. In: *Solid State Phenomena* 205-206 (2014), S. 83

45 Krause, C. ; Mankovics, D. ; Krause, H.-M. ; Arguirov, T. ; Kittler, M.: On the origin of intense luminescence at 0.93 eV from multi-crystalline silicon. In: *J. Appl. Phys.* 114 (2013), S. 034902

46 Krumeich, F.: *The Electron Microscopy Site*. Website. 2012. – URL `www.microscopy.ethz.ch`

47 Kürner, W. ; Sauer, R. ; Dörnen, A. ; Thonke, K.: Structure of the 0.767-eV oxygen-carbon luminescence defect in 450°C thermally annealed Czochralski-grown silicon. In: *Phys. Rev. B* 39 (1989), Jun, S. 13327–13337

48 Kurniawan, O. ; Ong, V. K. S.: Investigation of Range-energy Relationships for Low-energy Electron Beams in Silicon and Gallium Nitride. In: *Scanning* 29 (2007), Nr. 6, S. 280–286

49 Kveder, V. ; Badylevich, M. ; Schröter, W. ; Seibt, M. ; Steinman, E. ; Izotov, A.: Silicon light-emitting diodes based on dislocation-related luminescence. In: *Phys. Status Solidi A* 202 (2005), S. 901

50 Kveder, V. ; Kittler, M. ; Schröter, W.: Recombination activity of contaminated dislocations in silicon: A model describing electron-beam-induced current contrast behavior. In: *Phys. Rev. B* 63 (2001), S. 115208

51 Lautenschlager, P. ; Allen, P.B. ; Cardona, M.: Temperature dependence of band gaps in Si and Ge. In: *Phys. Rev. B Condens Matter.* 31 (1985), Nr. 4, S. 2163

52 Lee, W. ; Chen, J. ; Chen, B. ; Chang, J. ; Sekiguchi, T.: Cathodoluminescence study of dislocation-related luminescence from small-angle grain boundaries in multicrystalline silicon. In: *Appl. Phys. Lett.* 94 (2009), S. 12103

53 Lelikov, Yu. S. ; Rebane, Yu. T. ; Ruvimov, S. ; Sitnikova, A. A. ; Tarhin, D. V. ; Shreter, Yu. G.: A Classification of the Dislocation-Related Photoluminescencence in Silicon. In: *Phys. Status Solidi B* 172 (1992), S. 53

54 Liang, Di ; Bowers, John E.: Recent progress in lasers on silicon. In: *Nat Photon* 4 (2010), August, Nr. 8, S. 511–517

55 Liu, L. ; Edgar, J. H.: Substrates for gallium nitride epitaxy. In: *Mater. Sci. Eng. : R: Reports* 37 (2002), Nr. 3, S. 61–127

56 Logan, R. A. ; Peters, A. J.: Impurity Effects upon Mobility in Silicon. In: *Journal of Applied Physics* 31 (1960), Nr. 1, S. 122–124

57 Ma, J. L. ; Fu, Z. F. ; Wei, Q. ; Zhang, H. M.: Uniaxial Stress Induced Electron Mobility Enhancement in Silicon. In: *Silicon* 5 (2013), Nr. 3, S. 219–224

58 Mankovics, D. ; Klossek, A. ; Krause, Ch. ; Arguirov, T. ; Seifert, W. ; Kittler, M.: Luminescence of defects and breakdown sites in multicrystalline silicon solar cells. In: *Phys. Status Solidi A* 209 (2012), Nr. 10, S. 1908–1912

59 Mankovics, D. ; Schmid, R. P. ; Arguirov, T. ; Kittler, M.: Dislocation-related photoluminescence imaging of mc-Si wafers at room temperature. In: *Cryst. Res. Technol.* 47 (2012), Nr. 11, S. 1148

60 Matsuoka, M. ; Tohno, S.: 1.54 μm wavelength emission of erbium-doped silicon films grown by ion beam epitaxy using sputtering-type metal ion source. In: *Appl. Phys. Lett.* 66 (1995), S. 1862

61 Mchedlidze, T. ; Arguirov, T. ; Kononchuk, O. ; Trushin, M. ; Kittler, M.: Structures responsible for radiative and non-radiative recombination activity of dislocations in silicon. In: *Phys. Status Solidi C* 8 (2011), S. 991

62 Mchedlidze, T. ; Kononchuk, O. ; Arguirov, T. ; Trushin, M. ; Reiche, M. ; Kittler, M.: Determination of the Origin of Dislocation Related Luminescence from Silicon Using Regular Dislocation Networks. In: *Solid State Phenomena* 156-158 (2009), S. 567

63 Mchedlidze, T. ; Seifert, W. ; Kittler, M. ; Blumenau, A. T. ; Birkmann, B. ; Mono, T. ; Müller, M.: Capability of photoluminescence for characterization of multi-crystalline silicon. In: *J. Appl. Phys.* 11 (2012), S. 073504

64 Mchedlidze, T. ; Wilhelm, T. ; Arguirov, T. ; Trushin, M. ; Reiche, M. ; Kittler, M.: Correlation of electrical and luminescence properties of dislocation networks with its microscopic structure. In: *Phys. Status Solidi C* 6 (2009), S. 1817

65 Minaev, N. S. ; Mudryi, A. V.: Thermally-Induced Defects in Silicon Containing Oxygen and Carbon. In: *Phys. Status Solidi A* 68 (1981), S. 561

66 Möller, H. J.: Carbon-induced twinning in multicrystalline silicon. In: *Solid State Phenomena* 95-96 (2004), S. 181

67 Morin, F. J. ; Maita, J. P.: Electrical Properties of Silicon Containing Arsenic and Boron. In: *Phys. Rev.* 96 (1954), S. 28

68 Mudryi, A.V. ; Patuk, A.I. ; Shakin, I.A. ; Ulyashin, A.G. ; Job, R. ; Fahrner, W.R. ; Fedotov, A. ; A.Mazanik ; Drozdov, N.: Impurities and defects in multicrystalline silicon for solar cells: low-temperature photoluminescence investigations. In: *Solar Energy Materials & Solar Cells* 72 (2002), S. 503–508

69 Myhajlenko, Stefan ; D.R.Vij (Hrsg.): *Luminescence of Solids.* Plenum Press, New York, 1998

70 Noonan, J. R. ; Kirkpatrick, C. G. ; Streetman, B. G.: Photoluminescence from Si irradiated with 1.5-MeV electrons at 100K. In: *J. Appl. Phys.* 47 (1976), S. 3010

71 Ottaviani, G. ; Reggiani, L. ; Canali, C. ; Nava, F. ; Alberigi-Quaranta, A.: Hole drift velocity in silicon. In: *Phys. Rev. B* 12 (1975), Oct, S. 3318–3329

72 Pankove, Jacques I.: *Optical processes in semiconductors.* Prentice-Hall, Inc., Englewood Clifs, NJ, 1971

73 Petrov, V. I.: Cathodoluminescence Scanning Microscopy. In: *Phys. Status Solidi A* 133 (1992), S. 189–230

74 Pizzini, S. ; Binetti, S. ; Le Donne, A. ; Marzegalli, A. ; Rabier, J.: Optical properties of shuffle dislocations in silicon. In: *Applied Physics Letters* 88 (2006), Nr. 21, S. –

75 Sauer, R. ; Weber, J.: Photoluminescence of defect complexes in silicon. In: *Lecture Notes on Physics* 175 (1983), S. 120–133

76 Sauer, R. ; Weber, J. ; Stolz, J. ; Weber, E. R. ; Küsters, K.-H. ; Alexander, H.: Dislocation-related photoluminescence in silicon. In: *Appl. Phys. A Solids and Surfaces* 36 (1985), S. 1

77 Schlangenotto, H. ; Maeder, H. ; Gerlach, W.: Temperature dependence of the radiative recombination coefficient in silicon. In: *Phys. Status Solidi A* 21 (1974), S. 357

78 Schmid, R. P. ; Mankovics, D. ; Arguirov, T. ; Mchedlidze, T. ; Kittler, M.: Novel imaging techniques for dislocation-related D1-photo-luminescence of multicrystalline Si wafers - two different approaches. In: *Phys. Status Solidi C* 8 (2011), Nr. 4, S. 1297

79 Schmid, R. P. ; Mankovics, D. ; Arguirov, T. ; Ratzke, M. ; Mchedlidze, T. ; Kittler, M.: Rapid dislocation-related D1-photoluminescence imaging of multicrystalline Si wafers at room temperature. In: *Phys. Status Solidi A* 208 (2011), S. 888

80 Schönecker, A. ; Geerligs, L. J. ; Müller, A.: Casting Technologies for Solar Silicon Wafers: Block Casting and Ribbon-Growth-on-Substrate. In: *Solid State Phenomena* 95-96 (2003), S. 149

81 Schneider, J. ; Dore, J. ; Christiansen, S. ; Falk, F. ; Lichtenstein, N. ; Valk, B. ; Lewandowska, R. ; Slaoui, A. ; Maeder, X. ; Lábár, J. ; Sáfrán, G. ; Werner, M. ; Naumann, V. ; Hagendorf, C.: Solar Cells from Crystalline Silicon on Glass Made by Laser Crystallised Seed Layers and Subsequent Solid Phase Epitaxy. In: *Thin Film Crystalline Silicon Solar Cells and Wafer Equivalents 25th European Photovoltaic Solar Energy Conference and Exhibition / 5th World Conference on Photovoltaic Energy Conversion*, 2010

82 Schroder., Dieter K.: *Semiconductor Material and Device Characterization, 3rd Edition.* John Wiley & Sons, Inc., 2006

83 Schubert, M.C. ; Gundel, P. ; The, M. ; Warta, W. ; Romero, M.J. ; Ostapenko, S. ; Arguirov, T.: Spatially Resolved Luminescence Spectroscopy on Multicrystalline Silicon. In: *European Photovoltaic Solar Energy Conference and Exhibition (EU PVSEC)*, 2008

84 Sekiguchi, T. ; Kveder, V. V. ; Sumino, K.: Hydrogen effect on the optical activity of dislocations in silicon introduced at room temperature. In: *J. Appl. Phys.* 76 (1994), S. 7882

85 Sekiguchi, T. ; Sumino, K.: Cathodoluminescence study on dislocations in silicon. In: *J. Appl. Phys.* 79 (1996), S. 3253–3260

86 Sekiguchi, T. ; Yamane, H. ; Aoki, M. ; Araki, T. ; Shimada, M.: Cathodoluminescence study of h- and c-GaN single crystals grown by a Na or K flux. In: *Science and Technology of Advanced Materials* 3 (2002), Nr. 2, S. 91

87 Shockley, W. ; W.T. Read, Jr.: Statistic of the Recombination of Holes and Electrons. In: *Phys. Rev.* 87 (1952), S. 835

88 Sveinbjörnsson, E. Ö. ; Weber, J.: Room temperature electroluminescence from dislocation-rich silicon. In: *Appl. Phys. Lett.* 69 (1996), S. 2686

89 Sverdlov, Viktor ; Selberherr, Siegfried (Hrsg.): *Strain-Induced Effects in Advanced MOSFETs*. Springer Wien New-York, 2011

90 Sze, S. M. ; 2nd (Hrsg.): *Physics of Semiconductor Devices*. John Wiley & Sons, Inc., 1981

91 SZE, S.M.: *Semiconductor devices: physics and technology*. Wiley New York, 1985

92 Tajima, M. ; Takeno, H. ; Abe, T.: Characterization of Point Defects in Si Crystals by Highly Spatially Resolved Photoluminescence. In: *Mater. Sci. Forum* 83 (1992), S. 1327

93 Tajima, M. ; Takeno, H.i ; Warashina, M. ; Abe, T.: Role of Point Defects in Oxygen Agglomeration in Si. In: *Mater. Sci. Forum* 143 (1993), S. 147

94 Tajima, M. ; Tokita, M. ; Warashina, M.: Photoluminescence Due To Oxygen Precipitates Distinguished from the D Lines in Annealed Si. In: *Mater. Sci. Forum* 196 (1995), S. 1749

95 Tajima, Michio ; Iwata, Yasuaki ; Okayama, Futoshi ; Toyota, Hiroyuki ; Onodera, Hisashi ; Sekiguchi, Takashi: Deep-level photoluminescence due to dislocations and oxygen precipitates in multicrystalline Si. In: *J. Appl. Phys.* 111 (2012), Nr. 11, S. –

96 Thonke, K. ; Hangleiter, A. ; Sauer, R.: 0.79 eV (C line) defect in irradiated oxygen-rich silicon: excited state structure, internal strain and luminescence decay time. In: *J. Phys. C: Solid State Phys.* 18 (1985), S. L795

97 Weber, J. ; Bauch, H. ; Sauer, R.: Optical properties of copper in silicon: Excitons bound to isoelectronic copper pairs. In: *Phys. Rev. B* 25 (1982), Nr. 12, S. 7688–7699

98 Wu, C. J. ; Wittry, D. B.: Investigation of minority-carrier diffusion lengths by electron bombardment of Schottky barriers. In: *J. Appl. Phys.* 49 (1987), S. 2827

99 Yacobi, B. G. ; Holt, D. B.: Cathodoluminescence scanning electron microscopy of semiconductor. In: *J. Appl. Phys.* 59 (1986), February, Nr. 4, S. R1–R24

Acknowledgements

Hereby I would like to thank everyone who has contributed to the success of this work. My special thanks to

Prof. Dr. M. Kittler for giving me the opportunity to prepare my Ph.D. thesis at the Joint Lab of IHP and Brandenburg University of Technology and for his great support through the whole time.

Prof. Dr. P. Weger for his willingness to take care of one report on my thesis.

Prof. Dr. J. Reif for his helpful advices in any necessary situation.

Dr. W. Seifert for his guidance in respect of electron microscopy measurement methods and scientific documentation as well as for the critical experienced discussions, which often help to reconsider my thoughts carefully again.

H.-M. Krause for his great support in all experimental questions, performing the EBSD measurements and analysis for my work and of course for his enjoyable company during the lab work hours.

Dr. T. Arguirov for his encouragement concerning investigations, data interpretation, and presentation. Because of his always optimistic and humorous mood it was a very pleasant time with him in our lab.

Prof. Dr. O. Vyvenko for giving me the opportunity for a research stay at his lab in St. Petersburg to perform some of my investigations there.

Dr. A. Hähnel and H. Blumtritt for performing FIB preparation and TEM measurements and analysis at my samples.

In addition, I especially thank

my co-Ph.D-students Dr. A. Klossek, D. Mankovics, B. Schwartz for supporting me with PL and ReBEL measurements as well as their time and willing to think for oneself and to discuss thoughts and conclusions extensively. Especially the night shifts in some of the local establishments to, talk something through, were a great help.

all the other colleagues at the Joint Lab for the good cooperation and pleasant atmosphere during this work at the BTU Cottbus.

my parents and family which gave me the greatest possible support and stability over my whole study and in every decision I had to make in life.

my girlfriend for trying to cheer me up every day if I was in a bad mood, even if I have little time for her.

